A Biopolymer-Inspired Study on the Poynting Effect of Isotropic Materials

Zhe-Hong Pan

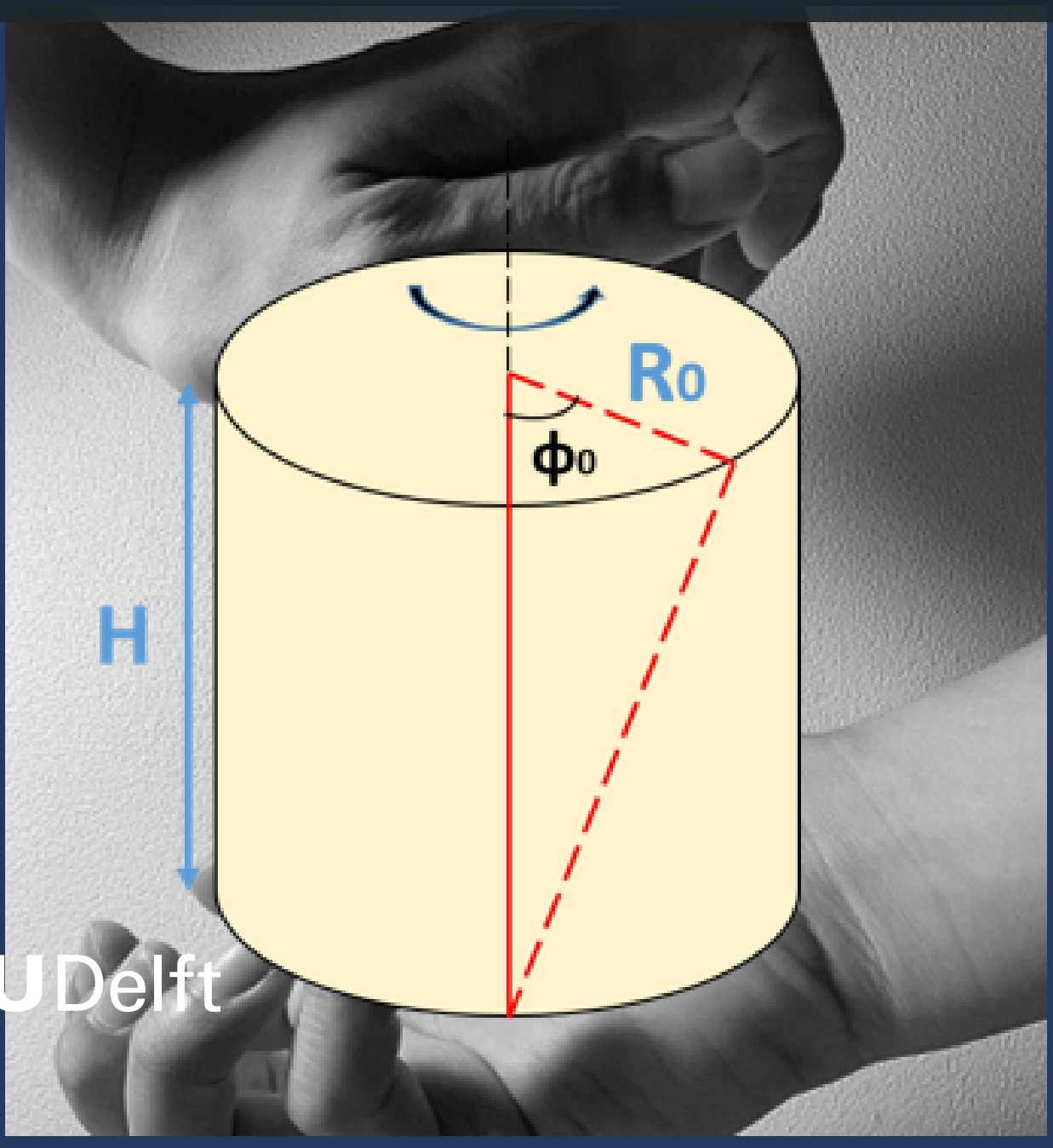

TU Delft

A Biopolymer-Inspired Study on the Poynting Effect of Isotropic Materials

Thesis report

by

Zhe-Hong Pan

to obtain the degree of Master of Science
at the Delft University of Technology
to be defended publicly on September 28, 2023 at 08:30

Thesis committee:	Dr. B.P. Tighe,	TU Delft, supervisor
	Dr. A.J.L.L. Buchner,	TU Delft, committee member
	Dr. O. Moultos,	TU Delft, committee member
Place:	Faculty of Technology, Policy and Management, Delft	
Project Duration:	December, 2022 - September, 2023	
Student number:	5491908	

An electronic version of this thesis is available at `http://repository.tudelft.nl/`.

Faculty of Mechanical Engineering · Delft University of Technology

Preface

This thesis marks the end of my brief yet fulfilling master's journey at TU Delft. Over the past ten months, I started research in previously uncharted territories, delving into a rather theoretical research direction. This was a significant breakthrough for me as it pushed me beyond my comfort zone while providing a deeper understanding of myself. As the ten months passed, I finally gained a deeper understanding of the amazing Poynting effect, which allowed me to complete this paper. Simultaneously, I have also harvested a wealth of support that will help me anticipate the next steps in my life and career.

I would like to express special thanks to my supervisor, Brian. Through continuous discussions and brainstorming, he not only inspired me greatly in this research topic but also guided me to accomplish this study. I am also grateful to my parents and sister for their encouragement throughout the past ten months, despite the physical distance, as we often connected through video calls to keep up with each other. At last, I am thankful for the cherished friends I made in Delft. The research journey has ups and downs occasionally, which is why this group of friends who joined me in late-night conversations over drinks played an irreplaceable role.

Zhe-Hong Pan
Delft, September 2023

Abstract

In recent times, soft matter has gained significant interest among researchers in the fields of biomechanics and biomedicine, especially in areas like soft robotics and biopolymers, due to its remarkable ability to undergo substantial deformations. Soft robotics often requires materials that can flexibly adapt to or mimic the movements of living organisms, requiring properties of flexibility and easy deformability. Biopolymers, naturally occurring in the human body, such as within brain tissue or blood clots, have gained attention due to their tendency to exhibit extensive deformation even under minimal loads. Consequently, there has been a growing emphasis on investigating stress-strain responses associated with these materials in recent years. This research particularly centers on a specific deformation phenomenon known as the Poynting effect.

Within the scope of this thesis, we employ two distinct deformation gradient tensors to analyze stress-strain responses under two separate boundary conditions: constant gap and constant normal stress boundary conditions. We also introduce a methodology for predicting the sign of the Poynting effect under conditions of small yet finite strain. Finally, we validate our analysis through simulation experiments.

The Poynting effect is related to the transverse stress or strain response when subjected to simple shear, revealing that the application of simple shear strain does not solely result in simple shear stress. This intriguing phenomenon captures our attention, primarily because it challenges intuitive expectations. In our exploration of the Poynting effect in soft matter, we commence with Meng's model, a network-theory-based framework rooted in an energy density function derived from the force-extension relationship of a single chain. Despite previous studies by Meng et al. on the Poynting effect, we identify flaws in their derivation process. Consequently, we opt for an alternative approach, directly computing the stress and strain responses of a cube subjected to shear forces.

To investigate the impact of compressibility, the original model undergoes a transformation into an isochoric model, followed by the addition of an extra volumetric function to create an almost incompressible model. Surprisingly, it is observed that the sign of the Poynting effect remains consistent for both the two-variable deformation gradient tensor denoted as $\mathbf{F}_1$ and the four-variable tensor represented as $\mathbf{F}_g$. The degree of compressibility has no distinguishable influence on determining this sign. In contrast, for $\mathbf{F}_g$, the magnitude of the stress response, under constant gap boundary conditions, amplifies as the Poisson's ratio approaches 0.5.

The prediction of the Poynting effect's sign is grounded in the concept of Maxwell's relation. In the final stages of derivation, we arrive at an expression that solely relies on material parameters, devoid of any strain variables. Remarkably, the obtained results exhibit substantial agreement with analytical solutions, affirming the method's efficacy in successfully predicting the sign of the Poynting effect.

Finally, we conducted a simulation study using Comsol. The results of this simulation indicate a closer alignment with the four-variable tensor $\mathbf{F}_g$, suggesting that the applied boundary conditions more closely resemble those employed in the numerical solution. Additionally, it is noteworthy that the specific geometries utilized in the study, cylinder and cube, did not exhibit any noticeable influence on determining the sign of the Poynting effect, particularly within the context of the chosen model and material parameters.

Contents

Nomenclature

Greek Symbols

α, β, δ	Exponent of strain	[-]
χ	Poynting coefficient	$[N/m^2]$
ϵ	Dilation in xy plane	[-]
γ	Shear strain	[-]
κ	Bulk modulus	$[N/m^2]$
λ	Pure shear in xy plane	[-]
$\Lambda_1, \Lambda_2, \Lambda_3$	Coefficients of σ_{xy}	$[N/m^2]$
λ_2, λ_3	Transverse deformation gradient	[-]
Λ_L	First Lamé parameter	$[N/m^2]$
λ_L	Coefficient of σ_{zz}	[-]
μ	Shear modulus	$[N/m^2]$
ν	Poisson's ratio	[-]
ϕ_0	Applied angle of rotation	[degree]
σ_{ij}	Cauchy stress	$[N/m^2]$
τ	Applied angle over gap	[degree$/m$]
ξ	Transverse deformation gradient used in $\mathbf{F}_g$	[-]

Roman Symbols

B	Left Cauchy-Green tensor	[-]
C	Right Cauchy-Green tensor	[-]
E	Green-Lagrangian strain tensor	[-]
$\mathbf{F}, \mathbf{F}_1, \mathbf{F}_g$	Deformation gradient tensor	[-]
P	First Poila-Kirchhoff stress tensor	$[N/m^2]$
S	Second Poila-Kirchhoff stress tensor	$[N/m^2]$
$\tilde{I_1}, \tilde{I_2}$	First and second isochoric strain invariant	[-]
c	Stiffness coefficient	[-]
e	Error	[%]
F_{nc}	Strain energy density function of n filaments	$[N/m^2]$
H	Gap of the cylinder	[m]
I_1, I_2, I_3	First, second, and third strain invariant	[-]

J	Volume ratio	[-]
k_B	Boltzmann constant	$[J/K]$
R, Θ, Z	Cylindrical reference configuration	
r, θ, z	Cylindrical deformed configuration	
R_0	Radius of cylinder	$[m]$
$T_\xi, T_{\sigma_{zz}}$	Torque	$[N \cdot m]$
T_{ij}	Reaction stress	$[N/m^2]$
W	Strain energy density	$[N/m^2]$
x	End-to-end ratio	[-]

1

Introduction

Complex fluids and soft solids, often referred to as ”soft matter,” play crucial roles in numerous practical domains, including medicine, food, personal care products, and pharmaceuticals. They also find innovative applications in fields like robotics and prosthetics. Notable examples encompass soft robots with the remarkable abilities to jump, roll, and bend; soft robotic gloves designed to assist patients in regaining hand functionality; and insect-inspired sensors capable of traversing water surfaces while detecting parameters such as pH values. Consequently, our attention is drawn to the stress-strain behaviors exhibited by soft matter, given their widespread relevance and transformative potential in various applications.

Our primary objective in this study is to investigate the Poynting effect within the context of soft matter. The Poynting effect involves the response of normal stress or strain in the transverse direction when subjected to shearing forces. It derives its name from the physicist John Henry Poynting, who first observed and described this phenomenon back in 1909. Despite several decades of observation and research, it remains remarkable that simple shear does not exclusively result in shear stress, as the Poynting effect also comes into play.

The significance of the Poynting effect in the field of soft matter is particularly noteworthy due to the material’s inherent ability to deform, meaning it can undergo significant deformation even under the influence of minor external forces. This unique characteristic of soft matter results in a pronounced Poynting effect, underscoring its importance in this context.

In the subsequent sections of this chapter, we will provide an in-depth exploration of the Poynting effect.

1.1. Poynting effect and Normal stress

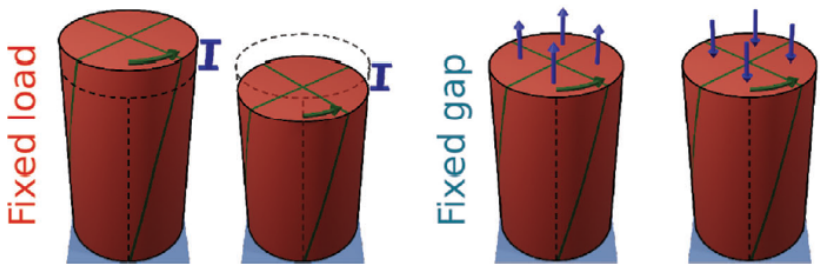

Figure 1.1: An illustration of the Poynting effect in (left) a non-confined and (right) a confined setups. In a non-confined setup, the load is fixed, while the material elongates or shortens upon shear. In a confined setup where the gap between the plates is fixed, the material will exert tensile or compressive stress on the confined configuration in order to keep the height constant [45].

The initial observation of the Poynting effect dates back to 1909 when J. H. Poynting conducted an experiment [25]. In this experiment, a wire was subjected to torsion while simultaneously being extended in the perpendicular direction. Poynting's investigation yielded two key pieces of evidence, leading to the conclusion that the application of shear forces could result in material deformation in the perpendicular direction.

Firstly, it was established that the thermal effect was not the primary cause of the observed elongation, as thermal expansion accounted for only a mere $1/100$ of the observed extension. Secondly, a crucial finding was the direct proportionality between the amount of lengthening and the square of the twist, signifying a robust correlation between these two variables. As a result of these observations, this phenomenon, where a material deforms in the transverse direction under shear, became known as the "Poynting effect."

Successive research efforts have revealed that this lengthening phenomenon is not uniform across all materials. Instead, the effect can be further categorized into two distinct types: the positive Poynting effect and the negative Poynting effect.

To gain a deeper comprehension of the Poynting effect, let's consider a straightforward scenario involving the shearing of a cylinder. When a cylinder undergoes shear, certain systems exhibit expansion, a phenomenon referred to as the positive Poynting effect. Consequently, when a fixed load is applied to the cylinder, it elongates in the transverse direction, as depicted in Figure (1.1) on the left side of the pair marked with the fixed load. On the other hand, when the gap of the cylinder is maintained constant, this expansion is halted. Eventually, the system exerts an outward force on the confining surfaces, as illustrated in Figure (1.1) on the right side of the pair denoted by the fixed gap. Alternatively, one can say that the system experiences a compressive force exerted by the container. Following sign convention as depicted in Figure (1.2), compressive normal stresses are considered negative. Therefore, a positive Poynting effect corresponds to a negative normal stress under confinement.

Similarly, if the cylinder tends to contract under shear, then in a fixed load scenario, the system will contract in the transverse direction. When the cylinder's gap is held constant, the system exerts an inward force on its container, namely, experiences tensile stress applied by the container. In most materials, elongation occurs during shear, demonstrating a positive Poynting effect. However, in the case of soft materials like biopolymers or rubber-like substances, negative normal stress may also emerge.

Earlier investigations have uncovered that the sign of the Poynting effect is not exclusively dictated by material properties alone; additional factors, including geometrical considerations, significantly influence this sign. This phenomenon becomes evident in devices like cone-plate and parallel-plate rheometers, where opposing signs of Poynting effects can be observed.

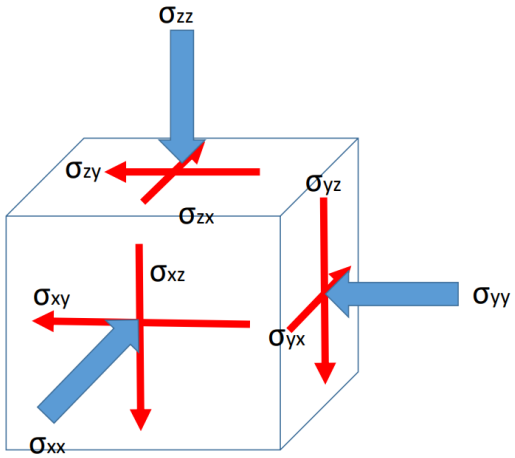

Figure 1.2: The sign convention provides a set of rules that guide the determination of the sign of the applied stress, denoted as σ, acting on a material.

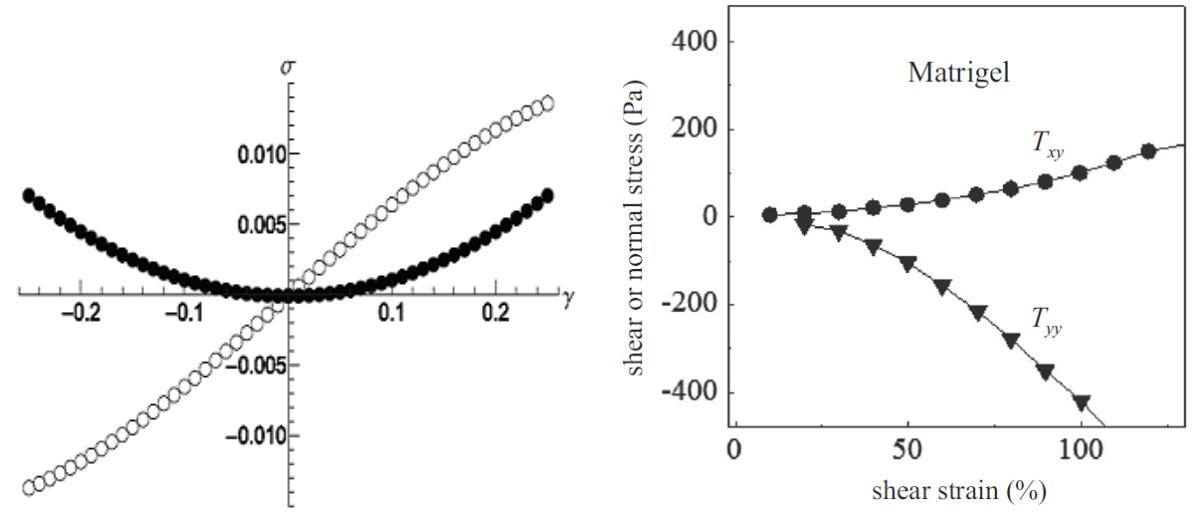

(a) (b)

Figure 1.3: The variables σ and T_{yy} correspond to $-\sigma_{zz}$, as illustrated in Figure (1.2). (a) depicts a theoretical analysis of the normal stress (●) and shear stress (○) responses concerning shear strain [27]. A positive normal stress indicates a positive Poynting effect. (b) illustrates that the shear stress response is linear when the shear strain γ is small. Within the hyperelasticity region, the response becomes nonlinear [39]. Notably, when subjected to shear, matrigel exhibits a negative Poynting effect.

As the Poynting effect revolves around the connection between shear strain and the resultant normal stresses, certain conclusions can be derived. For instance, the normal stress σ_{yy} should exhibit symmetry under simple shear, whether it is applied in the positive direction γ or the negative direction $-\gamma$. This symmetry implies that the resulting normal stress should maintain the same sign regardless of the direction of shear. The expression for the normal stress can be represented using Equation (1.1), and this relationship is visually depicted in Figure (1.3a) through the use of black dots.

$$\sigma_{yy}(\gamma) = \sum_{n=1}^{\infty} \alpha_n \gamma^{2n}, \quad n = 1, 2, 3, \ldots \tag{1.1}$$

In the case of a small but finite shear strain, it is commonly assumed that the relationship between shear strain γ and normal stress σ_{yy} follows a quadratic pattern. Conversely, shear stress exhibits antisymmetry when subjected to shearing, as illustrated in Figure (1.3a) using white dots. Importantly, the sign of the shear strain should indeed impact the sign of the resultant shear stress. The mathematical representation for shear stress is provided in Equation (1.2).

$$\sigma_{xy}(\gamma) = \sum_{n=1}^{\infty} \beta_n \gamma^{2n-1}, \quad n = 1, 2, 3, \ldots \tag{1.2}$$

In the case of a small but finite shear strain, it is a common practice to assume that the relationship between shear strain γ and shear stress σ_{xy} is linear. Later observations and analyses have consistently demonstrated that this assumption holds true, giving proof of its validity through numerical simulations [26] and experimental investigations [39].

Despite the extensive study of the Poynting effect over the years, continuous research, both experimental and numerical, continues to challenge and refine our previous understandings. In the following sections, we will present some experimental findings from prior investigations and explore the potential underlying causes of the Poynting effect and its associated signs.

1.1.1. Experimental research on Poynting effect

Early research into the Poynting effect dates back to 1950 when Rivlin conducted a series of experiments on rubber, specifically involving pure shear. His work helped establish the validity of strain energy

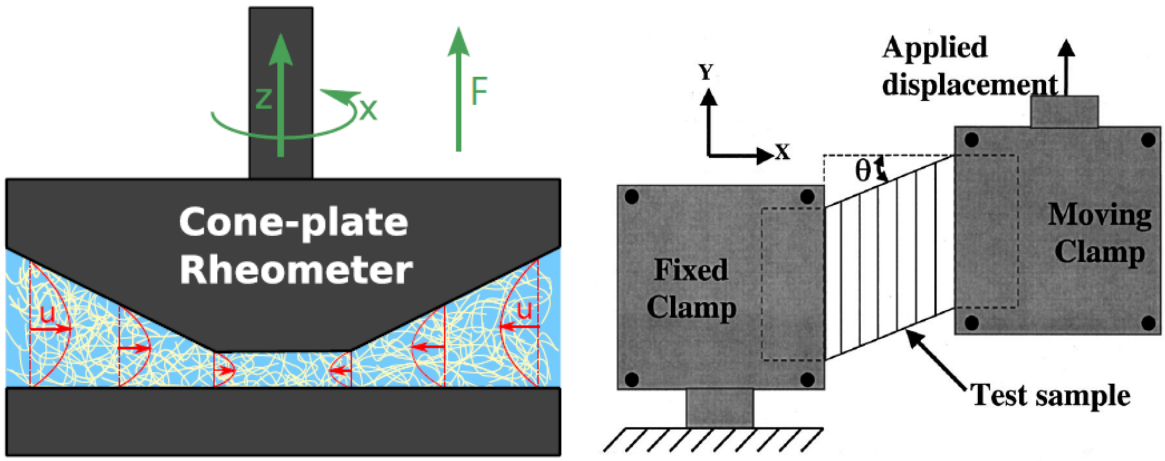

(a) (b)

Figure 1.4: The confined experimental setup for applying simple shear. (a) A cone-plate rheometer[2]. (b) The sample is clamped between a pair of fixed and moving clamps[21].

functions [44]. Subsequently, experiments using pantographic metamaterial, inspired by Poynting's observations, were conducted. These experiments demonstrated that the positive sign of the Poynting effect could change to negative as the twisting progressed. The deformation in these materials was governed by two mechanisms: (1) the beams forming the lattice underwent bending, and (2) two orthogonal families of beams rotated relative to each other. It was observed that when the deformation was primarily dominated by bending, the positive Poynting effect occurred [38].

In the case of semiflexible biopolymer gels, experimental results revealed a negative normal stress. Importantly, the magnitude of this negative normal stress increased only within the range where the systems stiffened under shear. When the shear modulus began to decrease, the magnitude of the negative normal stress also diminished. Furthermore, it was concluded that in a randomly oriented material, an equal number of filaments were elongated or compressed. However, due to the force-extension relation showing that stretched filaments exerted more force than compressed ones, this led to the emergence of negative normal stress [39].

Certain experimental studies have focused on brain cells, which are considered isotropic biological materials [35, 40]. Porcine brain matter, for instance, can be approximated as a Mooney-Rivlin material as long as the stretch remains below 60%. These studies have found that the Poynting effect is consistently positive, both through experimental observations and numerical simulations.

1.2. Proposal

Inspired by elastomers and biopolymers, our primary objective is to develop a model capable of accurately capturing the Poynting effect in isotropic, slightly compressible materials. In this research, we will begin by providing an overview of what constitutes soft matter and reviewing existing constitutive models for the strain energy of isotropic hyperelastic materials.

Given the suitability of Meng's model, based on continuum theory, for studying the Poynting effect, our analysis will primarily rely on this model. The model undergoes a transformation into an isochoric form to make way for the incorporation of the volumetric function. Following the discretization of both the isochoric and volumetric components, we will vary the Poisson's ratio to investigate the influence of compressibility on the Poynting effect. In Chapter 3, our analysis will utilize a two-variable simple shear deformation gradient tensor, while in Chapter 4, a more general tensor encompassing four variables will be employed to allow for the application of different boundary conditions.

Another crucial aspect of this thesis is the development of a method for predicting the sign of the Poynting effect under conditions of small but finite shear strain. This method relies on the concept of

Maxwell's relations, a multivariable calculus invariance that involves second derivatives. Upon deriving the relation, we will impose initial conditions based on various boundary conditions, ultimately resulting in an expression solely comprising material parameters. In this thesis, we demonstrate that the sign of the Poynting effect under small shear strain is predictably determined through the analysis of these material parameters. Furthermore, we explore the impact of boundary conditions on the strain-stiffening effect.

Following the numerical analysis, we will implement a simulation using the finite-element-based software Comsol. This simulation will investigate the simple shear of a cylinder, partly serving as a validation of our analytical findings. We anticipate that our simulation will also shed light on whether inhomogeneous deformation can influence the Poynting effect, particularly since the cylinder resembles parallel-plate rheometers—a common tool for studying the rheology of soft matter.

2

Literature Review

2.1. What is the soft matter?

Complex fluids and soft solids, collectively referred to as ”soft matter,” are prevalent in a wide array of practical applications, encompassing fields such as medicine, food production, personal care products, and pharmaceuticals. Soft matter comprises a diverse range of materials, falling into various categories, including polymers, biological tissues, and granular materials. At times, it can also show as a mixture of phases. In such cases, a solution qualifies as soft matter when the solute imparts structural properties to the solvent.

Different types of soft matter exhibit both shared characteristics and distinct attributes. One of the most prominent features common to soft matter is the lack of crystalline order. This characteristic allows soft matter to exhibit behavior that lies intermediate between that of solids and fluids [49]. Additionally, the characteristic length scale of the constitutive elements within soft matter typically falls within the mesoscopic range. Consequently, soft matter materials tend to have a low elastic modulus, meaning they display significant deformation in response to weak forces and exhibit nonlinear behavior.

Another notable trait of soft matter is its slow response. Soft matter typically forms extensive assemblies, and when subjected to deformation, the dynamics within these assemblies slow down significantly, occurring on the order of 1 to 10^4 seconds. This response time is considerably longer when compared to the rapid response of simple flows, which typically operates at the order of 10^{-9} seconds [50].

In the context of this research, our focus will be directed towards two distinct classes of polymeric soft matter: elastomers and biopolymers. The analysis is conducted under the quasi-static assumptions. This section has also presented an overview of various representative types of soft matter, including colloids, dispersions, and polymers.

2.1.1. Colloid

Colloid solutions represent a typical mixture type within the field of soft matter. These solutions consist of colloids, which are either fluid or solid particles dispersed within a liquid medium. The particle sizes in colloidal suspensions are relatively small, typically ranging from nanometers (nm) to micrometers (μm). A familiar example of a colloid solution is milk. In such solutions, the particles do not settle at the bottom due to the dominance of thermal fluctuations over gravity.

The dispersion of these small particles within the solvent, along with their Brownian motion, can have a significant impact on the rheological properties of the system. This influence can show in phenomena such as shear-thickening and viscoelastic behavior. In colloidal science, low-concentration colloidal solutions are often referred to as ”sol,” while high-concentration solutions are termed ”gel” [50].

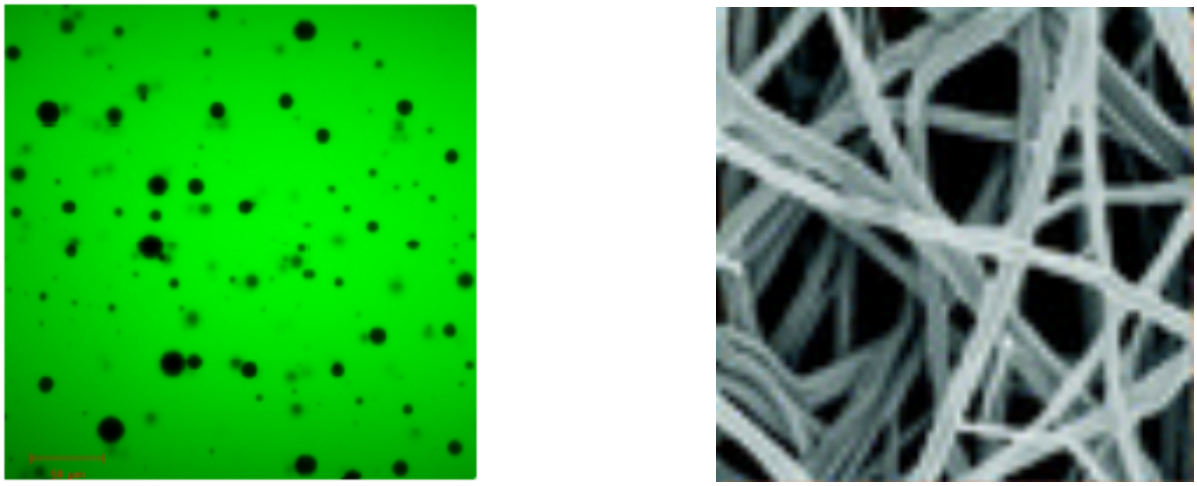

(a) (b)

Figure 2.1: (a) Image of emulsions of silicone oil droplets with 0.5 wt % in water stabilized by SDS [1]. (b) Electron microscopy image of a large-pore fibrin gel [57].

2.1.2. Dispersions

Dispersion, as shown in Figure (2.1a) is another prevalent category within the field of soft matter. It refers to a mixture comprising two phases: one phase that is spatially discontinuous and another that is continuous. The size of the particles involved in dispersions can vary widely, ranging from particles as small as sand grains to significantly larger entities such as icebergs. Notably, in dispersions, the particles are typically so large that thermal motion becomes negligible, and their movement is predominantly governed by inter-particle forces.

A diverse array of materials falls under the umbrella of dispersions, including granular materials (solid dispersed in a gas), suspensions (solid dispersed in a liquid), and foams (gas dispersed in a liquid). Granular materials, in particular, are characterized by disorder, high dissipation, and a pronounced nonlinear response to applied forces. The concept of jamming, where a granular system becomes immobilized in an amorphous state under static conditions, holds particular fascination for numerous researchers in this field [52].

2.1.3. Polymers

Polymers, ranging from natural to synthetic materials, constitute a significant category within the field of soft matter. These materials consist of long, chain-like structures composed of repeating monomer units. When polymers are stretched or straightened out, they have the potential to undergo crystallization. However, an interesting characteristic of polymers is that they often do not fully crystallize due to the substantial energy required for this process.

As a consequence, polymers tend to exhibit a wide range of structures that are better understood and characterized through their rheological properties rather than their molecular organization [49]. This inherent structural diversity and the role of rheology are fundamental aspects of polymers in the study of soft matter.

Natural polymers are ubiquitous, from silk to wood. Biological soft polymers are also abundant in human bodies, such as tissues, DNA, and polymeric carbohydrates. Biopolymer gel, which consists of semiflexible filament networks and liquid filling the interstitial space, specifically catches researchers' eyes because these materials are well-known for their stress-stiffening behavior under small strains, and also the compressibility that has been hypothesized to cause the negative Poynting effect [2].

Natural polymers are found abundantly in the natural world, ranging from materials like silk to wood. Within the human body, biological soft polymers are also prevalent, found in various tissues, DNA, and polymeric carbohydrates. Biopolymer gels, which comprise semiflexible filament networks within

a liquid-filled interstitial space, have garnered significant attention from researchers. These materials are renowned for their stress-stiffening behavior under small strains and their compressibility, which has been hypothesized to give rise to the negative Poynting effect [2].

In contrast, synthetic polymers play a crucial role in modern industry, with a particular focus on rubber. Rubber finds wide-ranging applications in products such as tires, absorbent materials for diapers, and even soft contact lenses [51]. Phenomenological behaviors of rubber have been extensively studied across a spectrum, from the dry state to the gel-like, swollen phase. A shared characteristic of rubber, and elastomers in general, is their remarkable reversibility even when subjected to substantial deformation and their ability to undergo large deformations in response to small external forces. One way to view rubbers is as networks of crosslinked filaments, as shown in Figure (2.1b), with the material being discretized as an assembly of small cells.

2.2. Hyperelasticity

Hyperelasticity is a term used to describe the nonlinear elastic behavior of materials like rubber when subjected to deformation. Rubber, in particular, is known for its ability to undergo significant strain in response to external forces, leading to a complex relationship between shear and strain. Also, hyperelasticity does not imply plasticity, which means that the deformation exhibited by hyperelastic materials is reversible. Therefore, there is no hysteresis loop observed in a loading-unloading cycle. In such cycles, the stress follows the same curve during both the loading and unloading phases, reflecting the material's elastic and reversible response to deformation.

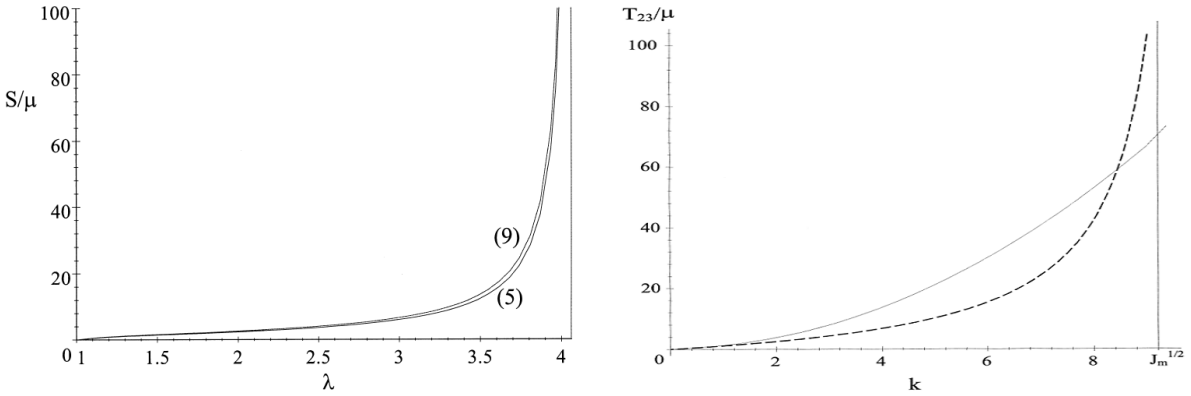

(a) (b)

Figure 2.2: The simulation of force response of rubber material shows the strain stiffening [8]. (a) The normal stress under simple extension. (b) The shear stress under simple shear.

Strain-stiffening effect is one of the manifestations of hyperelasticity. It means the materials stiffen or harden upon the large strain. A cause of strain-stiffening is that after the monomers of rubbers align with the direction of external force, in order to further stretch the material, the external force should be capable of pulling away the chemical bonds, and the energy required increases as the strain increases [18]. The phenomenon is considered critical in the field of biomedical because the elasticity of the biological tissue could change due to diseases or age. For example, the thoracic artery of a 70-year-old male stiffens five times more than that of a 21-year-old [16]. Upon stretching, isotactic rubbers crystallize and go through strain-stiffening. The atactic rubber-like materials, referring to the materials that have no regular configuration, stiffen because of the finite chain extensibility [18].

The deformation of hyperelastic materials is quantified using a deformation gradient tensor denoted as **F**. This tensor is defined as the derivative of the deformed coordinates **x** with respect to the undeformed coordinates **X** [9]. In this context, **x** represents the deformed state, while **X** represents the undeformed state.

Given a tensor **F**, we can determine the energy density function W, which characterizes the amount of energy stored per unit volume in the material. Since rigid body motion does not store energy, the

function W solely depends on the deformation gradient tensor **F**. W can be expressed as a function of invariants, namely I_1, I_2, and I_3, or principal strains, denoted as λ_1, λ_2, and λ_3. Strain invariants are derived from the deformation gradient tensor and are typically preferred because they describe deformation without being influenced by the choice of coordinate system.

To calculate these invariants, the Left Cauchy-Green deformation tensor, represented as $\mathbf{B} = \mathbf{F} \cdot \mathbf{F}^T$, is introduced. The invariants I_1, I_2, and I_3 are then defined, as described in Equation (2.1). I_1 and I_2 are particularly sensitive to shear deformation, while I_3 characterizes the dilational deformation of the material.

$$I_1 = tr(\mathbf{B}), \qquad I_2 = \frac{1}{2}({I_1}^2 - tr(\mathbf{B}^2)), \qquad I_3 = det(\mathbf{B}) = J^2. \tag{2.1}$$

Working with a strain energy function offers an advantage in that this single function encodes the stress response that arises from arbitrary deformations. It allows us to establish a relationship between the strain energy function W and two definitions of stress tensors: the first Piola-Kirchhoff stress tensor denoted as **P** and the second Piola-Kirchhoff stress tensor denoted as **S**. These tensors represent the force per unit area acting on the deformed and undeformed states, respectively.

$$\begin{aligned} \mathbf{P} &= \partial W / \partial \mathbf{F}, \\ \mathbf{S} &= J^{-1}(\partial W / \partial \mathbf{F})\mathbf{F}^T \end{aligned} \tag{2.2}$$

Furthermore, the relationship between the Cauchy stress tensor $\sigma 0$ can also be expressed as described in Equation (2.3).

$$\boldsymbol{\sigma} = \frac{1}{J}\mathbf{F}\mathbf{S}\mathbf{F}^T \tag{2.3}$$

2.2.1. Strain-energy functions for incompressible mateirals

The scientific literature encompasses a wide range of strain energy functions designed for hyperelastic materials. Each function corresponds to a distinct model, and these models vary in their characteristics and objectives. Some models provide a highly precise representation of a specific physical system, resulting in intricate formulations with numerous fitting parameters. Conversely, other models prioritize simplicity, emphasizing ease of analysis and qualitative insights over quantitative precision.

In this section, we offer an overview of various strain energy functions that bear relevance to the investigation of the Poynting effect. However, it is important to note that this thesis will ultimately concentrate on a specific model system, which will be described in greater detail in the next section.

Many materials exhibit nearly incompressible behavior, meaning that they require significantly more energy to induce volumetric strain compared to an equivalent shear strain. Therefore, many modeling approaches adopt an assumption that treats the material as perfectly incompressible, which causes volume changes impossible. This assumption results in setting parameters such as I_3 and J to equal one, making the strain energy function solely dependent on I_1 and I_2.

This section will review several relevant incompressible models, as shown in Table (2.1), while the following section will introduce models that account for compressibility.

The neo-Hookean model, shown in Equation (2.4), is not only a classical example of an incompressible material but also an example of isotropic materials. These isotropic, incompressible, hyperelastic materials are found in everyday life, such as natural rubber, synthetic elastomers, and biological tissue [12].

$$W = \frac{\mu}{2}(I_1 - 3) \tag{2.4}$$

One of the simplest forms of the strain energy function is the Gent model, which is expressed as shown in Equation (2.5).

$$W = \frac{-\mu}{2} J_m ln(1 - \frac{I_1 - 3}{J_m}), \tag{2.5}$$

where J_m is the limiting value for $I_1 - 3$. For incompressible materials, if the limiting value J_m tends towards infinity, the equation is further reduced to the neo-Hookean form [8].

The Mooney-Rivlin model is another well-known model for incompressible isotropic materials, alongside the neo-Hookean model. It is represented as a linear combination of the I_1 and I_2 terms.

$$W = \frac{\mu}{2}(I_1 - 3) + \frac{\kappa}{2}(I_2 - 3) \tag{2.6}$$

The importance of incorporating the second invariant I_2 when predicting the strain stiffening effect has been emphasized in references [16, 32]. Some models, such as the neo-Hookean model, exclusively rely on the first invariant I_1 and consequently may not fully capture certain features of real systems' responses.

In reference [16], the Vito model, which includes the second invariant term, is shown to provide a better fit to the deformation characteristics of real systems compared to the first-invariant-dependent FD model. For instance, the Vito model exhibits improved agreement with the results of the simple extension test conducted on the dog aorta.

Furthermore, the inclusion of I_2 has been demonstrated to be crucial for accurately capturing the Poynting effect. The significance of I_2 is also investigated by A. Anssari-Benam et al. using an elementary approach to molecular theory [32]. Strain-energy functions that are additive in nature and incorporate I_2 have been shown to better match the results of uniaxial tensile tests compared to the generalized neo-Hookean model, as illustrated in Figure (2.3).

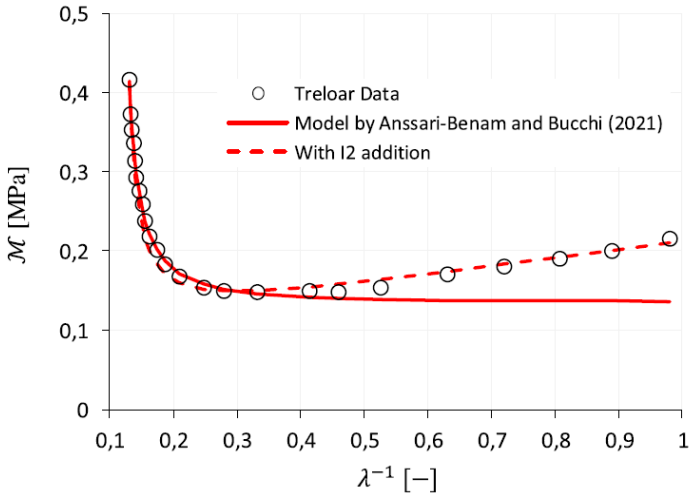

Figure 2.3: The comparison shown in the figure between experimental data (Treloar data) and two sets of numerical data presents the reduced engineering stress M plotted against extension λ during uniaxial deformation [32]. The Anssari-Benam and Bucchi model, which relies solely on I_1, fails to accurately capture the upturn observed in the experimental data. However, by incorporating the term $C_2(I_2 - 3)$ into the model, a much better fit is achieved, aligning the numerical results more closely with the experimental data.

Treloar and Jones' classical experiment on natural rubber has inspired several papers to investigate the fitting of hyperelastic models to the experimental data. R. W. Ogden et al. conducted a study on fitting hyperelastic models, as described in reference [20]. They calculated the relative errors between the fitted parameters and the experimental data for comparison.

In their analysis, the Pucci-Saccomandi model is shown to be a relatively poor fit for biaxial testing. On the other hand, the Ogden model, which is an M-summation function containing M different shear modulus terms and M terms to form a strain energy function, provides good fits for equi-biaxial tension. However, it is observed that the relative error is significant for small strains, regardless of the type of test conducted. Notably, the research demonstrates that increasing the value of M to 4 does not necessarily reduce the error compared to the case with M equal to 3.

Table 2.1: Strain-energy functions W for incompressible materials.

Lopez-Pamies (2009)[19]	$\frac{3^{1-\alpha_1}}{2\alpha_1}\mu_1(I_1^{\alpha_1}-3^{\alpha_1})+\frac{3^{1-\alpha_2}}{2\alpha_2}\mu_2(I_1^{\alpha_2}-3^{\alpha_2})$
Special Blatz-Ko (1962)[53]	$C(I_2+2I_3-5)$
Fung-Demiray (1972)[16]	$\frac{\mu}{2b}(e^{b(I_1-3)}-1)$
Vito (1973)[16]	$\frac{\mu}{2b}(e^{b(\alpha(I_1-3)+(1-\alpha)(I_2-3))}-1)$
Anssari-Benam(1) (2021)[32]	$\mu N\left[\frac{1}{6N}(I_1-3)-\ln\left(\frac{I_1-3N}{3-3N}\right)\right]+C_2(I_2-3)$
Anssari-Benam(2) (2021)[32]	$\mu N\left[\frac{1}{6N}(I_1-3)-\ln\left(\frac{I_1-3N}{3-3N}\right)\right]+C_2\left(\sqrt{\frac{I_2}{3}}-1\right)$
Anssari-Benam(3) (2021)[32]	$\mu N\left[\frac{1}{6N}(I_1-3)-\ln\left(\frac{I_1-3N}{3-3N}\right)\right]+C_2\left(\frac{I_2}{3}\right)$
Pucci-Saccomandi (2002)[20]	$-\frac{\mu}{2}J_m\log\left(1-\frac{I_1-3}{J_m}\right)+C_2\log\left(\frac{I_2}{3}\right)$
Ogden M-summation (2004) [20]	$\sum_{i=1}^{\infty}\frac{\mu_i}{\alpha_i}(\lambda_1^{\alpha_i}+\lambda_2^{\alpha_i}+\lambda_3^{\alpha_i}-3)$

Another I_1-based model for rubber is proposed by O. Lopez-Pamies. This closed-form model is developed based on the generalized neo-Hookean model and is characterized by its simplicity. Researchers fit the four-parameter model with experimental data and demonstrate that the model exhibits a high degree of similarity to the Gent model for rubber under uniaxial tension, biaxial tension, and pure shear [18]. It is worth noting that the Gent model also shows a more pronounced strain-hardening phenomenon compared to the power-law model.

2.3. Hyperelasticity with Compressibility

Rubber-like materials are often treated as incompressible as long as the hydrostatic stress remains relatively small. This assumption is based on the idea that these materials can maintain their volume under large deformations. However, in reality, even rubber-like materials exhibit some degree of compressibility. In hyperelasticity, this compressibility is accounted for in some models.

The simplest form of the neo-Hookean model, which considers compressibility, can be expressed as shown in Equation (2.7), where Λ_L represents the Lamé parameter.

$$W=\frac{\mu}{2}(I_1-3-2\ln J)+\frac{\Lambda_L}{2}(J-1)^2 \tag{2.7}$$

Compressibility in hyperelastic models is represented by terms involving the volume ratio denoted as J. If a material is considered incompressible, then J equals 1, and the corresponding terms disappear from the equations. In practice, incompressibility is an idealized assumption aimed at simplifying the elastic response function [15]. The bulk modulus for rubber is not infinitely large; rather, it is larger than the shear modulus. The compressibility of rubber has also been studied experimentally by Adams and Gibson [10].

For strain-energy functions designed to describe compressible materials, as opposed to classical incompressible materials, these functions must still adhere to three classical initial conditions, as mentioned in [12]. These conditions are: (1) the strain energy is zero in the reference configuration; (2) the stress is zero in the reference configuration; and (3) on restriction to infinitesimal deformations, the shear and bulk moduli, μ and κ, are positive, or equivalently, the strain-energy function is positive definite.

Defining the strain energy as $W=\psi(\lambda_1,\lambda_2,\lambda_3)+F(J)$, where $x_i=\lambda_i X_i$ (no summation) and therefore $J=\lambda_1\lambda_2\lambda_3$, we can translate these conditions into equations as follows:

$$\psi(1,1,1)+F(1)=0, \qquad \psi_{,i}(1,1,1)+F'(1)=0 \tag{2.8}$$

$$3\kappa=2\psi_{,ij}(1,1,1)+\psi_{,ii}(1,1,1)+2F'(1)+3F''(1), \qquad 2\mu=\psi_{,ii}(1,1,1)-\psi_{,ij}(1,1,1)-F'(1) \tag{2.9}$$

The material of interest in this study is nearly incompressible, which means that the determinant J of such materials is close to 1, or $J \to 1$. This suggests that for materials with slight compressibility, the Poisson's ratio ν should be close to 0.5 [13], or alternatively, the ratio $\eta = \mu/\kappa$ should be much less than 1 [12]. A characteristic of nearly incompressible materials is that they tend to soften in tension and harden in compression. The assumption of slight compressibility is also adopted by commercial Finite Element Method (FEM) software to prevent element locking [14].

Continuing from the conditions mentioned in equations (2.8) and (2.9), it is further assumed that the strain-energy function ψ depends on the shear modulus μ, and the volumetric function F depends on the bulk modulus κ. It is a requirement that the stress is zero in the reference configuration.

$$\kappa = F''(1), \qquad F(1) = F'(1) = 0 \tag{2.10}$$

The compatibility with the classical linear form of the strain-energy function on restriction to infinitesimal deformations also needs to be ensured:

$$\begin{gathered} 2\psi_{,ij}(1,1,1) + \psi_{,ii}(1,1,1) = 0, \qquad 2\mu = \psi_{,ii}(1,1,1) - \psi_{,ij}(1,1,1), \\ \psi_{,ij}(1,1,1) = \psi_{,i}(1,1,1) = 0. \end{gathered} \tag{2.11}$$

Table 2.2: Strain-energy functions W for compressible materials.

Christensen (1988)[12]	$\frac{\mu}{2}(I_1 - 3J^{2/3}) + \frac{3\kappa}{2}(\frac{3}{2}J^{2/3} - ln(J) - \frac{3}{2})$
Levinson (1972)[12]	$\frac{\mu}{6}(3I_1 - 4J - 2ln(J) - 5) + \kappa(J - ln(J) - 1)$
Levinson-Burgess (1971)[12]	$\frac{\mu}{6}(3I_1 - J^2 - 8J - 2) + \frac{\kappa}{2}(J-1)^2$
Ehlers-Eipper (1998)[12]	$\frac{\mu}{2}(I_1 J^{-2/3} - 3) + \frac{\kappa}{2}(lnJ)^2$
Horgan-Murphy (2006)[12]	$c_1\left(\lambda_1^m + \lambda_2^m + \lambda_3^m + \frac{4\epsilon}{1-2\epsilon}J^{\frac{(2\epsilon-1)m}{4\epsilon}} - \frac{3-2\epsilon}{1-2\epsilon}\right) +$ $c_2\left(\lambda_1^{-m} + \lambda_2^{-m} + \lambda_3^{-m} + \frac{4\epsilon}{1-2\epsilon}J^{-\frac{(2\epsilon-1)m}{4\epsilon}} - \frac{3-2\epsilon}{1-2\epsilon}\right)$
Horgan-Murphy (m=2)	$\frac{\mu f}{2}\left(I_1 - 3 - \frac{2}{\gamma}(J^\gamma - 1)\right) + \frac{\mu(1-f)}{2}\left(I_2 J^{-2} - 3 - \frac{2}{\gamma}(J^\gamma - 1)\right)$

Numerical research [12] has demonstrated significant deviations between the Christensen model, Levinson model, Levinson and Burgess model, and the Ehlers and Eipper model from experimental data. Additionally, when the deformation tensor (2.12) is used to describe simple shear, and because $J = 1$, the deformation is isochoric, and the stress response for almost incompressible materials in this case is independent of the volume ratio J.

$$\mathbf{F} = \begin{bmatrix} 1 & \gamma & 0 \\ 0 & 1 & 0 \\ 0 & 0 & 1 \end{bmatrix} \tag{2.12}$$

2.3.1. Volumetric part of constitutive models

For simplicity in computation, it is often assumed that the strain energy function can be divided into an isochoric part and a volumetric part. In this approach, the deviatoric functions introduced in section 2.2 can be combined with the volumetric function to describe deformation with dilation. To discretize the function, it is often rewritten as equation (2.13). $\tilde{I_1}$ and $\tilde{I_2}$ denote the first and second invariants of the isochoric-elastic right Cauchy–Green deformation tensor. By using isochoric strain invariants, $\tilde{\psi}$ describes only the isochoric deformation of the system, and $F(J)$ describes only the volumetric deformation, thus separating the two parts.

$$\begin{gathered} W = \tilde{\psi}\left(\tilde{I_1}, \tilde{I_2}\right) + F(J), \\ \tilde{I_1} = \frac{I_1}{J^{2/3}}, \qquad \tilde{I_2} = \frac{I_2}{J^{4/3}} \end{gathered} \tag{2.13}$$

Several proposals for models describing the volumetric part $F(J)$ have been made over the years, as shown in Table (2.3). When the volume change is small, namely, when $I_3 \leq 1$ or $1 \leq I_3 \leq 1.0003$, researchers have found that the formulation of the energy density function in equation (2.13) provides a good fit to the tension-volume change data of rubber [33]. In [15], the function W is further assumed to be independent of I_2. In this simplified model, the effect of limiting chain extensibility is found to stiffen the material relative to the neo-Hookean compressible case. A proposal made by Anssari-Benam and Horgan not only complies with the requirement that W_{Vol} should approach infinity when $J \to \infty$ or $J \to 0$, but it is also capable of predicting a wide range of deformation behaviors for a wide range of elastomers. It can also be derived from experimental data. By utilizing the relation between hydrostatic pressure and the volume change J obtained from experiments on porcine liver tissues, which are slightly compressible, an impression for the volumetric function is derived [56].

Table 2.3: Volumetric part of strain-energy functions W_{vol}.

Blatz-Ko (1962) [55]	$J - \ln(J) - 1$
Valanis-Landel (1967) [55]	$\frac{\kappa}{2}(\ln J)^2$
Simo-Taylor (1982) [55]	$\kappa\left[(J-1)^2 - (\ln J)^2\right]$
Bischoff et al. (2001) [55]	$\frac{\kappa}{\beta^2}(cosh(\beta J - \beta) - 1)$
Wang et al. (2020) [56]	$\frac{\kappa}{2}\frac{J^{\alpha+1}[(\alpha+1)\ln J-1]+1}{(\alpha+1)^2} - \frac{\kappa}{2}\frac{J^{-\alpha+1}[(\alpha-1)\ln J+1]-1}{(\alpha-1)^2}$
Anssari-Benam and Horgan (2022) [55]	$\frac{\kappa}{4}(J^2 - 1 - 2\ln J)$

2.3.2. Deformation tensor for Compressible Material

Applying the deformation tensor in (2.12), the stress response is independent of the volumetric function $F(J)$ since the volume ratio equals one. However, despite its apparent reasonability, this model does not match the experimental data. Therefore, alternative models have been studied. M. Destrade et al. argue that the isochoric approximation of simple shear is too restrictive and that an infinitesimal volume change should always be included [23]. To account for this infinitesimal volume change, the following approach is adopted:

$$x_1 = (1+\epsilon_1)X_1 + \gamma(1+\epsilon_2)X_2, \qquad x_2 = (1+\epsilon_2)X_2, \qquad x_3 = (1+\epsilon_3)X_3 \tag{2.14}$$

The deformation gradient tensor can be derived using equation (2.14) and then applied to the energy density function W to calculate the stress responses. It has been found that while the shear stress is still independent of Poisson's ratio ν, the normal stress responses upon shearing become sensitive to the choice of ν. Instead of simply setting the ratio to 1/2, the research suggests that since no material is perfectly incompressible, even a change of the third decimal of Poisson's ratio, ranging between 0.495 to 0.5, can result in a significant change in response, such as the reverse Poynting effect.

The Poynting effect, which indicates normal stress induced by simple shear, has been noted by several researchers, including M. Destrade et al., who stated that simple shear would not result in simple shear stress [23]. To express a more general deformation for simple shear, the research suggests that the principal elements in the deformation gradient tensor should not equal one, thereby increasing the degree of freedom in the analysis.

2.3.3. Compressibility in biological matters

Research on biopolymers has highlighted that the presence of compressibility is a prerequisite for materials to exhibit contraction under shear forces, a point we will delve into further in subsequent discussions [1]. In the context of cone-plate geometry, it becomes evident that when dealing with materials that are both incompressible and elastic, two key observations emerge: (1) the thrust applied to the rheometer head is directly proportional to the first normal stress difference, and (2) the first normal stress difference consistently holds a positive value. This implies that the Poynting effect is consistently positive in such scenarios. This insight naturally leads to the conclusion that for an elastic system to

display a negative Poynting effect, it must possess compressibility. The experiments conducted by Bonn et al indirectly confirm this understanding. To illustrate, compressibility can be achieved through a high water content. When water cannot readily exit the material in a short time frame, it renders the material incompressible. Conversely, when the material undergoes slow deformation, it becomes compressible as water can be gradually squeezed out. In our research, we focus exclusively on elastic models, assuming quasi-static deformation.

2.4. What influences the Poynting effect?

2.4.1. Nonlinearity and Poynting effect

Hyperelasticity, which characterizes the nonlinear response of soft matter, has a subtle but important role in understanding the Poynting effect, even though it has not been explicitly discussed in previous chapters.

The connection between the Poynting effect and nonlinearity can be inferred from the behavior of constitutive models. As previously discussed in subsection 2.2.1, the second invariant, denoted as I_2, is crucial for capturing the strain-stiffening effect, a typical nonlinear characteristic of biopolymers. Therefore, it is not surprising that models like the FD model, which lacks the I_2 term, fail to represent the Poynting effect, while models like the Vito model can account for compressive traction [16]. As a result, the inclusion of the second invariant term I_2 is essential for exponential models to accurately depict the Poynting effect in isotropic rubber-like and soft biomaterials.

Regarding the sign of the Poynting effect, geometric nonlinearities are identified as one of the factors contributing to the negative Poynting effect in filamentous biopolymers. While buckling is a significant contributor, arising from the asymmetric force-distance curve, it is not the sole cause of negative normal stress. Filament network theory, to be discussed in section 2.4.4, introduces various length scales for categorizing material deformation. For instance, l_p represents the persistence length, representing the stiffness or rigidity of a polymer chain, while L_c denotes the contour length of the chain.

The research findings suggest that, within the context of a quadratic spring model featuring a quadratic term in the force-extension relationship, the interaction between geometric and elastic nonlinearities is balanced when the persistence length (l_p) is approximately equal to the contour length (L_c). However, when L_c is much smaller than l_p, elastic nonlinearity becomes the primary factor governing normal stress. Additionally, the study observes a transition in the elastic response as shear strain increases from infinitesimal to large values, shifting from a quadratic behavior to a linear one.

2.4.2. Effect of Compressiblity

In the context of incompressible materials, where the volume remains constant, positive normal stress often exerts on the materials, or expansion in the transverse direction. However, for nearly incompressible materials, it is possible for the volume to contract, resulting in inward contraction. Achieving compressibility in materials, particularly in biopolymers, can occur through various means. For instance, semiflexible polymer hydrogels can exhibit compressibility because the water within the hydrogel can be squeezed out over time [2]. This compressibility can be characterized by the ”characteristic relaxation time,” meaning that if the system has sufficient time to react (i.e., squeeze out the water), it can undergo contraction. It is worth noting that this model generally applies to two-phase materials, but similar phenomena can also be observed in single-component materials.

Another experiment provides a direct comparison between foam and adhesive oil-in-water emulsions under shear, illustrating that compressibility can lead to opposite signs of the Poynting effect [1]. Foam, which exhibits a positive Poynting effect, tends to expand or push outwards on the rheometer under shear. In contrast, emulsions may display a negative Poynting effect, indicating that they can contract under shear. The compressibility of emulsions is achieved through a porous network structure, and it depends on the concentration of the surfactant. This type of geometry allows the solute to be squeezed out of the material, similar to the water in biopolymer gels. When the surfactant concentration is low, the biopolymer gel resembles a foam-like structure with little structural change. Incompressibility leads the system to exhibit repulsion and a positive Poynting effect. Conversely, emulsions with high sur-

factant concentration form large aggregates and gel-like structures, potentially resulting in a negative Poynting effect. Importantly, the compressibility is determined prior to shear, and thus, the sign of the Poynting effect is predefined. Experimental data further validate the quadratic relationship between normal stress and shear strain.

A key conclusion drawn from this is that to exhibit a negative Poynting effect, the shear modulus of a material should stiffen in response to stretching. Using a specific strain tensor, this relationship is derived analytically and found to align with experimental data. In this context, a Poynting coefficient χ is introduced, where F_y represents the thrust in the perpendicular direction, and ξ_y denotes the dimensionless dilation in the gradient direction. For materials like sticky adhesives, which form networks and remain unchanged unless subjected to a tensile force exceeding a certain threshold, placing such a network under tension increases its shear modulus, resulting in a positive derivative $(\frac{\partial G}{\partial \xi_y})$ and, consequently, a negative Poynting effect.

$$\chi = [(\frac{\partial^2 F_y}{\partial \gamma^2})_{\xi_y}]_0 = -[(\frac{\partial G}{\partial \xi_y})]_0 \tag{2.15}$$

Poisson's ratio offers a convenient means of quantifying a material's compressibility. The relation between the bulk modulus, shear modulus, and Poisson's ratio is defined as follows

$$\nu = \frac{3\kappa - 2\mu}{2(3\kappa + \mu)} \tag{2.16}$$

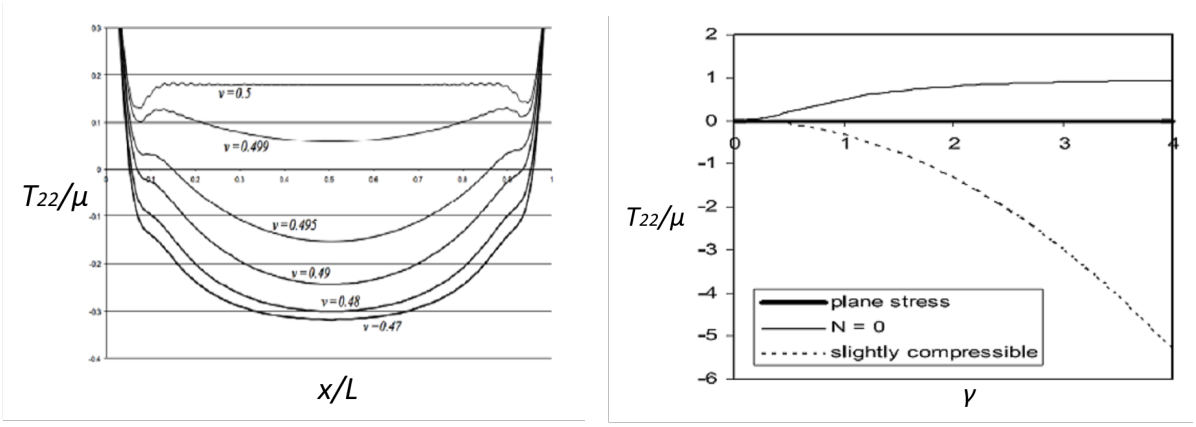

(a) (b)

Figure 2.4: (a) The sensitivity of the dimensionless transverse normal stress, expressed as $T_{yy}/\mu = -\sigma_{yy}/\mu$, is demonstrated across different positions along the horizontal centerline of the block for various values of $\nu = 0.5, 0.499, 0.495, 0.49, 0.48, 0.47$. The closer ν is to 0.5, the easier the normal stress $-\sigma_{yy}$ becomes positive, resulting in a positive Poynting effect [23]. (b) The nondimensional transverse normal stress σ_{yy}/μ under the assumption of (solid, bald line) plane stress, assuming that the stress on slanted faces σ_{zz} equals zero; (solid line) zero normal traction, assuming that the normal stress on slanted faces is equals zero; and slight compressibility (dashed line) [14].

The degree of compressibility in a material is closely tied to its Poisson's ratio, denoted as ν. In the limit where the bulk modulus κ significantly outweighs the shear modulus μ, namely, $\kappa/\mu \to \infty$, a material can be considered incompressible. As a result, for compressible materials, their Poisson's ratio ν is typically less than 0.5. Research has highlighted the considerable sensitivity of the Poynting effect to the specific value of Poisson's ratio ν. In one study [23], it is demonstrated that by making minor adjustments to the third decimal place of ν within the range of [0.495, 0.5], the sign of the Poynting effect can be altered, as depicted in Figure (2.4a). Therefore, the choice of ν should be made with precision. The study challenges the common statement that "slight compressibility does not warrant special attention for plane stress," which is sometimes provided by commercial software like Abaqus. Based on these findings, D. Wang and M.S. Wu propose a generalized simple shear displacement formulation, introducing linear and nonlinear deformations, which leads to a curved lateral profile of the

deformed block and the emergence of second-order in-plane shear T_{xy} [36]. Their research indicates that the closer ν is to 0.5 and the larger the shear modulus μ, the more likely it is for the Poynting effect to be positive. Additionally, it is worth noting that different assumptions about boundary conditions can yield distinct normal stress outcomes, as illustrated in Figure (2.4b).

2.4.3. Rubber and isotropic networks

The model extensively explored in Chapters 3 and 4 is commonly referred to as a ”micromechanical model.” In this subsection, we will introduce micromechanical models and provide an overview of their key characteristics.

To grasp the typical derivation of a micromechanical model, it is essential to consider its theoretical foundation - network theory. Rubbers and elastomers fall into the category of polymeric networks, which are materials composed of numerous smaller components. These smaller components are junctions or strands, indicating that monomers are linked either directly or indirectly. This concept allows us to break down these materials into small crosslinked filaments.

Due to this discretization, models based on network theory are often referred to as micromechanical models. These models aim to construct a strain energy function by starting with a description of the forces between individual polymer chains and then averaging these interactions over the entire network volume. The force-deformation relationship of a single monomer is usually determined experimentally or theoretically. For instance, Equation (2.17) describes the strain energy of a single semiflexible filament. In this equation, symbols like k_B and T represent the Boltzmann constant and temperature, respectively, while x and c refer to the end-to-end factor, which signifies the ratio of the distance between two ends of the polymer chain ξ_c to the total length of the chain L_C, and the dimensionless stiffness parameter, which reflects the competition between bending and thermal energy. However, effectively describing the motion of these polymer networks remains a challenge.

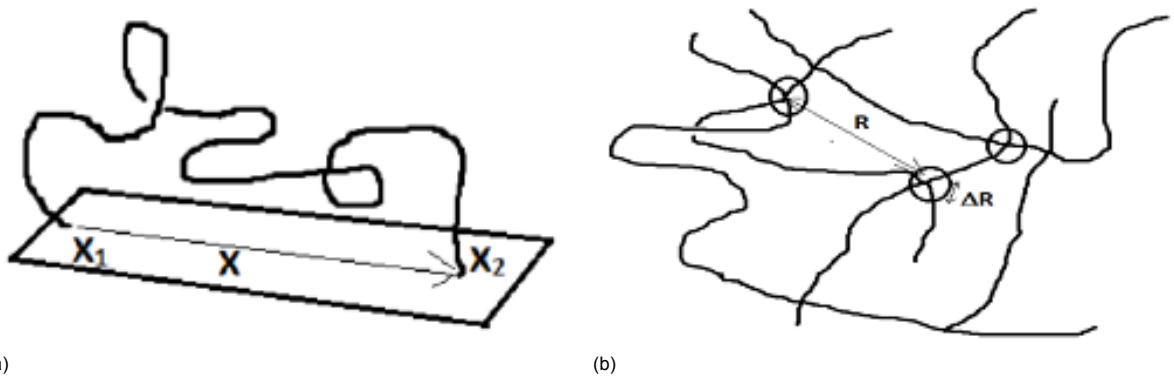

(a) (b)

Figure 2.5: Illustrations of (a) affine network, (b) phantom network [51]. The deformation of the affine network is defined based on the displacement of two ends. The deformation of the phantom network takes the entropy into account and is defined based on the displacement of the junctions. R denotes the displacement between 2 junctions, while ΔR denotes the fluctuation of the displacement.

Two key assumptions underlie the construction of these networks: the affine network and the phantom network. The affine network, depicted in Figure (2.5a), posits that junction points deform uniformly with macroscopic deformation, meaning that the deformation is based on the positions of the two ends of the monomers. Due to this assumption, this model is primarily suitable for small deformations. In contrast, the phantom network suggests that chains can move freely through one another because the network’s motion is determined by the displacements of the junctions, as seen in Figure (2.5b). These different assumptions result in the phantom network being consistently softer than the affine network. One specific type of network that interests researchers is the semiflexible filament network, which is prevalent in biopolymers.

First, the definition of ”affinity” should be stated. Affinity refers to the condition wherein, within a specified volume, the average displacements of crosslinks in a network are perfectly aligned with the deformation

gradient. In simpler terms, it implies that on average, every part of the material undergoes the same deformation. However, individual crosslinks within the material may still deviate or exhibit variations from this average behavior, and these deviations are referred to as fluctuations, leading to what is termed as ”non-affinity.” In cases where these fluctuations are entirely absent, the deformation is referred to as affine. It is crucial to understand that a continuum model, which encompasses all hyperelastic strain energy functions, can only describe affine deformations; it lacks the capability to predict or account for the magnitude or extent of non-affine fluctuations.

For an affine network composed of polymeric materials, a positive normal stress will only occur when stress softening also takes place. Stress softening means that the material becomes weaker or less resistant to deformation. However, it is important to note that stress softening alone does not guarantee a positive normal stress. Both stress hardening and stress softening can induce negative normal stress under certain conditions.

In the case of a non-affine system, which can be achieved by applying a random, two-dimensional arrangement of polymer network (referred to as a Mikado network), research findings indicate that it can never yield the same results as an affine system, even when the non-affine system is made infinitely stiff [27]. This emphasizes the fundamental differences and limitations associated with modeling non-affine deformations in contrast to the more straightforward descriptions provided by affine models.

$$w_{\text{chain}} = k_B T \pi^2 c(1-x^2) + \frac{k_B T}{\pi c(1-x^2)}, \quad x = \xi_c / L_c \tag{2.17}$$

Given that microstructures in these materials are crosslinked to form complicated networks, several assumptions have been put made to describe this crosslinking process, as illustrated in Figure (2.6). These assumptions include the 1-chain model, which employs spherical coordinates and positions one side of the chain at the center. Moreover, a variety of constitutive models build upon the 3-chain and 8-chain models. Table (2.4) provides an overview of micromechanical models developed over the years, where the symbol n represents the density of filaments.

One of the early 8-chain models was proposed by Arruda and Boyce, initially as an incompressible model designed for elastomers. Later, they extended this model to handle compressible materials by introducing the volumetric term J. In 2001, they once again expanded the incompressible model to accommodate compressible materials by incorporating various volumetric terms.

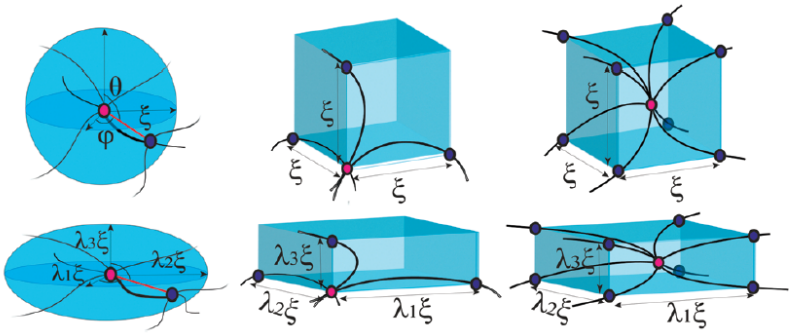

Figure 2.6: The deformation with respect to (left) 1-chain, (middle) 3-chain, and (right) 8-chain models [26]. ξ_c denotes the end-to-end length of the filament.

F. Meng et al. have proposed a continuum theory for equilibrium elasticity for a semiflexible filament network. Each individual filament within the network can be characterized by its persistent length (l_p), contour length (L_c), and the dimensionless stiffness parameter ($c = l_p/(2L_c)$). When c is much larger than the critical stiffness parameter (c^*), the filament behaves similarly to a stiff rod, while it becomes highly flexible when c is much smaller than c^*. The assumption in this model is that the network of filaments is affine, meaning that the deformation aligns with the mesh cell.

To explore the Poynting effect under these conditions, the study investigates the normal strain in a

Table 2.4: Micromechanics-based strain-energy functions.

Blundell-Terentjev (2009) [26]	1-chain	$k_BT\pi^2c(1-x^2)+\frac{k_BT}{\pi c(1-x^2)}, \quad x=\xi_c/L_c$
Xu–Safran (2015) [58]	3-chain	$\frac{1}{3}n\Sigma_{i=1}^{3}w_{\text{chain}}(\lambda_i)+\frac{1}{2}\tilde{K}(\lambda_1+\lambda_2+\lambda_3-3)^2$
Meng-Terentjev (2016) [26]	3-chain	$\frac{\mu}{3}\left(\frac{\pi^2c}{2}\left(3-x_0^2I_1\right)+\frac{2(3-2I_1x_0^2+I_2x_0^4)}{\pi c(1-I_1x_0^2+I_2x_0^4-J^2x_0^6)}\right)$
Arruda-Boyce (1993) [60]	8-chain	$\mu\sqrt{n}\left(\beta_{\text{chain}}\sqrt{\frac{I_1}{3}}+\sqrt{n}\ln\left(\frac{\beta_{\text{chain}}}{\sinh\beta_{\text{chain}}}\right)\right),$ $\beta_{\text{chain}}=L^{-1}\left(\sqrt{\frac{I_1}{3n}}\right), \quad L(\beta)=\coth(\beta)-\frac{1}{\beta}$
Arruda-Boyce (2001) [60]	8-chain	$\mu\sqrt{n}\left(\beta_{\text{chain}}\sqrt{\frac{I_1}{3}}+\sqrt{n}\ln\left(\frac{\beta_{\text{chain}}}{\sinh\beta_{\text{chain}}}\right)\right)+\frac{\kappa}{2}(J-1)^2,$ $\beta_{\text{chain}}=L^{-1}\left(\sqrt{\frac{I_1}{3n}}\right), \quad L(\beta)=\coth(\beta)-\frac{1}{\beta}$
Arruda-Boyce (2001) [60]	8-chain	$\mu\sqrt{n}\left[\beta_{\text{chain}}\sqrt{\frac{I_1}{3}}+\sqrt{n}\ln\left(\frac{\beta_{\text{chain}}}{\sinh(\beta_{\text{chain}})}\right)\frac{\beta_0}{3}ln(\frac{1}{J})\right] \quad +$ $\frac{\kappa}{\alpha^2}(\cosh[\alpha(J-1)]-1), \quad \beta_{\text{chain}}=L^{-1}\left(\sqrt{\frac{1}{n}}\right)$

cylinder-shaped sample subjected to oscillating shear deformation. Although the study does not calculate the normal stress, it does examine the conditions necessary for the negative Poynting effect to occur. The tension is defined using $x=\xi_c/L_c$, where ξ_c represents the end-to-end length of the filament. When $c<c^*$, the flexible network is mainly influenced by entropic energy, resulting in a positive Poynting effect except under high tension. On the other hand, when the mesh size is comparable to the contour length, the energy required for contraction outweighs that needed for expansion, leading to a negative Poynting effect.

This thesis will use the micromechanical model to analyze the Poynting effect because of the following advantages. First, it is based on a quantitative description of the behavior of individual polymer chains, thereby establishing a link between microscopic characteristics and macroscopic response. Second, With suitable selections of parameters ”c” and ”x,” it can depict both flexible polymeric systems, such as elastomers, and stiff polymers, such as biopolymer networks. Lastly, it has been validated against experimental data, reproducing the shear stress-shear strain behavior observed in experimental systems. These three points make it a strong candidate for quantitative modeling of the Poynting effect.

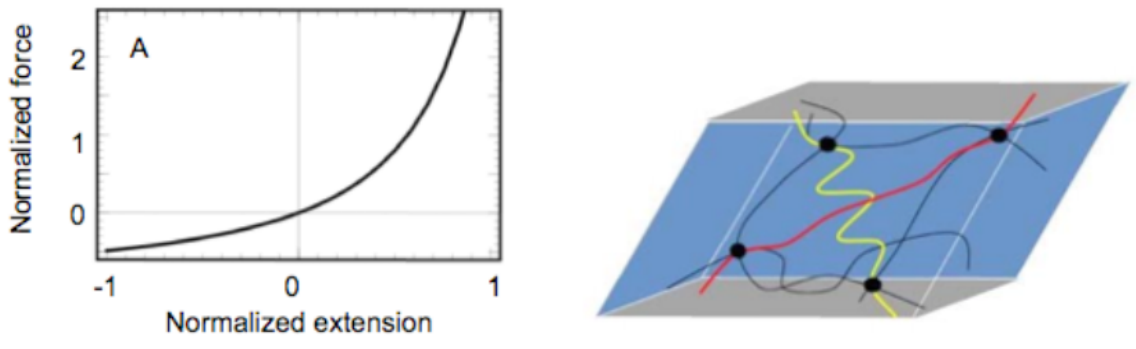

(a) (b)

Figure 2.7: (a) The force-extension curve of a rhombus isotropic filament network. (b) Illustration of the deformed network.[39]

Moreover, as previously mentioned, the asymmetric force-deformation curve also plays a crucial role in influencing the Poynting effect, as shown in Figure (2.7a). Research has indicated that compressible, isotropic, and homogeneous semiflexible networks exhibit a sharp slope upon extension and a relatively

flat slope upon compression. When a material is subjected to shearing forces under constant gap boundary conditions, as shown in Figure(2.7b), the elongation of certain filaments within the material induces greater compressive forces than the tensile forces generated by contracting filaments, leading to the emergence of a negative Poynting effect.

3

Meng's model

3.1. A revisit to Meng's model

Meng's model is a classic example of a micromechanical model grounded in network theory. This theory posits that macroscopic networks are constructed from linked filaments. The force-extension relationship for a single filament is relatively straightforward to derive and depends on two key factors: the stiffness of the filament denoted as c and its end-to-end ratio represented by x. The dimensionless stiffness parameter c quantifies the balance between bending and thermal energy and is expressed as the ratio of the persistent length of the filament, l_p, to twice its contour length, $2L_c$. The end-to-end ratio x is defined as the ratio of the end-to-end length, η, to the contour length of the filament, L_c. Filaments are categorized as semiflexible when their persistent length l_p is on a similar scale to their contour length L_c. The force-extension relationship for a single filament under these conditions can be described as follows:

$$F = k_B T \pi^2 c(1 - x^2) + \frac{k_B T}{\pi c(1 - x^2)}. \tag{3.1}$$

The next step in the modeling process involves using this relationship to derive the free energy density. This is achieved through the following steps: First, a single-chain model is developed to account for the effects of filament orientation. Denoting the orientation as (θ, ϕ), the single-chain model calculates the average orientation of a deformed filament, leading to the formulation shown in Equation (3.2).

$$F_{1c} = n \int \frac{sin\theta d\theta d\phi}{4\pi} F(\lambda\eta), \tag{3.2}$$

where n denotes the density of the filaments and λ denotes the expression $\sqrt{sin^2\theta(cos^2\phi\lambda_1^2 + sin^2\phi\lambda_2^2) + cos_\theta^2}$. Nevertheless, the single-chain model is not well-suited for modeling filament networks. Instead, researchers have introduced two alternative models: the eight-chain model and the three-chain model. The eight-chain model, developed by Palmer and Boyce [67], assumes that the deformation of each filament is identical. This assumption allows the strain energy density of the eight-chain model, denoted as F_{8c} in Equation (3.3), to be expressed as a function dependent solely on the invariant I_1.

$$F_{8c} = nF\left(\sqrt{\frac{I_1}{3}}\eta\right) \tag{3.3}$$

However, it is worth noting that the eight-chain model has limitations when it comes to analyzing the Poynting effect. Since it depends only on the invariant I_1, it cannot generate normal stress upon shearing, as argued in [26]. Therefore, an alternative three-chain model, known as Meng's model, has been developed.

Meng's model assumes that the lattice points represent the crosslinking sites and the filaments are

aligned with the principle directions of the deformation tensor. With these assumptions, the deformation of each filament i is expressed as $\lambda_i \eta$ and the strain energy density is expressed as a summation of the force-extension relation in each direction.

$$F_{3c} = \frac{n}{3} \sum_{i=3} F(\lambda_i \eta) \tag{3.4}$$

Substituting equation 3.1 into 3.4, the model is then expressed explicitly as Equation (3.5)

$$F_{3c} = \frac{n}{3} \sum_{i=3} k_B T \pi^2 c (1 - \lambda_i^2 x^2) + \frac{k_B T}{\pi c (1 - \lambda_i^2 x^2)} \tag{3.5}$$

The strain energy function is expressed in strain components. As mentioned in the previous chapter, the strain invariants formulation may lead to a simpler form. Moreover, the invariants-based function is independent of the axis of geometry, which makes it suitable for analyzing the deformation. The first part of the function in the bracket of equation (3.4) can be rewritten as

$$\begin{aligned} &\sum_{i=3} k_B T \pi^2 c (1 - \lambda_i^2 x^2) \\ =&k_B T \pi^2 c (3 - (\lambda_1^2 + \lambda_2^2 + \lambda_3^2) x^2) \\ =&k_B T \pi^2 c (3 - I_1 x^2). \end{aligned} \tag{3.6}$$

The second part of the function is formulated into:

$$\begin{aligned} &\sum_{i=3} \frac{k_B T}{\pi c (1 - \lambda_i^2 x^2)} \\ =&\frac{k_B T}{\pi c} \left(\frac{1}{1 - \lambda_1^2 x^2} + \frac{1}{1 - \lambda_2^2 x^2} + \frac{1}{1 - \lambda_3^2 x^2} \right) \\ =&\frac{k_B T}{\pi c} \left(\frac{3 - 2 I_1 x^2 + I_2 x^4}{1 - I_1 x^2 + I_2 x^4 - J^2 x^6} \right). \end{aligned} \tag{3.7}$$

After replacing $n k_B T$ as μ and substituting equation 3.6 and 3.7 into 3.5, the strain-invariant based 3-chain model is then derived.

$$F_{3c} = \frac{\mu}{3} \left(\pi^2 c (3 - I_1 x^2) + \frac{1}{\pi c} \left(\frac{3 - 2 I_1 x^2 + I_2 x^4}{1 - I_1 x^2 + I_2 x^4 - J^2 x^6} \right) \right) \tag{3.8}$$

3.2. Poynting effect analysis with Meng's model

When Meng's model was initially introduced in [26], researchers also explored its implications on the Poynting effect. The analysis process for this effect was later detailed in [29]. To begin, the research formulated the simple shear strain tensor as an incompressible tensor, as illustrated in equation (3.9). In this formulation, the shear strain is not solely reliant on γ (the applied shear strain); instead, it also relies on the deformation along the transverse direction of the shearing plane. Therefore, if λ_3 exceeds 1, it indicates a positive Poynting effect within the system. Conversely, if λ_3 is less than 1, it implies a negative Poynting effect.

$$\mathbf{F} = \begin{bmatrix} 1/\sqrt{\lambda_3} & 0 & 0 \\ 0 & 1/\sqrt{\lambda_3} & \gamma/\sqrt{\lambda_3} \\ 0 & 0 & \lambda_3 \end{bmatrix} \tag{3.9}$$

The sign of the Poynting effect is determined by the following process. First, the total free energy of the system is calculated by integrating the energy density over the radius R from 0 to R_0. Next, the derivative of the total free energy with respect to λ_3 is taken, allowing for the identification of extrema and their corresponding λ_3 values. The free energy is assumed to be a convex function, and therefore $\lambda_{3,min}$ corresponds to the point of minimum free energy, which can be interpreted as the equilibrium state for the system at a given stiffness c, end-to-end ratio x, and γ. The results are depicted in Figure

(3.1).

It is worth noting that there is a region where the filament network is characterized as unstable. The network is stable if the marginal rigidity condition $G_0 \geq 0$. G_0 represents the linear shear modulus, which can be observed in the linear regime $\sigma = G_0\gamma$ of the stress-strain diagram. The stable criterion is expressed as Equation 3.10, which will be proven in the next section when the stress-strain relation is derived.

$$c \leq \frac{1}{\pi^{3/2}} \frac{\sqrt{1+x^2}}{(1-x^2)^{3/2}}. \tag{3.10}$$

However, when attempting to repeat the same results, it became evident that the assumption equating local extrema with local minima is not universally valid for all combinations of (c, x). With the given deformation tensor (3.9), the corresponding expressions for the invariants are as follows: $I_1 = \lambda_3^2 + (2+\gamma^2)/\lambda_3$, $I_2 = 2\lambda_3 + (1+\gamma^2)/\lambda_3^2$, and $J = 1$. Upon substituting these values into equation (3.8), we arrive at the strain energy density for this tensor. The three-chain model can be reformulated as follows:

$$F_{3c} = \frac{\mu}{3}\left(\pi^2 c(3-(\lambda_3^2+\frac{2+\gamma^2}{\lambda_3})x^2) + \frac{1}{\pi c}\left(\frac{3-2(\lambda_3^2+\frac{2+\gamma^2}{\lambda_3})x^2+(2\lambda_3+\frac{1+\gamma^2}{\lambda_3^2})x^4}{1-(\lambda_3^2+\frac{2+\gamma^2}{\lambda_3})x^2+(2\lambda_3+\frac{1+\gamma^2}{\lambda_3^2})x^4-x^6}\right)\right) \tag{3.11}$$

Furthermore, we assume that the shear strain γ varies linearly with respect to the radius r. Therefore, with γ_0 representing the shear strain at the outermost surface R_0, the shear strain $\gamma(r)$ can be expressed as $\gamma(r) = \gamma_0 r/R_0$. We can then proceed to integrate the energy density with respect to the radius. To simplify the function, we express the total free energy with respect to γ_0 using the following relation:

$$\int_0^{R_0} dr F_{3c}(\lambda, r) = \int_0^{\gamma_0} \frac{R_0}{\gamma_0} d\gamma F_{3c}(\lambda, \gamma). \tag{3.12}$$

After the integration, the total free energy E is expressed as equation (3.13).

$$\begin{aligned}
E &= \frac{R_0\mu}{3\gamma_0}(e_1+e_2),\\
e_1 &= \pi^2 c\left(3-x^2\lambda_3^2-\frac{2x^2}{\lambda_3}\right)\gamma_0 - \frac{\pi^2 c x^2 \gamma_0^3}{3\lambda_3},\\
e_2 &= \frac{\gamma_0}{\pi c} + \frac{x^2\gamma_0}{\pi c\lambda_3 B} + \left(\frac{x^6+2-x^2\lambda_3^2-\frac{2x^2}{\lambda}}{\pi c\sqrt{AB}} - \frac{x^2}{\pi c\lambda_3}\sqrt{\frac{A}{B^3}}\right)\times\begin{cases} arctanh(\sqrt{\frac{B}{A}}\gamma_0), & \text{if } |\sqrt{\frac{B}{A}}\gamma_0| < 1 \\ arccoth(\sqrt{\frac{B}{A}}\gamma_0), & \text{if } |\sqrt{\frac{B}{A}}\gamma_0| > 1 \end{cases},\\
A &= 1-\lambda_3^2x^2-\frac{2x^2}{\lambda_3}+2\lambda_3x^4+\frac{x^4}{\lambda_3^2}-x^6, \qquad B = \frac{x^2}{\lambda}-\frac{x^4}{\lambda^2}.
\end{aligned} \tag{3.13}$$

We observe that the choice of parameters can lead to changes in the constitutive equation, and as a result, the total energy may not always behave as a convex function with respect to λ_3. In certain cases, the curve becomes concave, and the point where the first derivative of the function equals zero corresponds to the maximum total free energy. This behavior is illustrated in Figure (3.7), where five different parameter combinations are selected. When (c, x) is set to $(0.1, 0.1)$ and $(0.1, 0.5)$, the function is convex, and the assumption holds. However, for the datasets $(0.1, 0.8)$, $(0.5, 0.8)$, and $(0.8, 0.8)$, the curves are concave. This phenomenon is related to the conditional equation $\sqrt{\frac{B}{A}}\gamma_0$, which depends only on the end-to-end ratio x. To estimate the value of x that leads to the violation of the assumption, assuming $\lambda = 1$ and using the condition $|\sqrt{\frac{B}{A}}\gamma_0| > 1$, we find that when $x > 0.78$, the local maxima of the system become the maximum rather than the minimum. This implies that the region of the positive Poynting effect falls within the bounds of the assumption. However, for certain cases of the negative Poynting effect, it violates the assumption.

The results are not entirely satisfactory, and we aim to implement an alternative method for calculating the Poynting effect that can be applied to a broader range of datasets.

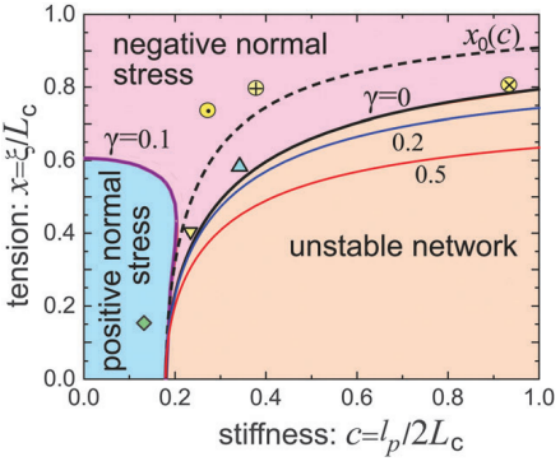

Figure 3.1: Poynting effect is analyzed in [26, 27] using the principle of minimum energy. The red part, blue part, and orange part correspond to the positive Poynting effect, the negative Poynting effect, and unstable network, respectively.

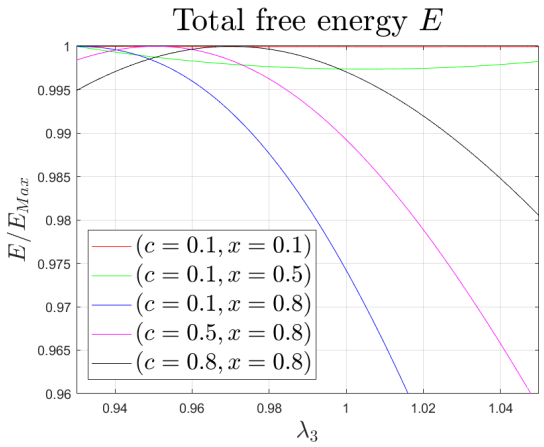

Figure 3.2: Attempt to regenerate the same results shows that the principle of minimum energy fails because, for some material parameters, where the slope equals zero corresponds to the largest total energy.

3.3. Alternative method: Stress-strain relation

With the energy density function, the stress-strain relation of the model can be derived. With the stress-strain relation, we could directly compute the resulting normal stress upon shearing, therefore determining the Poynting effect. First, an important assumption is that the undeformed materials are assumed to be isotropic to simplify the formulation. To ensure the assumption holds, it would be better to construct the left Cauchy-Green deformation tensor **B** by the relation $\mathbf{B} = \mathbf{F} \cdot \mathbf{F}^T$ since the formulation will be automatically isotropic. Also, it is worth noting that within this research, we focus on the Cauchy stress tensor □.

Two methods are available for deriving the stress-strain relation, and they both yield the same result. The first method directly utilizes the deformation gradient **F**.

$$\sigma_{ij} = \frac{1}{J} F_{ik} \frac{\partial W}{\partial F_{kj}} \tag{3.14}$$

This approach is particularly useful when dealing with simple strain-based models. However, many models are invariant-based, and it would be convenient to directly apply the model to the stress-strain

relation without the need to derive the relation each time a new function is applied. The advantage of using an invariant-based formulation will become evident when applying the volumetric strain energy function to Meng's model.

Starting from equation (3.14), we can establish the equivalence of $\partial W/\partial F_{ij}$ by utilizing the invariants I_1, I_2, and J.

$$\frac{\partial W}{\partial F_{ij}} = \frac{\partial W}{\partial I_1}\frac{\partial I_1}{\partial F_{ij}} + \frac{\partial W}{\partial I_2}\frac{\partial I_2}{\partial F_{ij}} + \frac{\partial W}{\partial J}\frac{\partial J}{\partial F_{ij}} \tag{3.15}$$

The expression of $\partial W/\partial I_1$, $\partial W/\partial I_2$, and $\partial W/\partial J$ can be easily derived with the given function.

$$\frac{\partial I_1}{\partial F_{ij}} = \frac{\partial\ \mathrm{tr}(\mathbf{B})}{\partial F_{ij}} = 2F_{ij}\frac{\partial\ \mathrm{tr}(\mathbf{F})}{\partial F_{ij}} = 2F_{ij}. \tag{3.16}$$

$$\begin{aligned}\frac{\partial I_2}{\partial F_{ij}} &= \frac{\partial\ 0.5(I_1^2 - \mathbf{B}\cdot\cdot\mathbf{B})}{\partial F_{ij}} = \frac{1}{2}2I_1\frac{\partial I_1}{\partial F_{ij}} + \frac{1}{2}4B_{ik}F_{kj} \\ &= 2I_1F_{ij} + 2B_{ik}F_{kj}.\end{aligned} \tag{3.17}$$

$$\frac{\partial J}{\partial F_{ij}} = \frac{\partial \det(\mathbf{F})}{\partial F_{ij}} = \mathrm{adj}(\mathbf{F})^T = (\det(\mathbf{F})\mathbf{F}^{-1})^T = JF_{ji}^{-1}. \tag{3.18}$$

Substituting equation (3.16), (3.17), and (3.18) into equation (3.14), we obtain the following relation.

$$\sigma_{ij} = \frac{2}{J}\left[\left(\frac{\partial W}{\partial I_1} + I_1\frac{\partial W}{\partial I_2}\right)B_{ij} - \frac{\partial W}{\partial I_2}B_{ik}B_{kj}\right] + \frac{\partial W}{\partial J}\delta_{ij} \tag{3.19}$$

Alternatively, the relation can also be derived based on different sets of invariants $\tilde{I_1}$, $\tilde{I_2}$, and J.

$$\sigma_{ij} = \frac{2}{J}\left[\frac{1}{J^{2/3}}\left(\frac{\partial \tilde{W}}{\partial \tilde{I_1}} + \tilde{I_1}\frac{\partial \tilde{W}}{\partial \tilde{I_2}}\right)B_{ij} - \left(\tilde{I_1}\frac{\partial \tilde{W}}{\partial \tilde{I_1}} + 2\tilde{I_2}\frac{\partial \tilde{W}}{\partial \tilde{I_2}}\right)\frac{\delta_{ij}}{3} - \frac{1}{J^{4/3}}\frac{\partial \tilde{W}}{\partial \tilde{I_2}}B_{ik}B_{kj}\right] + \frac{\partial \tilde{W}}{\partial J}\delta_{ij} \tag{3.20}$$

An important premise of the relations above requires that the materials show some extent of compressibility, thus requiring a compressible strain tensor with $J \neq 1$. The reason behind this phenomenon results from the fact that for perfectly incompressible materials, their shape will not be changed by applying any external pressure., which leads to a situation where the stress-strain relation is only able to show the deviatoric stress $\tilde{\sigma_{ij}} = \sigma_{ij} - \sigma_{kk}\delta_{ij}/3 = \sigma_{ij} + p\delta_{ij}$. p represents the hydrostatic pressure applied to the materials. The stress-strain relation becomes a two-invariant model and it is expressed as Equation (3.21).

$$\sigma_{ij} = 2\left[\left(\frac{\partial W}{\partial I_1} + I_1\frac{\partial W}{\partial I_2}\right)B_{ij} - \left(I_1\frac{\partial W}{\partial I_1} + 2I_2\frac{\partial W}{\partial I_2}\right)\frac{\delta_{ij}}{3} - \frac{\partial W}{\partial I_2}B_{ik}B_{kj}\right] + p\delta_{ij} \tag{3.21}$$

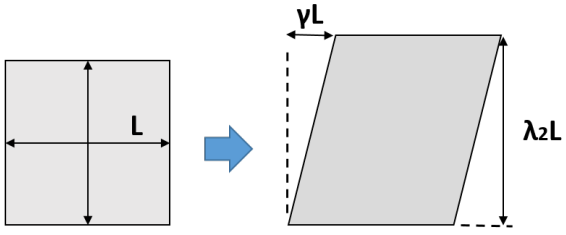

Figure 3.3: An illustration of the simple shear of a compressible cube. The compressibility is achieved by assigning a strain tensor with a determinant not equal to one.

The strain tensor used in [26] is designed for incompressible materials, which means that when applying it to the stress-strain relation, we need to apply Equation (3.21). However, since most of the biomaterials show some extent of compressibility, we want to use an alternative method to study the Poynting effect. The new strain gradient includes the compressibility is illustrated by Figure(3.3) and

is shown in equation (3.22). For the upcoming sections, instead of using the cylinder geometry as in Meng's paper, we will apply simple shear to a cube. In this alternative strain tensor, the shear strain is solely determined by γ, and only the principal strain in the transverse direction, λ_2, does not equal one. The volume change is also solely dependent on λ_2.

$$\begin{bmatrix} 1 & \gamma & 0 \\ 0 & \lambda_2 & 0 \\ 0 & 0 & 1 \end{bmatrix} \tag{3.22}$$

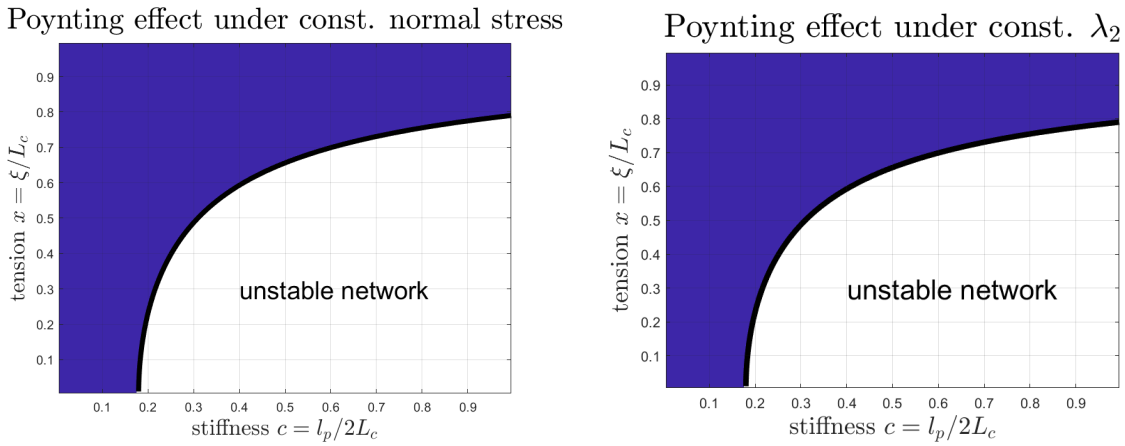

(a) (b)

Figure 3.4: Poynting effect under (a) the constant normal stress boundary conditions, where the dark blue region corresponds to negative Poynting effect; (b) the constant normal gap boundary conditions, which also results in negative Poynting effect for all stable networks. The unstable region is left blank.

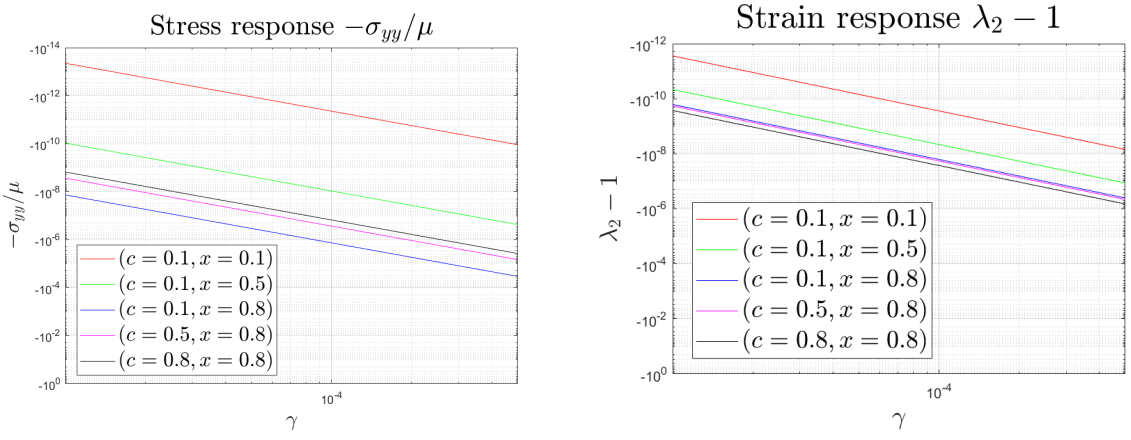

(a) (b)

Figure 3.5: (a) Adimensional stress response curves under constant height boundary conditions; (b) Strain response curves under constant normal stress boundary conditions.

The analysis of the Poynting effect involves applying shear strain γ within the range of 0 to 0.0005. In this research, we specifically focus on infinitesimal strain and its corresponding stress response. Additionally, the sign of the Poynting effect is determined based on the thrust rather than the Cauchy stress. The relationship between the thrust in the transverse direction, denoted as T, and the corresponding Cauchy stress σ_{yy} is given by $T = -\sigma_{yy}$. If the thrust is positive, then the sign of the Poynting effect is also positive, and vice versa.

Using the stress-strain relation provides the advantage of applying different boundary conditions to

study the model with ease. As mentioned earlier, the Poynting effect can be observed under two typical boundary conditions. One involves keeping the gap of the material constant, while the other involves keeping the normal stress applied to the material constant, allowing its gap to change. Figures (3.10a) and (3.10b) illustrate that the results obtained differ significantly from those obtained by Meng. Under both boundary conditions, the model exhibits a negative Poynting effect.

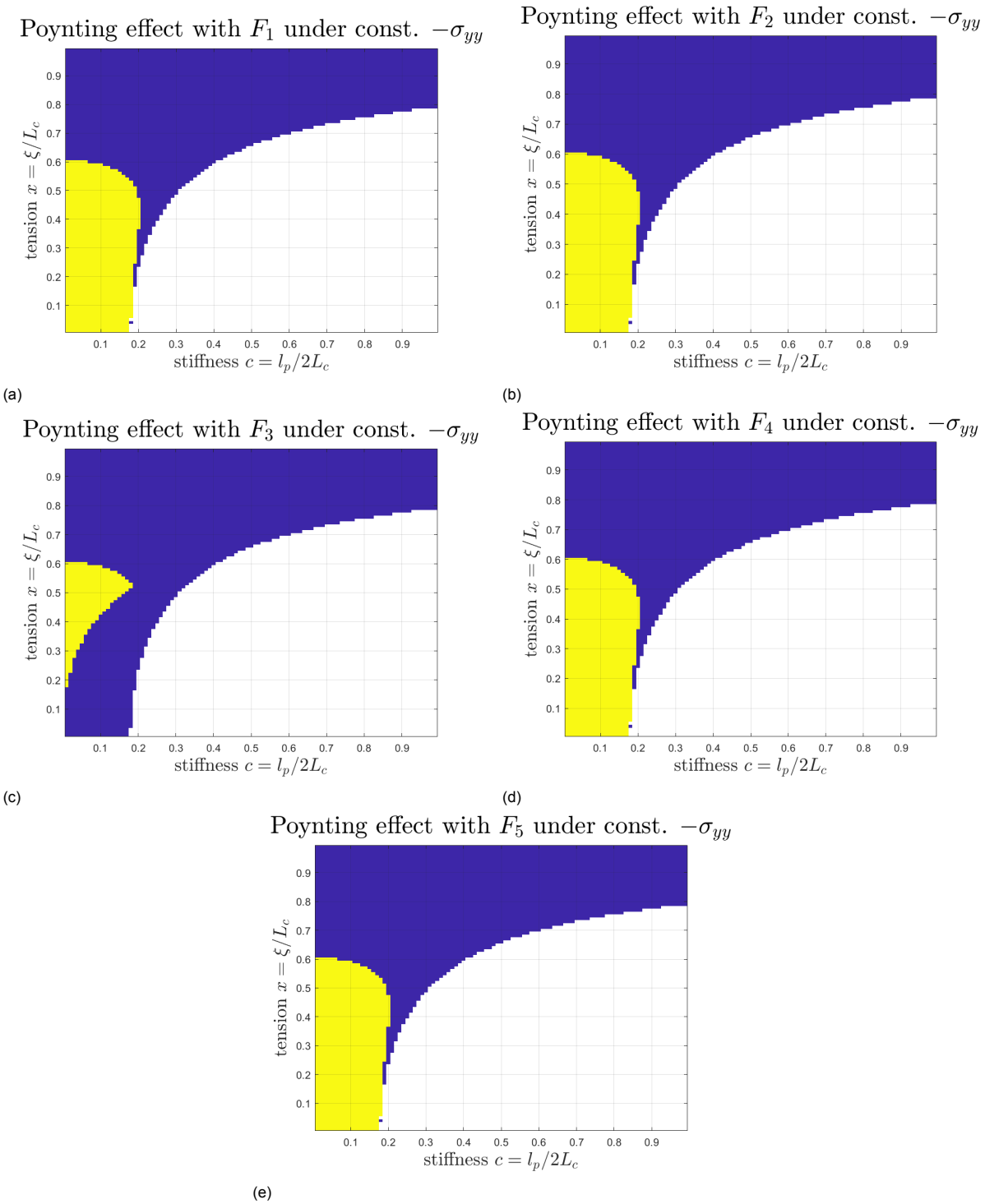

Figure 3.6: The sign of Poynting effect with the addition of volumetric energy density functions.

Moreover, we could also investigate the magnitude of the resulting stress or strain response. We choose 5 datasets to represent the results. From the figure(3.10a) and (3.10b), it could be noticed that

the dataset corresponds to the largest magnitude of the stress response, which is (c=0.1, x=0.8), is not the same with the one shows the largest strain response. This observation provides evidence that boundary conditions can indeed influence the behavior of the Poynting effect.

3.4. Addition of volumetric energy function

In this chapter, we explore the effects of adding an extra volumetric term to Meng's model in order to model an almost incompressible material. The need for this addition arises from the fact that Meng's model, in its original form, lacks dependence on the bulk modulus κ, making it unsuitable for studying the behavior of almost incompressible materials where the ratio $\mu/\kappa >> 1$ is significant.

One advantage of using invariant-based models is their flexibility in transforming into a form with separate deviatoric and volumetric components. The addition of the volumetric term follows a specific procedure. Initially, Meng's model, which is originally a function of invariants I_1, I_2, and I_3, is transformed into a form $\tilde{W}(\tilde{I_1}, \tilde{I_2}, J = 1) + F(J)$, where $\tilde{W}$ represents the isochoric part and $F(J)$ represents the volumetric part. Then, we introduce the bulk modulus κ to the model, setting its magnitude to be a hundred times larger than that of the shear modulus μ. Consequently, the bulk modulus κ is associated with the volumetric part, while the shear modulus μ is associated with the isochoric part.

Table 3.1: Volumetric part of strain-energy functions W_{vol}.

F_1	$\frac{\kappa}{2}(J-1)^2$
F_2	$\frac{\kappa}{4}(J^2-1-2\ln J)$
F_3	$\kappa\left((J_1)^2-\ln J^2\right)$
F_4	$\frac{\kappa}{2}(1-J^*)(J-2+J^*+\frac{(1-J^*)^2}{J-J^*})$
F_5	$\frac{\kappa}{2}\ln J^2$

The selected volumetric strain energy functions are presented in table (3.1). The outcomes are depicted in figure (3.6). The range of shear strain γ applied to the models remains the same as before. The first energy function, F_1, is chosen because it is a commonly used formulation in previous research, such as [33]. The second function, F_2, is a relatively new function proposed by Anssari-Benam and Horgan in 2022 [55]. This function is characterized by two factors: it approaches infinity when the volume ratio approaches either infinity or zero, and it is widely used in finite element analysis. The fifth function, F_5, was first proposed by Valanis-Landel in 1967 and is known for its simplicity. It is a phenomenological function inspired by natural rubbers. The third function, F_3, is a general form that combines aspects of functions F_1 and F_5, overcoming instability issues encountered with F_1 and F_5. Finally, the function F_4, introduced by A. E. Ehret in 2017, is designed to describe the mechanisms of poroelastic soft matter. J^* represents the limit of volume reduction due to growing resistance to compression.

The analysis of the Poynting effect is conducted solely under constant normal stress boundary conditions. The case where the gap is held constant is not separately investigated for each model because, in this case, the determinant of the strain tensor becomes $J = 1$, rendering the volumetric strain energy function irrelevant. From the results shown above, it is evident that introducing the volumetric part to Meng's model alters the Poynting effect. For example, the most noticeable change is the appearance of a light yellow region, corresponding to a positive Poynting effect.

More specifically, models 1, 2, 4, and 5 exhibit similar stress responses, indicating that these models express comparable stress responses under small shear strain. This similarity is further demonstrated in the next subsection. It is also worth noting that the sign of the Poynting effect is very much in line with the one obtained from Meng's original analysis. The difference is that, by employing the stress-strain relation, the result is more straightforward and convincing.

These results also suggest that the semiflexible filament network, which represents many biomate-

rials, can be effectively modeled using compressible or almost incompressible assumptions. However, it would be advantageous to have a method for predicting the sign of the Poynting effect without directly applying shear strain and investigating the resulting response. Therefore, a useful method will be developed in the following subsections.

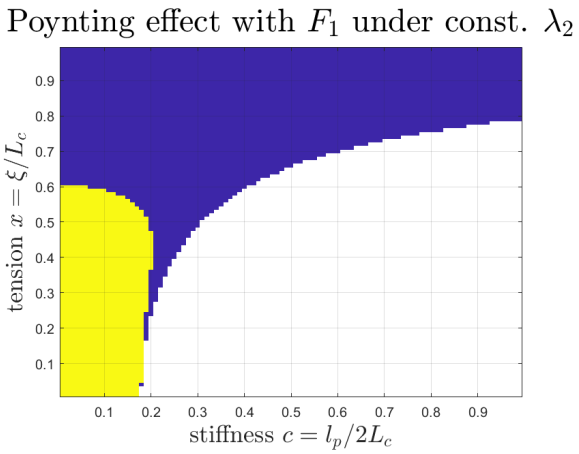

Figure 3.7: The sign of Poynting effect under constant height B.C. with volumetric function F_1 shows identical distribution as Figure(3.6.a).

3.5. Taylor's expansion

Based on the previous study, we can assume that the stress or strain response is monotonic for small but finite shear strains, which is also the range of shear strains that we are interested in. Therefore, it is reasonable to apply a Taylor expansion to simplify the stress-strain relation for further analysis. The original stress-strain relation using strain tensor (3.22) is expressed in equation (3.23). This equation is relatively complex, as it involves both γ and λ_2 in both the denominator and numerator.

$$-\sigma_{yy} = 2x\mu\frac{1-2x^2(\gamma^2+(-1+\lambda_2)^2)-\lambda_2-2x^6(-1+\lambda_2)\lambda_2(2+\gamma^2+\lambda_2+\lambda_2^2)+x^8\lambda_2(-1-\gamma^2+\lambda_2^3)+}{3c\pi(-1+x^2)^2(1+x^4\lambda_2^2-x^2(1+\gamma^2+\lambda_2^2))^2}$$
$$+\frac{c^2\pi^3(-1+x^2)^2(-1+\lambda_2)(1+x^4\lambda_2^2-x^2(1+\gamma^2+\lambda_2^2))^2+x^4(1+\gamma^4-6\lambda_2+4\lambda_2^2+\lambda_2^4+\gamma^2(2-\lambda_2+2\lambda_2^2))}{3c\pi(-1+x^2)^2(1+x^4\lambda_2^2-x^2(1+\gamma^2+\lambda_2^2))^2} \tag{3.23}$$

Then, the Taylor expansion is applied to the model. It is expanded at the initial conditions, which we assume an undeformed geometry to be $\gamma = 0$ and $\lambda_2 = 1$.

$$\begin{aligned}-\sigma_{yy} &= \frac{2x^2(1-c^2\pi^3+3x^2+3c^2\pi^3x^2-3c^2\pi^3x^4+c^2\pi^3x^6)\mu}{3c\pi(-1+x^2)^3}(-1+\lambda_2)\\ &-\gamma^2\left(\frac{2x^4(2+x^2)\mu}{3c\pi(-1+x^2)^4}-\frac{2x^4(2+11x^2+3x^4)\mu}{3c\pi(-1+x^2)^5}(-1+\lambda_2)\right)\end{aligned} \tag{3.24}$$

After the expansion, the stress-strain relation can be categorized into three parts, dependent on (λ_2-1), γ^2, and $(\lambda_2-1)\gamma^2$, respectively. Given our focus on relatively small scales, we argue that the third term can be safely ignored. This is because, from the numerical study in the previous section, it was found that the absolute value of (λ_2-1) typically falls on the order of magnitude of 10^{-6}, making the third term too small to have a noticeable impact.

Moving on to models with volumetric parts, as the volumetric part is added to the model linearly, the corresponding stress response of the volumetric function can also be seen as a linear addition. Therefore, we apply Taylor expansion to the functions used in the previous subsection. It becomes evident that for functions F_1, F_2, F_3, and F_5, the expressions after expansion are the same. This reaffirms the results obtained in the previous subsection and confirms that these models exhibit the same behavior at small strains.

Table 3.2: Volumetric part of strain-energy functions and their Taylor expansion forms.

	Original function	Taylor expansion
F_1	$\frac{\kappa}{2}(J-1)^2$	$\kappa(-1+\lambda_2)$
F_2	$\frac{\kappa}{4}(J^2-1-2\ln J)$	$\kappa(-1+\lambda_2)$
F_3	$\kappa\left((J-1)^2-\ln J^2\right)$	0
F_4	$\frac{\kappa}{2}(1-J^*)(J-2+J^*+\frac{(1-J^*)^2}{J-J^*})$	$\kappa(-1+\lambda_2)$
F_5	$\frac{\kappa}{2}\ln J^2$	$\kappa(-1+\lambda_2)$

Due to the same expression, we will select F_1 as a representative to compute the Taylor expansion. The original stress-strain relation is given by Equation (3.25).

$$\begin{aligned}-\sigma_{yy} = -(-1+\lambda_2)\kappa &- \frac{(4x^4\lambda_2^{4/3}(1+\gamma^2-\lambda_2^2)(4\lambda_2^{4/3}+2x^6\lambda_2^{4/3}-2x^2\lambda_2^{2/3}(2+\gamma^2+\lambda_2^2))\mu)}{(18c\pi(x^2-\lambda_2^{2/3})^2\lambda_2^{7/3}(\lambda_2^{2/3}+x^4\lambda_2^{4/3}-x^2(1+\gamma^2+\lambda_2^2))^2)} \\ &- \frac{-x^2\lambda_2^{2/3}(2+\gamma^2-2\lambda_2^2)(4\lambda_2^{8/3}+8x^6\lambda_2^{8/3}-4x^4\lambda_2^{4/3}(1+\gamma^2+2\lambda_2^2))\mu}{(18c\pi(x^2-\lambda_2^{2/3})^2\lambda_2^{7/3}(\lambda_2^{2/3}+x^4\lambda_2^{4/3}-x^2(1+\gamma^2+\lambda_2^2))^2)} \\ &- \frac{-x^2\lambda_2^{2/3}(2+\gamma^2-2\lambda_2^2)(-4c^2\pi^3(x^2-\lambda_2^{2/3})^2(\lambda_2^{2/3}+x^4\lambda_2^{4/3}-x^2(1+\gamma^2+\lambda_2^2))^2)\mu}{(18c\pi(x^2-\lambda_2^{2/3})^2\lambda_2^{7/3}(\lambda_2^{2/3}+x^4\lambda_2^{4/3}-x^2(1+\gamma^2+\lambda_2^2))^2)}\end{aligned} \tag{3.25}$$

The Taylor expansion is applied to the model as the process used above. This time, only two terms, γ^2 and λ_2, are shown.

$$\begin{aligned}-\sigma_{yy} = -(-1+\lambda_2)&\left(\kappa - \frac{8(x^2\mu - c^2\pi^3x^2\mu + x^4\mu + 3c^2\pi^3x^4\mu - 3c^2\pi^3x^6\mu + c^2\pi^3x^8\mu)}{9c\pi(-1+x^2)^3}\right) \\ &- \gamma^2\left(\frac{2(-x^2\mu + c^2\pi^3x^2\mu + 2x^4\mu - 4c^2\pi^3x^4\mu + 2x^6\mu + 6c^2\pi^3x^6\mu - 4c^2\pi^3x^8\mu + c^2\pi^3x^{10}\mu)}{9c\pi(-1+x^2)^4}\right)\end{aligned} \tag{3.26}$$

We could also apply it to the shear stress response. The original equation is given as (3.27).

$$\sigma_{xy} = -\frac{((2x^2\gamma(-\lambda_2^{4/3}+x^4\lambda_2^2+c^2\pi^3(\lambda_2^{2/3}+x^4\lambda_2^{4/3}-x^2(1+\gamma^2+\lambda_2^2))^2)\mu)}{(3c\pi\lambda_2^{2/3}(\lambda_2^{2/3}+x^4\lambda_2^{4/3}-x^2(1+\gamma^2+\lambda_2^2))^2))}. \tag{3.27}$$

The Taylor expansion form would be:

$$\begin{aligned}\sigma_{xy} = &-\gamma\frac{2x^2(-1+x^4+c^2\pi^3(1-2x^2+x^4)^2)\mu}{3c\pi(1-2x^2+x^4)^2} \\ &+\gamma(-1+\lambda_2)\frac{4x^2(-1+c^2\pi^3+2x^2-4c^2\pi^3x^2+2x^4+6c^2\pi^3x^4-4c^2\pi^3x^6+c^2\pi^3x^8)\mu}{9c\pi(-1+x^2)^4} \\ &+\gamma^3\left(-\frac{4x^4(1+x^2)\mu}{3c\pi(-1+x^2)^5}+\frac{8x^4(-2+3x^2+4x^4)(-1+\lambda_2)\mu}{9c\pi(-1+x^2)^6}\right).\end{aligned} \tag{3.28}$$

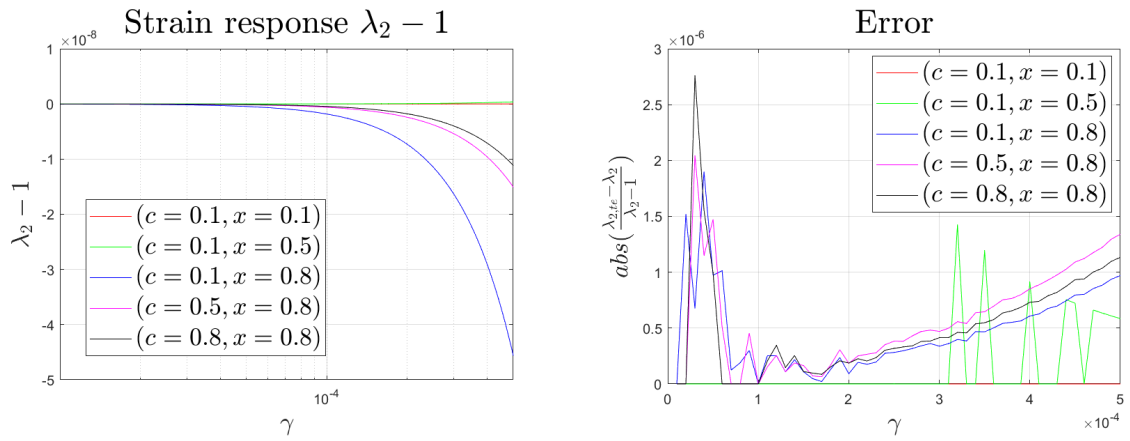

(a) (b)

Figure 3.8: Strain responses of Meng's model with the volumetric part under constant normal stress B.C. is shown in (a). The error plot (b) between the original form and the Taylor expansion form of the model shows a good approximation is reached, with error typically ranging around 10^{-14}.

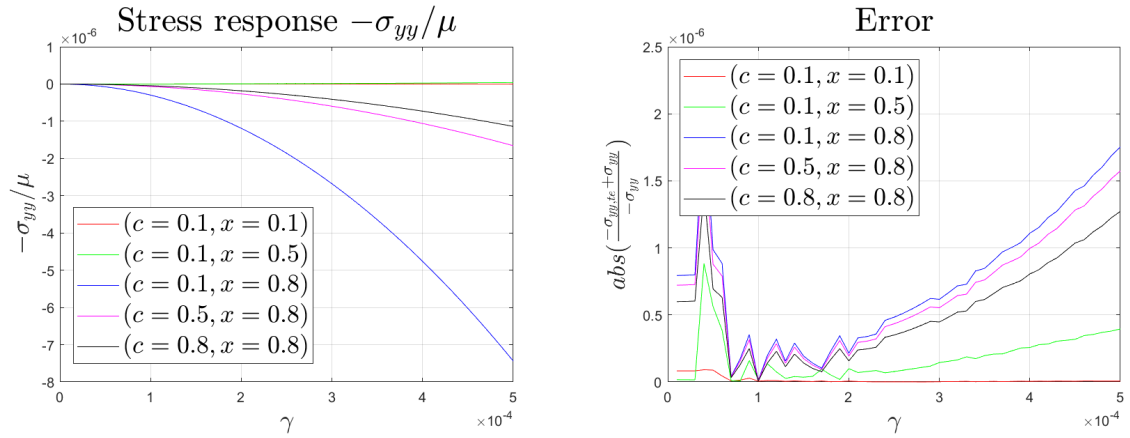

(a) (b)

Figure 3.9: Stress responses of Meng's model with the volumetric part under constant height B.C. is shown in (a). The error plot (b) between the original form and the Taylor expansion form of the model shows a larger error because the response is solely determined by γ^2 term. However, the error is still acceptable, which is around 10^{-6}.

We selected five datasets to examine the similarity between the original model and the Taylor-expanded one. The findings indicate that, under constant normal stress boundary conditions, the Taylor expansion serves as a strong approximation to the original models. It effectively conveys the Poynting effect's sign for each dataset and closely matches the magnitude of the strain response in both cases, with errors typically on the order of 10^{-14}.

The stress response, while correctly reflecting the Poynting effect using the Taylor expansion, exhibits a slightly larger magnitude difference compared to the constant normal stress boundary conditions, although it remains within acceptable bounds, with errors around the order of 10^{-6}. Overall, the Taylor expansion proves to be a robust representation of the original model at small, yet non-negligible strains.

After applying the Taylor expansion, the expressions become simplified and offer enhanced potential for further analysis. For a given dataset represented as (c, x) and material properties (μ, κ), Equation (3.26) becomes linearly dependent on λ_2 and quadratically dependent on γ. This allows for the assignment of two parameters: the first parameter, λ_L, is dependent on λ_2, while the second parameter, known as the Poynting parameter or χ, is dependent on γ^2, as defined in Equation (3.29).

When applying a constant gap boundary condition, the stress response relies solely on γ, and thus the sign of the Poynting effect is determined by χ. Notably, χ is doubled when subtracted from the stress-strain relation, as there is an additional factor of 2 introduced during the derivation of χ. This accounts for why the Poynting parameter χ is doubled when subtracted from the second term of the stress-strain relation.

On the other hand, with a constant normal stress boundary condition, the Poynting effect is influenced by both parameters, as elaborated in the next section. Equation (3.30) provides the explicit expressions for χ and λ_L, considering Meng's model with an additional volumetric component. Furthermore, in equation (3.29), we can examine the definition of the parameter related to the Taylor expansion of the shear stress response (3.28). The coefficients for the γ, $\gamma\lambda_2$, and γ^3 terms in equation (3.28) are denoted as Λ_0, Λ_1, and Λ_3.

$$\chi = -\left(\frac{\partial^2\sigma_{yy}}{\partial\gamma^2}\right)_{\gamma=0,\lambda_2=1}, \qquad \lambda_L = -\left(\frac{\partial\sigma_{yy}}{\partial\lambda_2}\right)_{\gamma=0,\lambda_2=1}$$
$$\Lambda_0 = \left(\frac{\partial\sigma_{xy}}{\partial\gamma}\right)_{\gamma=0,\lambda_2=1}, \qquad \Lambda_1 = \left(\frac{\partial}{\partial\lambda_2}\left(\frac{\partial\sigma_{xy}}{\partial\gamma}\right)\right)_{\gamma=0,\lambda_2=1}, \qquad \Lambda_3 = \frac{1}{6}\left(\frac{\partial^3\sigma_{xy}}{\partial\gamma^3}\right)_{\gamma=0,\lambda_2=1}. \tag{3.29}$$

$$\lambda_L = -\left(\kappa - \frac{8(x^2\mu - c^2\pi^3x^2\mu + x^4\mu + 3c^2\pi^3x^4\mu - 3c^2\pi^3x^6\mu + c^2\pi^3x^8\mu)}{9c\pi(-1+x^2)^3}\right),$$
$$\chi = -4\frac{-x^2\mu + c^2\pi^3x^2\mu + 2x^4\mu - 4c^2\pi^3x^4\mu + 2x^6\mu + 6c^2\pi^3x^6\mu - 4c^2\pi^3x^8\mu + c^2\pi^3x^{10}\mu}{9c\pi(-1+x^2)^4}. \tag{3.30}$$

3.6. Predict the sign - Maxwell's relation

In this section, we will explore a method for predicting the direction of the Poynting effect without the need for shear analysis or calculating the precise model response. This concept holds particular appeal because, in such cases, the Poynting effect's sign can be determined solely by the material parameters. One key assumption underlying this approach is that the Poynting effect retains its sign for small, yet finite strains.

To begin, we will introduce an arbitrary energy function denoted as W, making the derived general relationships applicable to any hyperelastic system. Subsequently, we will apply these relationships to Meng's model to investigate how they predict the direction of the Poynting effect within this specific model.

Our proposed method draws inspiration from Maxwell's relations, which are a set of equations grounded in the principles of multivariable calculus and the invariance of second derivatives. The fundamental symmetry of second derivatives dictates that for a function expressed as $f(x_i, x_j)$, the order of differentiation can be exchanged, provided that the function possesses differentiable partial derivatives. Additionally, it is crucial that x_i and x_j remain independent for the relation to hold true.

$$\left(\frac{\partial}{\partial x_j}\left(\frac{\partial f}{\partial x_i}\right)_{x_j}\right)_{x_i} = \left(\frac{\partial}{\partial x_i}\left(\frac{\partial f}{\partial x_j}\right)_{x_i}\right)_{x_j}. \tag{3.31}$$

Building upon the previous subsections, we have established that the energy density function, denoted as W, depends solely on two variables: γ and λ_2, given the material parameters. These two variables, γ and λ_2, are assumed to be independent, thereby ensuring the validity of the symmetry of second derivatives.

To derive Maxwell's relations for the Poynting effect, instead of relying on a specific function, it proves more effective to work with an arbitrary function that yields an expression applicable to all homogeneous hyperelastic models in a general sense. Therefore, we designate a representative energy function as $W(\gamma, \lambda_2)$.

Based on this assumption, the differential change in W, dW can be expressed through the relation described in equation (3.32). Here, S represents the second Piola-Kirchhoff stress tensor, while dE represents an infinitesimal alteration in the Lagrange strain tensor. The Lagrange strain tensor is defined as presented in equation (3.33), and the strain gradient remains consistent with the formulation provided in equation (3.22).

$$dW = \mathrm{Tr}(\mathbf{S} \cdot d\mathbf{E}). \tag{3.32}$$

$$\begin{aligned} \mathbf{E} &= \frac{1}{2}(\mathbf{F}^T\mathbf{F} - \mathbf{I}) \\ &= \frac{1}{2}\begin{bmatrix} 0 & \gamma & 0 \\ \gamma & -1+\gamma^2+\lambda_2^2 & 0 \\ 0 & 0 & 0 \end{bmatrix}. \end{aligned} \tag{3.33}$$

Then, the total derivative is applied to compute $d\mathbf{E}$.

$$\begin{aligned} d\mathbf{E} &= \left(\frac{\partial \mathbf{E}}{\partial \lambda_2}\right)_\gamma d\lambda_2 + \left(\frac{\partial \mathbf{E}}{\partial \gamma}\right)_{\lambda_2} d\gamma, \\ \text{where} \qquad \left(\frac{\partial \mathbf{E}}{\partial \lambda_2}\right)_\gamma &= \begin{bmatrix} 0 & 0 & 0 \\ 0 & \lambda_2 & 0 \\ 0 & 0 & 0 \end{bmatrix}, \\ \left(\frac{\partial \mathbf{E}}{\partial \gamma}\right)_{\lambda_2} &= \begin{bmatrix} 0 & 1/2 & 0 \\ 1/2 & \gamma & 0 \\ 0 & 0 & 0 \end{bmatrix} \end{aligned} \tag{3.34}$$

The Cauchy stress tensor $\boldsymbol{\sigma}$ is assumed to be nonzero only on the diagonal elements and σ_{xy}, σ_{yx}.

$$\boldsymbol{\sigma} = \begin{bmatrix} \sigma_{xx} & \sigma_{xy} & 0 \\ \sigma_{yx} & \sigma_{yy} & 0 \\ 0 & 0 & \sigma_{zz} \end{bmatrix}. \tag{3.35}$$

Equation (3.32) shows that a second Piola-Kirchoff stress tensor is required to compute dW. However, we do not directly assign an arbitrary **S** because it is more favorable for us to take a step further to express the second Piola-Kirchoff stress tensor by the Cauchy stress tensor. If we further utilize the fact that $\sigma_{xy} = \sigma_{yx}$, then

$$\begin{aligned} \mathbf{S} &= J\mathbf{F}^{-1}\boldsymbol{\sigma}\mathbf{F}^{-T} \\ &= \begin{bmatrix} \lambda_2\sigma_{xx} - 2\gamma\sigma_{xy} + \frac{\gamma^2}{\lambda_2}\sigma_{yy} & \sigma_{xy} - \frac{\gamma}{\lambda_2}\sigma_{yy} & 0 \\ \sigma_{xy} - \frac{\gamma}{\lambda_2}\sigma_{yy} & \frac{1}{\lambda_2}\sigma_{yy} & 0 \\ 0 & 0 & \lambda_2\sigma_{zz} \end{bmatrix}. \end{aligned} \tag{3.36}$$

Finally, dW is obtained.

$$dW = \sigma_{xy}d\gamma + \sigma_{yy}d\lambda_2. \tag{3.37}$$

Then, we apply the symmetry of second derivatives on dW. It shows that after the second derivative, the expression is still dependent on the shear strain γ. In order to cancel it,

$$\begin{aligned} \left(\frac{\partial}{\partial \gamma}\left(\frac{\partial W}{\partial \lambda_2}\right)_\gamma\right)_{\lambda_2} &= \left(\frac{\partial}{\partial \lambda_2}\left(\frac{\partial W}{\partial \gamma}\right)_{\lambda_2}\right)_\gamma, \\ \Rightarrow \qquad \left(\frac{\partial \sigma_{yy}}{\partial \gamma}\right)_{\lambda_2} &= \left(\frac{\partial \sigma_{xy}}{\partial \lambda_2}\right)_\gamma. \end{aligned} \tag{3.38}$$

The expression already showed a good preliminary result. However, it does not fulfill our goal to predict the Poynting effect by the material parameters, as we defined in equation (3.29).

All these parameters can only be determined under the initial conditions. If we apply the initial conditions, both sides of Equation (3.38) will yield zero. Consequently, to derive an expression involving the

parameters defined in Equation (3.29), we need to take an additional step. After applying the rule of symmetry of second derivatives, we proceed by taking the derivative of the equation with respect to γ and imposing the initial conditions. The result is presented in Equation (3.39). This relationship clearly indicates that the coefficient χ is solely reliant on the shear modulus μ, as the shear stress σ_{xy} remains independent of the bulk modulus.

$$\begin{aligned} &\frac{\partial}{\partial\gamma}\left(\left(\frac{\partial\sigma_{yy}}{\partial\gamma}\right)_{\lambda_2} = \left(\frac{\partial\sigma_{xy}}{\partial\lambda_2}\right)_{\gamma}\right)_{\gamma=0,\lambda_2=1}, \\ &\Rightarrow -\chi = \Lambda_1. \end{aligned} \tag{3.39}$$

Once a satisfactory result is achieved, it is essential to validate the findings through a parameter study. Initially, we visualize the signs of χ and λ_L is determined by Equation (3.30) in Figures (3.10a) and (3.10b). A direct comparison with Figure (3.6) reaffirms that under the constant gap boundary condition, χ is the decisive parameter dictating the direction of the Poynting effect. Subsequently, we subtract Λ_1 from Equation (3.28), and it becomes evident that the two expressions match precisely when multiplied by -1.

$$\Lambda_1 = \frac{4x^2(-1+c^2\pi^3+2x^2-4c^2\pi^3x^2+2x^4+6c^2\pi^3x^4-4c^2\pi^3x^6+c^2\pi^3x^8)\mu}{9c\pi(-1+x^2)^4}. \tag{3.40}$$

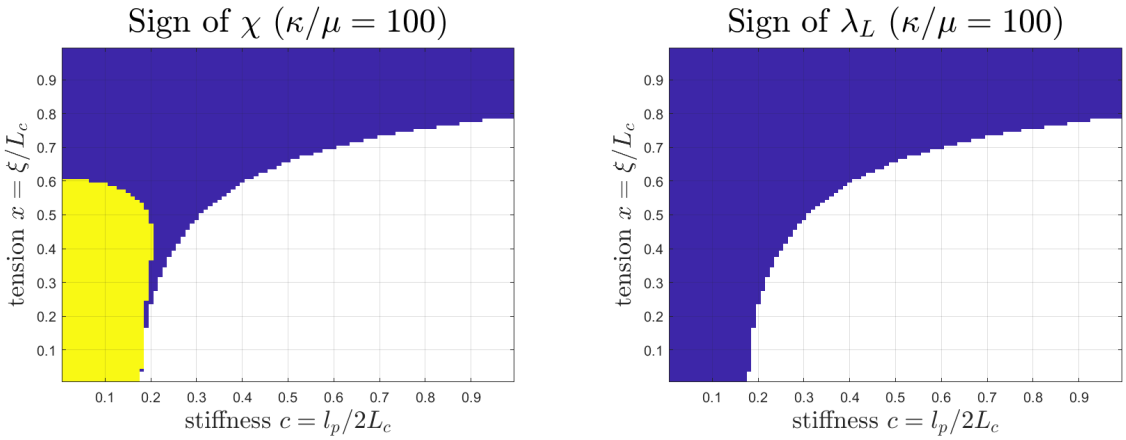

(a) (b)

Figure 3.10: Prediction of the sign of Poynting effect using (a) χ and (b) λ_L, where the yellow region represents positive value, and the dark blue region represents negative value. Under constant height B.C., the sign of the Poynting effect is determined solely by χ. However, under constant normal stress B.C., it is determined by both χ and λ_L.

3.7. Strain stiffening and boundary condition

The Poynting effect exhibits a strong connection to the strain-stiffening phenomenon. In this section, we aim to establish a relationship between these two effects and explore the role played by boundary conditions.

We argue that the γ^3 term in Equation (3.28) serves as the most representative parameter for the strain-stiffening effect. In the previous section, we have already established that under constant gap boundary conditions, the parameter governing the γ^3 term can be described as Λ_2. However, under constant normal stress boundary conditions, we cannot simply take derivatives with respect to γ. To derive $(\partial^3\sigma_{xy}/\partial\gamma^3)_{\sigma yy}$, we follow the following process.

We begin by calculating the first derivative with respect to γ. Since the normal stress σ_{yy} is also a function of (γ, λ_2), we express the shear stress response in the following form of refeqn:rewrite shear stress).

$$\sigma_{xy} = \sigma_{xy}(\gamma, \lambda_2(\gamma, \sigma_{yy}). \tag{3.41}$$

Again, by applying the rule of total derivation, the expression of $d\sigma_{xy}$ could be found.

$$\begin{aligned} d\sigma_{xy} &= \left(\frac{\partial \sigma_{xy}}{\partial \gamma}\right)_{\lambda_2} d\gamma + \left(\frac{\partial \sigma_{xy}}{\partial \lambda_2}\right)_{\gamma} d\lambda_2, \\ &= \left(\frac{\partial \sigma_{xy}}{\partial \gamma}\right)_{\lambda_2} d\gamma + \left(\frac{\partial \sigma_{xy}}{\partial \lambda_2}\right)_{\gamma} \left(\left(\frac{\partial \lambda_2}{\partial \gamma}\right)_{\sigma_{yy}} d\gamma + \left(\frac{\partial \lambda_2}{\partial \sigma_{yy}}\right)_{\gamma} d\sigma_{yy}\right). \end{aligned} \tag{3.42}$$

Since the normal stress σ_{yy} is constant, therefore $d\sigma_{yy} = 0$. The first derivative could be written as:

$$\begin{aligned} \left(\frac{\partial \sigma_{xy}}{\partial \gamma}\right)_{\sigma_{yy}} &= \left(\frac{\partial}{\partial \gamma}\left(\left(\frac{\partial \sigma_{xy}}{\partial \gamma}\right)_{\lambda_2} d\gamma + \left(\frac{\partial \sigma_{xy}}{\partial \lambda_2}\right)_{\gamma}\left(\frac{\partial \lambda_2}{\partial \gamma}\right)_{\sigma_{yy}} d\gamma\right)\right)_{\sigma_{yy}}, \\ &= \left(\frac{\partial \sigma_{xy}}{\partial \gamma}\right)_{\lambda_2} + \left(\frac{\partial \sigma_{xy}}{\partial \lambda_2}\right)_{\gamma}\left(\frac{\partial \lambda_2}{\partial \gamma}\right)_{\sigma_{yy}}. \end{aligned} \tag{3.43}$$

The expression seems simple. However, there is still a term that holds normal stress constant. For the simplicity of further calculation, we would like the normal stress to be in the bracket of derivative. Therefore, using -1 rule, we could transform the equation into the following form:

$$\left(\frac{\partial \lambda_2}{\partial \gamma}\right)_{\sigma_{yy}}\left(\frac{\partial \gamma}{\partial \sigma_{yy}}\right)_{\lambda_2}\left(\frac{\partial \sigma_{yy}}{\partial \lambda_2}\right)_{\gamma} = -1. \tag{3.44}$$

$$\left(\frac{\partial \sigma_{xy}}{\partial \gamma}\right)_{\sigma_{yy}} = \left(\frac{\partial \sigma_{xy}}{\partial \gamma}\right)_{\lambda_2} - \left(\frac{\partial \sigma_{xy}}{\partial \lambda_2}\right)_{\gamma}\left(\frac{\partial \sigma_{yy}}{\partial \gamma}\right)_{\lambda_2}\left(\frac{\partial \lambda_2}{\partial \sigma_{yy}}\right)_{\gamma} \tag{3.45}$$

Using the same procedure, the second and the third derivative could also be derived.

$$\begin{aligned} &\left(\frac{\partial^2 \sigma_{xy}}{\partial \gamma^2}\right)_{\sigma_{yy}} \\ &= \frac{\partial}{\partial \gamma}\left(\left(\frac{\partial \sigma_{xy}}{\partial \gamma}\right)_{\lambda_2} - \left(\frac{\partial \sigma_{xy}}{\partial \lambda_2}\right)_{\gamma}\left(\frac{\partial \sigma_{yy}}{\partial \gamma}\right)_{\lambda_2}\left(\frac{\partial \lambda_2}{\partial \sigma_{yy}}\right)_{\gamma}\right)_{\sigma_{yy}} \\ &= \left(\frac{\partial^2 \sigma_{xy}}{\partial \gamma^2}\right)_{\lambda_2} - 2\frac{\partial}{\partial \lambda_2}\left(\left(\frac{\partial \sigma_{xy}}{\partial \gamma}\right)_{\lambda_2}\right)_{\gamma}\left(\frac{\partial \sigma_{yy}}{\partial \gamma}\right)_{\lambda_2}\left(\frac{\partial \lambda_2}{\partial \sigma_{yy}}\right)_{\gamma} - \left(\frac{\partial \sigma_{xy}}{\partial \lambda_2}\right)_{\gamma}\left(\frac{\partial^2 \sigma_{yy}}{\partial \gamma^2}\right)_{\lambda_2}\left(\frac{\partial \lambda_2}{\partial \sigma_{yy}}\right)_{\gamma} \\ &\quad - \left(\frac{\partial \sigma_{xy}}{\partial \lambda_2}\right)_{\gamma}\left(\frac{\partial \sigma_{yy}}{\partial \gamma}\right)_{\lambda_2}\left(\frac{\partial}{\partial \gamma}\left(\frac{\partial \lambda_2}{\partial \sigma_{yy}}\right)_{\gamma}\right)_{\lambda_2} + \left(\frac{\partial^2 \sigma_{xy}}{\partial \lambda_2^2}\right)_{\gamma}\left(\frac{\partial \sigma_{yy}}{\partial \gamma}\right)_{\lambda_2}^2\left(\frac{\partial \lambda_2}{\partial \sigma_{yy}}\right)_{\gamma}^2 \\ &\quad + \left(\frac{\partial \sigma_{xy}}{\partial \lambda_2}\right)_{\gamma}\left(\frac{\partial \sigma_{yy}}{\partial \gamma}\right)_{\lambda_2}^2 \frac{\partial}{\partial \lambda_2}\left(\left(\frac{\partial \lambda_2}{\partial \sigma_{yy}}\right)_{\gamma}\right)_{\gamma}\left(\frac{\partial \lambda_2}{\partial \sigma_{yy}}\right)_{\gamma} + \left(\frac{\partial \sigma_{xy}}{\partial \lambda_2}\right)_{\gamma}\left(\frac{\partial \sigma_{yy}}{\partial \gamma}\right)_{\lambda_2}\left(\frac{\partial \lambda_2}{\partial \sigma_{yy}}\right)_{\gamma}^2\left(\frac{\partial}{\partial \lambda_2}\left(\frac{\partial \sigma_{yy}}{\partial \gamma}\right)_{\lambda_2}\right)_{\gamma} \end{aligned} \tag{3.46}$$

Our primary interest lies in anticipating the difference in the strain-stiffening effect resulting from distinct boundary conditions. One approach to achieve this is by looking at Equation (3.47), which characterizes the constant normal stress boundary condition, with $(\partial^3 \sigma_{xy}/\partial \gamma^3)_{\lambda_2}$, representing the third derivative of shear stress response under constant gap boundary conditions.

To obtain the difference between these two expressions, we note that from Equation (3.47), it is evident that $(\partial^3 \sigma_{xy}/\partial \gamma^3)_{\lambda_2}$ corresponds exactly to the first term of the equation. Therefore, the remaining components of the equation represent the distinction introduced by the two different boundary conditions. However, the resulting expression is rather intricate and not suitable for straightforward analysis. Therefore, similar to our approach in the previous section, we apply the initial conditions to the expression, resulting in a simplified expression composed of the parameters defined in Equation (3.30).

Through the formulation in Equation (3.26) and (3.28), we derive additional initial conditions, as indicated in (3.48). The attempt yields remarkable success, simplifying the difference between the expressions for the two boundary conditions. This difference can now be expressed in terms of the previously defined parameters, as presented in Equation (3.50). The result shows that the difference of the strain-stiffening effect under initial conditions is proportional to Λ_1 and χ, and inversely proportional to λ_L. It implies that the difference is mainly determined by the γ^2 and $(\lambda_2 - 1)$ terms in normal stress σ_{yy} and also the $\gamma(\lambda_2 - 1)$ term in shear stress σ_{xy}.

$$
\begin{aligned}
&\left(\frac{\partial^3\sigma_{xy}}{\partial\gamma^3}\right)_{\sigma_{yy}} \\
&= \left(\frac{\partial^3\sigma_{xy}}{\partial\gamma^3}\right)_{\lambda_2} + \left(\frac{\partial\sigma_{yy}}{\partial\lambda_2}\right)_{\gamma}^{-5}\left(\left(\frac{\partial\sigma_{yy}}{\partial\lambda_2}\right)_{\gamma}^{3}\left(3\left(\frac{\partial^2\sigma_{yy}}{\partial\lambda_2^2}\right)_{\gamma}^{2}\left(\frac{\partial\sigma_{xy}}{\partial\lambda_2}\right)_{\gamma} - 3\left(\frac{\partial\sigma_{yy}}{\partial\lambda_2}\right)_{\gamma}\left(\frac{\partial^2\sigma_{yy}}{\partial\lambda_2^2}\right)_{\gamma}\left(\frac{\partial^2\sigma_{xy}}{\partial\lambda_2^2}\right)_{\gamma}\right.\right. \\
&\quad + \left(\frac{\partial\sigma_{yy}}{\partial\lambda_2}\right)_{\gamma}\left(-\left(\frac{\partial\sigma_{xy}}{\partial\lambda_2}\right)_{\gamma}\left(\frac{\partial^3\sigma_{yy}}{\partial\lambda_2^3}\right)_{\gamma} + \left(\frac{\partial\sigma_{yy}}{\partial\lambda_2}\right)_{\gamma}\left(\frac{\partial^3\sigma_{xy}}{\partial\lambda_2^3}\right)_{\gamma}\right)\Big) \\
&\quad + 3\left(\frac{\partial\sigma_{yy}}{\partial\lambda_2}\right)_{\gamma}^{2}\left(\frac{\partial\sigma_{yy}}{\partial\lambda_2}\right)_{\gamma}\left(\left(\frac{\partial^2\sigma_{yy}}{\partial\lambda_2^2}\right)_{\gamma}\left(-3\left(\frac{\partial}{\partial\gamma}\left(\frac{\partial\sigma_{yy}}{\partial\lambda_2}\right)_{\gamma}\right)_{\lambda_2}\left(\frac{\partial\sigma_{xy}}{\partial\lambda_2}\right)_{\gamma} + \left(\frac{\partial\sigma_{yy}}{\partial\lambda_2}\right)_{\gamma}\left(\frac{\partial}{\partial\gamma}\left(\frac{\partial\sigma_{xy}}{\partial\lambda_2}\right)_{\gamma}\right)_{\lambda_2}\right)\right. \\
&\quad + \left(\frac{\partial\sigma_{yy}}{\partial\lambda_2}\right)_{\gamma}\left(2\left(\frac{\partial^2\sigma_{xy}}{\partial\lambda_2^2}\right)_{\gamma}\left(\frac{\partial}{\partial\gamma}\left(\frac{\partial\sigma_{yy}}{\partial\lambda_2}\right)_{\gamma}\right)_{\lambda_2} + \left(\frac{\partial\sigma_{xy}}{\partial\lambda_2}\right)_{\gamma}\left(\frac{\partial}{\partial\gamma}\left(\frac{\partial^2\sigma_{yy}}{\partial\lambda_2^2}\right)_{\gamma}\right)_{\lambda_2} - \left(\frac{\partial\sigma_{yy}}{\partial\lambda_2}\right)_{\gamma}\left(\frac{\partial}{\partial\gamma}\left(\frac{\partial^2\sigma_{xy}}{\partial\lambda_2^2}\right)_{\gamma}\right)_{\lambda_2}\right)\Big) \\
&\quad + \left(\frac{\partial\sigma_{yy}}{\partial\lambda_2}\right)_{\gamma}^{3}\left(3\left(\frac{\partial\sigma_{yy}}{\partial\lambda_2}\right)_{\gamma}\left(\frac{\partial^2\sigma_{yy}}{\partial\gamma^2}\right)_{\lambda_2}\left(\frac{\partial}{\partial\gamma}\left(\frac{\partial\sigma_{xy}}{\partial\lambda_2}\right)_{\gamma}\right)_{\lambda_2} + \left(\frac{\partial\sigma_{xy}}{\partial\lambda_2}\right)_{\gamma}\left(-3\left(\frac{\partial^2\sigma_{yy}}{\partial\gamma^2}\right)_{\lambda_2}\left(\frac{\partial}{\partial\gamma}\left(\frac{\partial\sigma_{yy}}{\partial\lambda_2}\right)_{\gamma}\right)_{\lambda_2}\right.\right. \\
&\quad + \left(\frac{\partial\sigma_{yy}}{\partial\lambda_2}\right)_{\gamma}\left(\frac{\partial^3\sigma_{yy}}{\partial\gamma^3}\right)_{\lambda_2}\Big)\Big) + 3\left(\frac{\partial\sigma_{yy}}{\partial\gamma}\right)_{\lambda_2}\left(\frac{\partial\sigma_{yy}}{\partial\lambda_2}\right)_{\gamma}^{2}\left(\left(\frac{\partial^2\sigma_{yy}}{\partial\lambda_2^2}\right)_{\gamma}\left(\frac{\partial\sigma_{xy}}{\partial\lambda_2}\right)_{\gamma}\left(\frac{\partial^2\sigma_{yy}}{\partial\gamma^2}\right)_{\lambda_2}\right. \\
&\quad + 2\left(\frac{\partial\sigma_{xy}}{\partial\lambda_2}\right)_{\gamma}\left(\frac{\partial}{\partial\gamma}\left(\frac{\partial\sigma_{yy}}{\partial\lambda_2}\right)_{\gamma}\right)_{\lambda_2}^{2} - \left(\frac{\partial\sigma_{yy}}{\partial\lambda_2}\right)_{\gamma}\left(\left(\frac{\partial^2\sigma_{xy}}{\partial\lambda_2^2}\right)_{\gamma}\left(\frac{\partial^2\sigma_{yy}}{\partial\gamma^2}\right)_{\lambda_2} + \left(\frac{\partial\sigma_{xy}}{\partial\lambda_2}\right)_{\gamma}\left(\frac{\partial}{\partial\lambda_2}\left(\frac{\partial^2\sigma_{yy}}{\partial\gamma^2}\right)_{\lambda_2}\right)_{\gamma}\right. \\
&\quad \left.\left. + 2\left(\frac{\partial}{\partial\gamma}\left(\frac{\partial\sigma_{yy}}{\partial\lambda_2}\right)_{\gamma}\right)_{\lambda_2}\left(\frac{\partial}{\partial\gamma}\left(\frac{\partial\sigma_{xy}}{\partial\lambda_2}\right)_{\gamma}\right)_{\lambda_2}\right) + \left(\frac{\partial\sigma_{yy}}{\partial\lambda_2}\right)_{\gamma}^{2}\left(\frac{\partial}{\partial\lambda_2}\left(\frac{\partial^2\sigma_{xy}}{\partial\gamma^2}\right)_{\lambda_2}\right)_{\gamma}\right)\Big)\Big).
\end{aligned}
\tag{3.47}
$$

$$
\gamma = 0, \quad \lambda_2 = 1: \qquad \left(\frac{\partial\sigma_{xy}}{\partial\lambda_2}\right)_{\gamma} = 0, \quad \left(\frac{\partial\sigma_{yy}}{\partial\gamma}\right)_{\lambda_2} = 0 \tag{3.48}
$$

$$
\begin{aligned}
\left[\left(\frac{\partial^3\sigma_{xy}}{\partial\gamma^3}\right)_{\sigma_{yy}} - \left(\frac{\partial^3\sigma_{xy}}{\partial\gamma^3}\right)_{\lambda_2}\right]_{\gamma=0,\lambda_2=1} &= \left[\frac{-3\left(\frac{\partial^2\sigma_{yy}}{\partial\gamma^2}\right)_{\lambda_2}\left(\frac{\partial}{\partial\lambda_2}\left(\frac{\partial\sigma_{xy}}{\partial\gamma}\right)_{\lambda_2}\right)_{\gamma}}{\left(\frac{\partial\sigma_{yy}}{\partial\lambda_2}\right)_{\gamma}}\right]_{\gamma=0,\lambda_2=1}, \\
&= -\frac{3\Lambda_1\chi}{\lambda_L}
\end{aligned}
\tag{3.49}
$$

However, the derivation does not stop here. From equation (3.39), we notice that the parameter Λ_1 can actually be substituted by the Poynting parameter χ with the relation $\Lambda_1 = -\chi$.

$$
\left[\left(\frac{\partial^3\sigma_{xy}}{\partial\gamma^3}\right)_{\sigma_{yy}} - \left(\frac{\partial^3\sigma_{xy}}{\partial\gamma^3}\right)_{\lambda_2}\right]_{\gamma=0,\lambda_2=1} = -\frac{3\Lambda_1\chi}{\lambda_L} = \frac{3\chi^2}{\lambda_L}. \tag{3.50}
$$

After the substitution, it becomes evident that the difference between the two boundary conditions can be entirely characterized by the normal stress response σ_{yy}. Furthermore, an intriguing conclusion

can be drawn from the expression: the sign of the Poynting effect does not influence the determination of the difference in the strain-stiffening effect. Instead, whether the constant normal stress boundary conditions or the constant height boundary conditions contribute to a greater stiffening effect is solely governed by the sign of λ_L, which corresponds to the $\lambda_2 - 1$ term. The magnitude of the difference is proportional to the square of χ and inversely proportional to λ_L.

To further analyze the influence of the material parameters κ/μ and how compressibility affects the difference in the strain-stiffening effect, a numerical study is conducted. Figure (3.10b) suggests that the value of Equation (3.50) would always be negative. Thus, the absolute value of the difference is plotted with respect to the κ/μ ratio.

Upon examining Figure (3.11), it is observed that changes in the parameter set (c, x) generate different results. The figure is presented in logarithmic scales on both the x- and y-axes. When $(c = 0.1, x = 0.1)$, the curve forms a straight line, indicating that the magnitude of the difference decreases exponentially with a constant exponent. On the other hand, when $(c = 0.1, x = 0.8)$, the curve is flat for a small κ/μ ratio. Then the slope gradually becomes stiffer so that at large κ/μ ratio, the slope is similar to the one when $(c = 0.1, x = 0.1)$. The slope at large ratio is contributed by the λ_L, which is the only variable that is dependent on κ in the expression. For large κ, λ_L can be approximated as $-\kappa/\mu$. Because for a certain set of (c, x), χ is a constant multiplies μ, the magnitude of the difference is proportional to $1/(\kappa/\mu)$ at large κ/μ ratios.

$$\frac{\kappa}{\mu} >> 1 : \qquad \left|\frac{3\chi^2}{\lambda_L}\right| \sim \frac{1}{\left(\frac{\kappa}{\mu}\right)}. \tag{3.51}$$

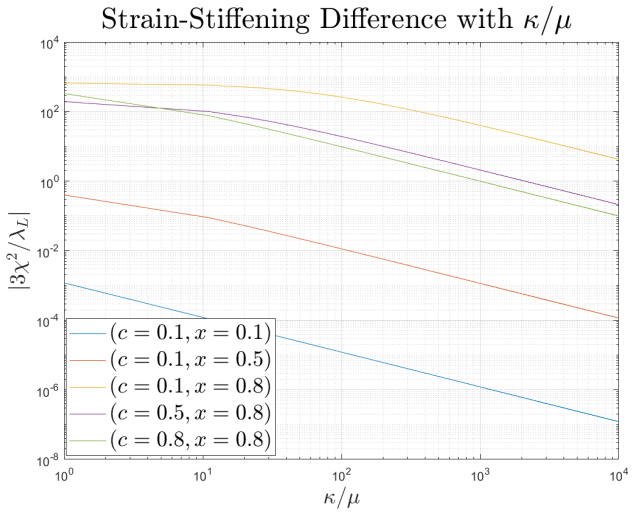

Figure 3.11: The strain stiffening effect performs differently under two boundary conditions. The difference could be characterized by $\left[\left(\frac{\partial^3 \sigma_{xy}}{\partial \gamma^3}\right)_{\sigma_{yy}} - \left(\frac{\partial^3 \sigma_{xy}}{\partial \gamma^3}\right)_{\lambda_2}\right]_{\gamma=0,\lambda_2=1}$, which is dependent on the compressibility κ/μ. The plot shows that different material sets may perform differently to the effect of compressibility. However, the slope always reaches $1/(\kappa/\mu)$ at a large ratio.

4

Introduce a general tensor

4.1. The formulation of a general deformation gradient tensor

In the last chapter, we adopted an innovative methodology to investigate the Poynting effect. This exploration encompassed an examination of the impact stemming from the inclusion of volumetric functions and the application of Taylor expansion techniques. Furthermore, we utilized this approach to examine the strain-stiffening effect under two common boundary conditions: constant normal stress and constant gap boundary conditions. Nevertheless, it is essential to note that the strain tensor employed in Chapter 3 only accommodates shear and a single dilation, presuming no deformation along the x- and z-directions. This presumption, though, is somewhat unwarranted since it does not account for the normal stresses in the x- and z-directions.

To provide a more comprehensive perspective on stress-strain responses, particularly in all three principal directions, we introduce a more general tensor, as represented in (4.1). This revision demands significant alterations. Firstly, the plane of deformation has shifted, with shear strain now being applied along the y-z plane, leading to an analysis of the Poynting effect in the z-direction. The definition of deformation has also undergone substantial changes. Along the principal x and y axes, deformation is characterized by ϵ/λ and $\epsilon\lambda$, respectively. Here, ϵ signifies the dilation of the x-y plane, while λ can be regarded as pure shear within the x-y plane. Notably, the element F_{yz} within the deformation gradient tensor appears complicated due to its formulation, which includes weighted factors, namely α, β, and δ, influencing the shear strain.

$$\mathbf{F} = \begin{bmatrix} \epsilon/\lambda & 0 & 0 \\ 0 & \epsilon\lambda & \gamma\xi^{\alpha}\epsilon^{\beta}\lambda^{\delta} \\ 0 & 0 & \xi \end{bmatrix} \tag{4.1}$$

While this element may initially appear complicated, we will simplify it using the Green-Lagrange tensor **E**, ultimately representing the element e_{yz} as just γ. Furthermore, given that the tensor includes seven variables, we require a minimum of six relationships to solve the equations. This is especially relevant since the shear strain γ typically serves as a controlled variable, to which we can assign a specific value. Therefore, our initial step involves deriving the Green-Lagrangian strain tensor to determine the values of the weighted factors. The Green-Lagrangian strain tensor **E** for the general tensor is presented below.

$$\begin{aligned} \mathbf{E} &= \frac{1}{2}\left(\mathbf{F}^{T}\mathbf{F} - \mathbf{I}\right) \\ &= \frac{1}{2}\begin{bmatrix} -1 + \frac{\epsilon^2}{\lambda^2} & 0 & 0 \\ 0 & -1 + \epsilon^2\lambda^2 & \gamma\xi^{\alpha}\epsilon^{1+\beta}\lambda^{1+\delta} \\ 0 & \gamma\xi^{\alpha}\epsilon^{1+\beta}\lambda^{1+\delta} & -1 + \xi^2 + \gamma^2\xi^2\alpha\epsilon^2\beta\lambda^2\delta \end{bmatrix} \end{aligned} \tag{4.2}$$

The Green-Lagrangian strain tensor quantifies how much the deformation tensor differs from the identity matrix **I**, which represents the undeformed state. As previously mentioned, since the term e_{yz} corresponds to the actual shear strain, we aim to relate γ with e_{yz}. Therefore, while alternative choices

for the weighted factors remain valid, we adopt the following relationships for our analysis.

$$\begin{aligned} &\gamma\xi^{\alpha}\epsilon^{1+\beta}\lambda^{1+\delta} = \gamma \\ \Rightarrow &\begin{cases} \alpha = 0 \\ \beta = -1\,. \\ \delta = -1 \end{cases} \end{aligned} \tag{4.3}$$

We have three unknowns to resolve: ξ, ϵ, and λ. These can be determined by imposing sufficient boundary conditions. Building upon the concept introduced in the previous chapter, we apply two distinct sets of boundary conditions. For each set, we define boundary conditions along the x, y, and z axes, respectively. The conditions specified for the x and y directions remain consistent across both cases, with variations appearing exclusively along the z-axis.

In the x and y directions, the boundary conditions assume that there is no normal stress, regardless of how the material undergoes deformation. This assumption is grounded in the experimental setup, where the inclined face of the material subjected to shear is typically unconstrained. As a result, instead of generating stress, the response in these two directions is expected to present as deformations.

On the other hand, the z-axis is typically confined by plates, leading to a boundary condition characterized by a constant gap. This condition may also induce a constant normal stress boundary condition if the external load is fixed. The formulations of these boundary conditions are presented in the following equation:

$$\begin{aligned} x: &\quad \sigma_{xx} = 0 \\ y: &\quad \sigma_{yy} = 0 \\ z: &\quad \begin{cases} \text{const. normal stress} & \sigma_{zz} = 0, \xi \neq 0 \\ \text{const. gap} & \sigma_{zz} \neq 0, \xi = 0 \end{cases}. \end{aligned} \tag{4.4}$$

With the questions of interest now fully defined, we are prepared to solve for all the unknowns. Meng's model, including the volumetric part, is now represented as (4.5).

$$\begin{aligned} W = &\frac{1}{2}\kappa\left(-1+\epsilon^2\xi\right)^2 + \frac{1}{3}\mu\left(c\pi^2\left(3 - \frac{x^2\left(\epsilon^2\left(\frac{1}{\lambda^2}+\lambda^2\right)+\xi^2+\frac{\gamma^2}{\epsilon^2\lambda^2}\right)}{\left(\epsilon^2\xi\right)^2}\right)\right. \\ &\left. + \frac{-3\epsilon^2\lambda^4\left(\epsilon^2\xi\right)^{4/3} + 2x^2\lambda^2\left(\epsilon^2\xi\right)^{2/3}\left(\gamma^2+\epsilon^4\left(1+\lambda^4\right)+\epsilon^2\lambda^2\xi^2\right) - x^4\epsilon^2\left(\gamma^2+\epsilon^4\lambda^4+\epsilon^2\lambda^2\left(1+\lambda^4\right)\xi^2\right)}{c\pi\left(\left(x^6-1\right)\epsilon^{14/3}\lambda^4\xi^{4/3} + x^2\lambda^2\left(\epsilon^2\xi\right)^{2/3}\left(\gamma^2+\epsilon^4\left(1+\lambda^4\right)+\epsilon^2\lambda^2\xi^2\right) - x^4\epsilon^2\left(\gamma^2+\epsilon^4\lambda^4+\epsilon^2\lambda^2\xi^2\left(1+\lambda^4\right)\right)\right)}\right) \end{aligned} \tag{4.5}$$

4.2. Stress-strain response

Following the procedure used in the last chapter, we commence by working from equation (3.20) to derive the stress responses in all three normal directions, as well as the shear stress on the y-z plane. Due to the complexity of the expressions involved, we will refrain from presenting the exact stress expressions in this chapter. Instead, we opt for a Taylor expansion of the stress expressions concerning four variables: γ, ϵ, λ, and ξ. Each of these variables is expanded around their initial points, which are set as 0, 1, 1, and 1, respectively.

$$\begin{aligned} \sigma_{zz} = &(-1+\epsilon)\left(2\kappa + \frac{8(x^2 - c^2\pi^3x^2 + x^4 + 3c^2\pi^3x^4 - 3c^2\pi^3x^6 + c^2\pi^3x^8)\mu}{9c\pi(-1+x^2)^3}\right) \\ &+ \gamma^2\left(\frac{2(x^2 + c^2\pi^3x^2 + 2x^4 - 4c^2\pi^3x^4 + 2x^6 + 6c^2\pi^3x^6 - 4c^2\pi^3x^8 + c^2\pi^3x^{10})\mu}{9c\pi(-1+x^2)^4}\right) \\ &+ (-1+\xi)\left(\kappa - \frac{8(x^2 - c^2\pi^3x^2 + x^4 + 3c^2\pi^3x^4 - 3c^2\pi^3x^6 + c^2\pi^3x^8)\mu}{9c\pi(-1+x^2)^3}\right) \end{aligned} \tag{4.6}$$

After Taylor's expansion is applied, we proceed to simplify the expressions by neglecting higher-order terms. In the case of variables $\epsilon - 1$, $\lambda - 1$, and $\xi - 1$, only the first-order terms remain in the normal stress expressions. On the other hand, these variables can be combined with a γ term in the shear stress response since we assume that γ is significantly larger than the deformations in the principal directions. The quadratic and cubic terms of γ are left in the normal stress and shear stress responses because they are the main contributors to the strain-stiffening effect. The Taylor expression form of the stress responses are shown from equation (4.6) to (4.9).

$$\begin{aligned}\sigma_{yy} =& -(-1+\lambda)\frac{4(x^2 - c^2\pi^3x^2 + x^4 + 3c^2\pi^3x^4 - 3c^2\pi^3x^6 + c^2\pi^3x^8)\mu}{3c\pi(-1+x^2)^3} \\ &+ \frac{(-1+\epsilon)}{9}\left(18\kappa - \frac{4x^4(2+x^2)\mu}{c\pi(-1+x^2)^4} + \frac{x^2(4 - 12x^4 + 8x^6 - 4c^2\pi^3(-1+3x^2-3x^4+x^6)^2)\mu}{c\pi(-1+x^2)^6}\right) \\ &- \gamma^2\left(\frac{2(-2x^2 + 2c^2\pi^3x^2 - 2x^4 - 8c^2\pi^3x^4 + x^6 + 12c^2\pi^3x^6 - 8c^2\pi^3x^8 + 2c^2\pi^3x^{10})\mu}{9c\pi(-1+x^2)^4}\right) \\ &+ (-1+\xi)\left(\frac{-9c\pi\kappa(1-x^6) + 27c\pi\kappa(x^2-x^4) + 4x^2\mu - 4c^2\pi^3\mu(x^2-x^8) + 4x^4\mu + 12c^2\pi^3\mu(x^4-x^6)}{9c\pi(-1+x^2)^3}\right).\end{aligned} \tag{4.7}$$

$$\begin{aligned}\sigma_{xx} =& (-1+\lambda)\frac{4(x^2 - c^2\pi^3x^2 + x^4 + 3c^2\pi^3x^4 - 3c^2\pi^3x^6 + c^2\pi^3x^8)\mu}{3c\pi(-1+x^2)^3} \\ &+ (-1+\epsilon)\left(2\kappa - \frac{4x^4(2+x^2)\mu}{9c\pi(-1+x^2)^4} + \frac{x^2(4 - 12x^4 + 8x^6 - 4c^2\pi^3(-1+3x^2-3x^4+x^6)^2)\mu}{9c\pi(-1+x^2)^6}\right) \\ &+ \gamma^2\left(\frac{2(-x^2 + c^2\pi^3x^2 - 4x^4 - 4c^2\pi^3x^4 - x^6 + 6c^2\pi^3x^6 - 4c^2\pi^3x^8 + c^2\pi^3x^{10})\mu}{9c\pi(-1+x^2)^4}\right) \\ &+ (-1+\xi)\left(\kappa + \frac{4x^4(2+x^2)\mu}{9c\pi(-1+x^2)^4} + \frac{4x^2(-1 + c^2\pi^3 - 2x^2 - 4c^2\pi^3x^2 + 6c^2\pi^3x^4 - 4c^2\pi^3x^6 + c^2\pi^3x^8)\mu}{9c\pi(-1+x^2)^4}\right).\end{aligned} \tag{4.8}$$

$$\begin{aligned}\sigma_{yz} =& \gamma^3\left(-\frac{4x^4(-1+x^4)\mu}{3c\pi(-1+x^2)^6} + \frac{4x^4(-3+6x^2+7x^4)(-1+\lambda)\mu}{3c\pi(-1+x^2)^6}\right) \\ &+ \gamma\left(-\frac{2x^2(1 - c^2\pi^3 + x^2 + 3c^2\pi^3x^2 - 3c^2\pi^3x^4 + c^2\pi^3x^6)\mu}{3c\pi(-1+x^2)^3}\right. \\ &+ (-1+\lambda)\frac{2x^2(-1 + c^2\pi^3 + 4x^2 - 4c^2\pi^3x^2 + 3x^4 + 6c^2\pi^3x^4 - 4c^2\pi^3x^6 + c^2\pi^3x^8)\mu}{3c\pi(-1+x^2)^4} \\ &+ (-1+\epsilon)\frac{2x^2(-13 + 13c^2\pi^3 - 4x^2 - 52c^2\pi^3x^2 + 11x^4 + 78c^2\pi^3x^4 - 52c^2\pi^3x^6 + 13c^2\pi^3x^8)\mu}{9c\pi(-1+x^2)^4} \\ &\left.+(-1+\xi)\frac{4x^2(-1 + c^2\pi^3 + 2x^2 - 4c^2\pi^3x^2 + 2x^4 + 6c^2\pi^3x^4 - 4c^2\pi^3x^6 + c^2\pi^3x^8)\mu}{9c\pi(-1+x^2)^4}\right)\end{aligned} \tag{4.9}$$

In equation (4.6), it becomes evident that the transverse normal stress σ_{zz} is solely dependent on γ, ϵ, and ξ. This suggests that the shear on the x-y plane exerts no influence on the Poynting effect. On the other hand, the normal stresses in the other two directions, σ_{xx} and σ_{yy}, are both correlated with all four variables. It is worth emphasizing that the γ^2 terms in the normal stresses are unrelated to the bulk modulus. This implies that, for this specific formulation and strain energy function, the strain-stiffening effect is primarily unaffected by the choice of bulk modulus. This observation extends to the cubic γ term in the shear stress as well. In fact, we notice that the shear stress response remains entirely independent of the bulk modulus.

4.3. Derivation of the Poynting parameter

In the last chapter, we introduced a method to predict the sign of the Poynting effect. This method, under the assumption that stress and strain responses in the normal direction are monotonic at small

deformations, demonstrated a strong alignment with the obtained results. Thus, in this chapter, we follow the same procedure to derive the expression for the Poynting parameter. We will then utilize this parameter to predict the sign of the Poynting effect. The following section will present a comparison between these predictions and the analytical solutions.

To start, we need the expression for the differential of the Green-Lagrangian strain tensor, denoted as $d\mathbf{E}$. Calculating the total derivative involves four variables, hence requiring the use of four matrices, as illustrated in equation (4.10).

$$d\mathbf{E} = \left(\frac{\partial \mathbf{E}}{\partial \lambda}\right)_{(\gamma,\epsilon,\xi)} d\lambda + \left(\frac{\partial \mathbf{E}}{\partial \gamma}\right)_{(\lambda,\epsilon,\xi)} d\gamma + \left(\frac{\partial \mathbf{E}}{\partial \epsilon}\right)_{(\gamma,\lambda,\xi)} d\epsilon + \left(\frac{\partial \mathbf{E}}{\partial \xi}\right)_{(\gamma,\lambda,\epsilon)} d\xi,$$

where

$$\left(\frac{\partial \mathbf{E}}{\partial \lambda}\right)_{(\gamma,\epsilon,\xi)} = \begin{bmatrix} -\frac{\epsilon^2}{\lambda^3} & 0 & 0 \\ 0 & \epsilon^2\lambda & 0 \\ 0 & 0 & -\frac{\gamma^2}{\epsilon^2\lambda^3} \end{bmatrix}, \quad \left(\frac{\partial \mathbf{E}}{\partial \gamma}\right)_{(\lambda,\epsilon,\xi)} = \begin{bmatrix} 0 & 0 & 0 \\ 0 & 0 & \frac{1}{2} \\ 0 & \frac{1}{2} & \frac{\gamma}{\epsilon^2\lambda^2} \end{bmatrix},$$

$$\left(\frac{\partial \mathbf{E}}{\partial \epsilon}\right)_{(\gamma,\lambda,\xi)} = \begin{bmatrix} \frac{\epsilon}{\lambda^2} & 0 & 0 \\ 0 & \epsilon\lambda^2 & 0 \\ 0 & 0 & -\frac{\gamma^2}{\epsilon^3\lambda^2} \end{bmatrix}, \quad \left(\frac{\partial \mathbf{E}}{\partial \xi}\right)_{(\gamma,\lambda,\epsilon)} = \begin{bmatrix} 0 & 0 & 0 \\ 0 & 0 & 0 \\ 0 & 0 & \xi \end{bmatrix} \tag{4.10}$$

Continuing with the same approach, we derive the expression for the second Piola-Kirchhoff stress, denoted as **S**, and apply the same Cauchy stress tensor, as given in equation (3.35). We arrive at the expression for dW, as presented in equation (4.11).

$$dW = \frac{\epsilon}{2\lambda\xi}\left(-\epsilon\xi\left(2\xi(\sigma_{xx}-\sigma_{yy}) + \frac{4\gamma\sigma_{yz}}{\epsilon\lambda}\right)d\lambda + \lambda\left(\xi\left(2\xi(\sigma_{xx}+\sigma_{yy}) - \frac{4\gamma\sigma_{yz}}{\epsilon\lambda}\right)d\epsilon + \epsilon\left(\frac{2\xi\sigma_{yz}}{\epsilon\lambda}d\gamma + 2\xi\sigma_{zz}d\xi\right)\right)\right) \tag{4.11}$$

The general tensor utilizes four unknowns, allowing us to formulate six Maxwell's relations. However, upon examining the equations, it becomes obvious that the normal stress in the z-direction, denoted as σ_{zz}, is solely associated with the variable $d\xi$. Therefore, there are only three relations directly connected to σ_{zz}, as illustrated in equations (4.12) through (4.14).

Maxwell's relation (1)

$$\begin{aligned} \left(\frac{\partial}{\partial\gamma}\left(\frac{\partial W}{\partial \xi}\right)\right) &= \left(\frac{\partial}{\partial\xi}\left(\frac{\partial W}{\partial \gamma}\right)\right) \\ \Rightarrow \epsilon^2\frac{\partial\sigma_{zz}}{\partial\gamma} &= \frac{\epsilon}{\lambda}\frac{\partial\sigma_{yz}}{\partial\xi} \end{aligned} \tag{4.12}$$

Maxwell's relation (2)

$$\begin{aligned} \left(\frac{\partial}{\partial\lambda}\left(\frac{\partial W}{\partial \xi}\right)\right) &= \left(\frac{\partial}{\partial\xi}\left(\frac{\partial W}{\partial \lambda}\right)\right) \\ \Rightarrow \epsilon^2\frac{\partial\sigma_{zz}}{\partial\lambda} &= -\frac{\epsilon}{\lambda^2}\left(\epsilon\lambda\left(\sigma_{xx}-\sigma_{yy}+\xi\frac{\partial\sigma_{xx}}{\partial\xi}-\xi\frac{\partial\sigma_{yy}}{\partial\xi}\right)+2\gamma\frac{\partial\sigma_{yz}}{\partial\xi}\right) \end{aligned} \tag{4.13}$$

Maxwell's relation (3)

$$\begin{aligned} \left(\frac{\partial}{\partial\epsilon}\left(\frac{\partial W}{\partial \xi}\right)\right) &= \left(\frac{\partial}{\partial\xi}\left(\frac{\partial W}{\partial \epsilon}\right)\right) \\ \Rightarrow \epsilon\left(2\sigma_{zz}+\epsilon\frac{\partial\sigma_{zz}}{\partial\epsilon}\right) &= \epsilon\left(\sigma_{xx}+\sigma_{yy}+\xi\left(\frac{\partial\sigma_{xx}}{\partial\xi}+\frac{\partial\sigma_{yy}}{\partial\xi}\right)\right)-\frac{2\gamma}{\lambda}\frac{\partial\sigma_{yz}}{\partial\xi} \end{aligned} \tag{4.14}$$

Again, we intend to follow the same procedure used in the previous chapter. Our objective is to derive the expression for the term $(\partial^2\sigma_{zz}/\partial\gamma^2)_{(\gamma,\epsilon,\lambda)}$ under the initial conditions. We will only need to take one additional derivative with respect to γ and incorporate it into the equation to obtain the desired result. Reviewing the equations provided, it becomes evident that only the first Maxwell relation, as denoted

in (4.12), is capable of meeting this requirement.

First, we take derivative of the equation with respect to γ.

$$\begin{aligned} &\left(\frac{\partial^2}{\partial\gamma^2}\left(\frac{\partial W}{\partial\xi}\right)\right) = \left(\frac{\partial}{\partial\gamma}\left(\frac{\partial}{\partial\xi}\left(\frac{\partial W}{\partial\gamma}\right)\right)\right) \\ \Rightarrow &\epsilon^2\frac{\partial^2\sigma_{zz}}{\partial\gamma^2} = \frac{\epsilon}{\lambda}\left(\frac{\partial}{\partial\gamma}\left(\frac{\partial\sigma_{yz}}{\partial\xi}\right)\right), \\ \text{Apply initial consitions:} \quad &\Rightarrow -\chi = \left(\frac{\partial}{\partial\gamma}\left(\frac{\partial\sigma_{yz}}{\partial\xi}\right)\right) \end{aligned} \tag{4.15}$$

A surprising result is shown here. The ability to predict the sign of the Poynting effect is entirely dependent on the $\gamma\xi$ term within the shear stress response, regardless of the chosen strain tensor. We derive this expression from equation (4.9), yielding the following result:

$$\chi = -\frac{4x^2(-1+c^2\pi^3+2x^2-4c^2\pi^3x^2+2x^4+6c^2\pi^3x^4-4c^2\pi^3x^6+c^2\pi^3x^8)\mu}{9c\pi(-1+x^2)^4} \tag{4.16}$$

In the previous chapter, we discussed how the Poynting coefficient χ alone was sufficient to predict the sign of the Poynting effect under constant gap boundary conditions. This simplicity arose because λ_2 was set to one, leaving only one term in the normal stress expression. The coefficient could also be extended to predict the sign under constant normal stress boundary conditions. This was due to the combined influence of the sign of χ and λ_L on the normal strain response, with λ_L consistently being negative. As a result, the sign of the normal strain $\lambda_2 - 1$, expressed as $-\chi/\lambda_L$, always matched the sign of χ.

In this chapter, however, the tensor involves more unknowns, and the expression for normal stress is considerably more complex. Therefore, we follow the same fundamental concept but derive an expression to predict the sign of the Poynting effect for constant normal stress boundary conditions.

It is important to note that the Poynting effect is closely tied to the Poynting parameter χ, which means that our derivation will consist of the term $(\partial^2\sigma_{zz}/\partial\gamma^2)$. The key difference in this derivation, compared to the previous chapter, lies in the formulation of the transverse deformation gradient element ξ as a function of the unknowns γ, ϵ, λ, and the normal stress σ_{zz}. This formulation allows us to derive Maxwell's relations while accounting for the normal stress σ_{zz}.

The derivation will start from equation (4.11) in the previous subsection. The first Maxwell's relation is derived based on the new formulation of ξ.

$$\begin{aligned} &\left(\frac{\partial}{\partial\xi}\left(\frac{\partial W}{\partial\gamma}\right)\right) = \left(\frac{\partial}{\partial\gamma}\left(\frac{\partial W}{\partial\xi}\right)\right) \\ \Rightarrow &0 = \epsilon^2\left(\frac{\partial\sigma_{zz}}{\partial\xi}\frac{\partial\xi}{\partial\gamma} + \frac{\partial\sigma_{zz}}{\partial\gamma}\right). \end{aligned} \tag{4.17}$$

Then, we take a derivative of the equation with respect to γ and obtain equation (4.18).

$$\begin{aligned} &\left(\frac{\partial}{\partial\gamma}\left(\frac{\partial}{\partial\xi}\left(\frac{\partial W}{\partial\gamma}\right)\right)\right) = \left(\frac{\partial^2}{\partial\gamma^2}\left(\frac{\partial W}{\partial\xi}\right)\right) \\ \Rightarrow &0 = \frac{\partial\xi}{\partial\gamma}\left(\frac{\partial}{\partial\gamma}\left(\frac{\partial\sigma_{zz}}{\partial\xi}\right)\right) + \frac{\partial\xi}{\partial\gamma}\left(\frac{\partial^2\sigma_{zz}}{\partial\xi^2}\frac{\partial\xi}{\partial\gamma} + \left(\frac{\partial}{\partial\xi}\left(\frac{\partial\sigma_{zz}}{\partial\gamma}\right)\right)\right) + \frac{\partial\sigma_{zz}}{\partial\xi}\frac{\partial^2\xi}{\partial\gamma^2} + \frac{\partial^2\sigma_{zz}}{\partial\gamma^2}. \end{aligned} \tag{4.18}$$

During the derivation, we observe that the derived relation is solely associated with the expression of the normal stress σ_{zz}. Therefore, we proceed by applying the initial condition to equation (4.18). Given the Taylor expansion of σ_{zz}, as expressed in equation (4.6), it becomes evident that the terms $\left(\partial^2\sigma_{zz}/\partial\gamma\partial\xi\right)$ and $\left(\partial^2\sigma_{zz}/\partial\xi^2\right)$ will result in zero under the initial conditions.

$$\text{Initial conditions:} \quad 0 = \frac{\partial\sigma_{zz}}{\partial\xi}\frac{\partial^2\xi}{\partial\gamma^2} + \frac{\partial^2\sigma_{zz}}{\partial\gamma^2}. \tag{4.19}$$

From the expression above, we identify that the term $\partial^2\xi/\partial\gamma^2$ could be used to predict the sign of the Poynting effect.

$$\text{Initial conditions:} \quad \frac{\partial^2\xi}{\partial\gamma^2} = -\frac{\frac{\partial^2\sigma_{zz}}{\partial\gamma^2}}{\frac{\partial\sigma_{zz}}{\partial\xi}} = -\frac{\chi}{\lambda_L}. \tag{4.20}$$

Again, referring to equation (4.6), we can re-express the expression in terms of the material parameters, as demonstrated in equation (4.21). Given that the parameter λ_L depends on the bulk modulus κ, we anticipate that the sign of the Poynting effect may also be influenced by the magnitude of κ.

$$\left(\frac{\partial^2\xi}{\partial\gamma^2}\right)_0 = \frac{4x^2(-1+c^2\pi^3+2x^2-4c^2\pi^3x^2+2x^4+6c^2\pi^3x^4-4c^2\pi^3x^6+c^2\pi^3x^8)\mu}{\kappa(9c\pi(-1+x^2)^4)-8(x^2-c^2\pi^3x^2+x^4+3c^2\pi^3x^4-3c^2\pi^3x^6+c^2\pi^3x^8)\mu(9c\pi(-1+x^2))} \tag{4.21}$$

A parameter study is also presented below for the sake of comparison in the upcoming section. We have plotted both the Poynting parameter χ and the equivalent parameter $-\chi/\lambda_L$ concerning various stiffness parameters c and the end-to-end ratio x. These plots are displayed in figures (4.1a) and (4.1b), respectively.

The study reveals that the prediction regarding the sign of the Poynting effect holds true universally for both boundary conditions. This means that if the Poynting effect is negative for a given parameter set under constant normal stress boundary conditions, it should also exhibit a negative Poynting effect under constant gap boundary conditions. Also, it implies that the Poisson's ratio has no influence on the sign of the Poynting effect under either boundary condition.

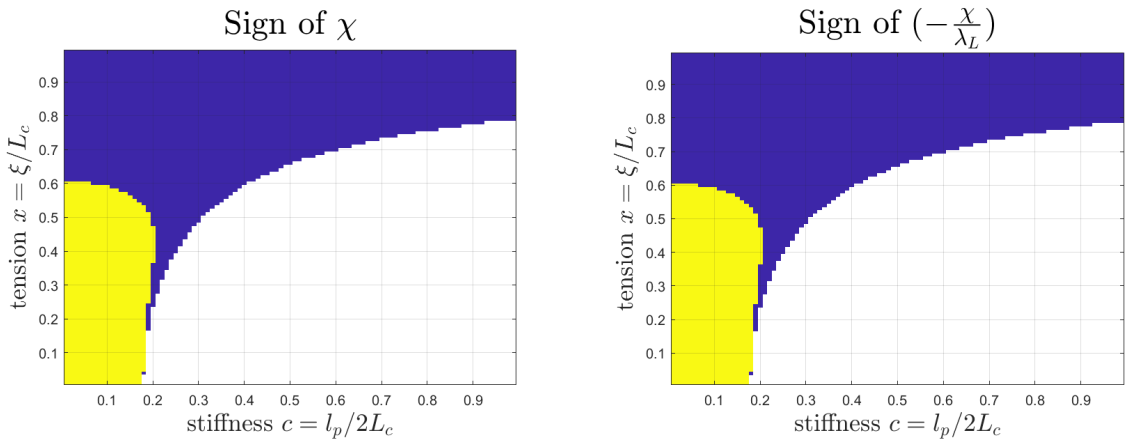

(a) (b)

Figure 4.1: (a) The sign of χ, which predicts the sign of the Poyntign effect under constant gap B.C.; (b) The sign of $-\chi/\lambda_L$, which predicts the sign under constant normal stress B.C..

4.4. Results

In this section, we present the results of the numerical study for both boundary conditions. The stress and strain responses have been calculated using the Taylor expansion form of the stress expressions. The numerical values are obtained using the built-in function $solve$ in Matlab.

4.4.1. Constant Gap

First, let's consider the sign of the Poynting effect under constant gap boundary conditions, examining the influence of Poisson's ratio. We have explored two scenarios for the bulk modulus: one where it has the same magnitude as the shear modulus, denoted as $\kappa/\mu = 1$ (as seen in Figure(4.2a)), and another where the bulk modulus is a thousand times larger than the shear modulus, represented as $\kappa/\mu = 1000$ (as shown in Figure(4.2b)).

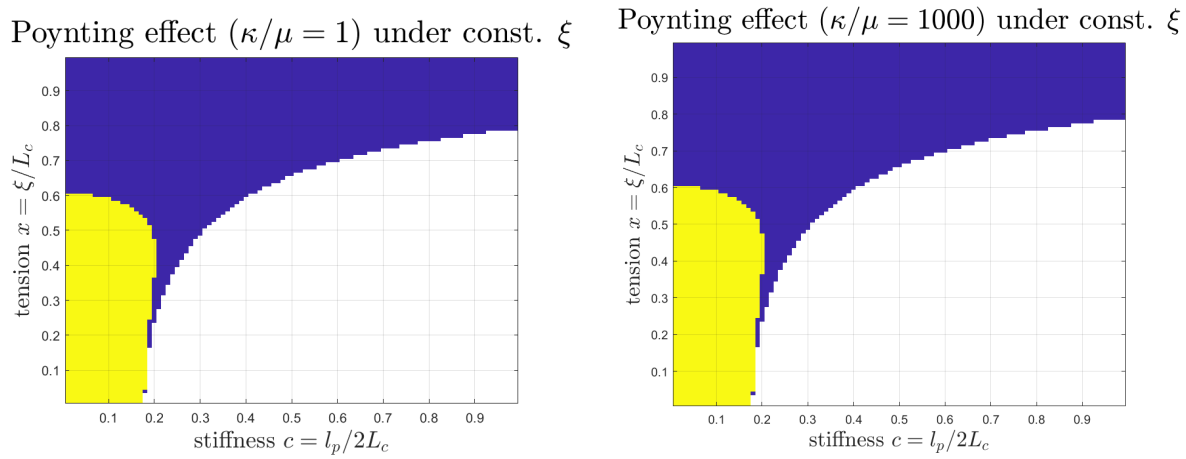

(a) (b)

Figure 4.2: The sign of the Poynting effect shows the identical distribution, where yellow region represents positive Poynting effect and dark blue represents negative Poynting effect, for moduli ratio κ/μ equals (a) 1, (b) 1000.

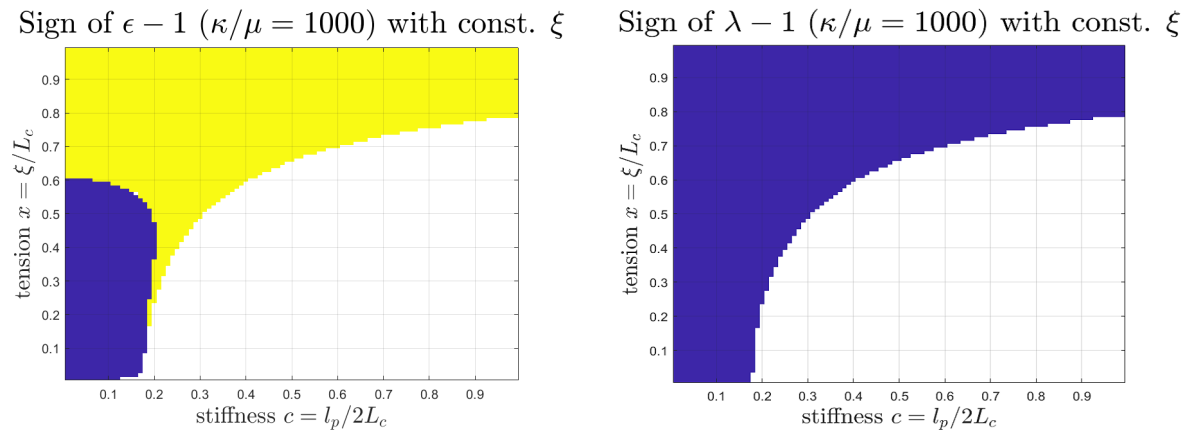

(a) (b)

Figure 4.3: (a) The sign of $\epsilon - 1$ shows the dilational factor on x and y direction. For the positive Poynting effect, the factor is negative (dark blue region), and vice versa. (b) shows the sign of $\lambda - 1$, implying that the distortional factor is always negative.

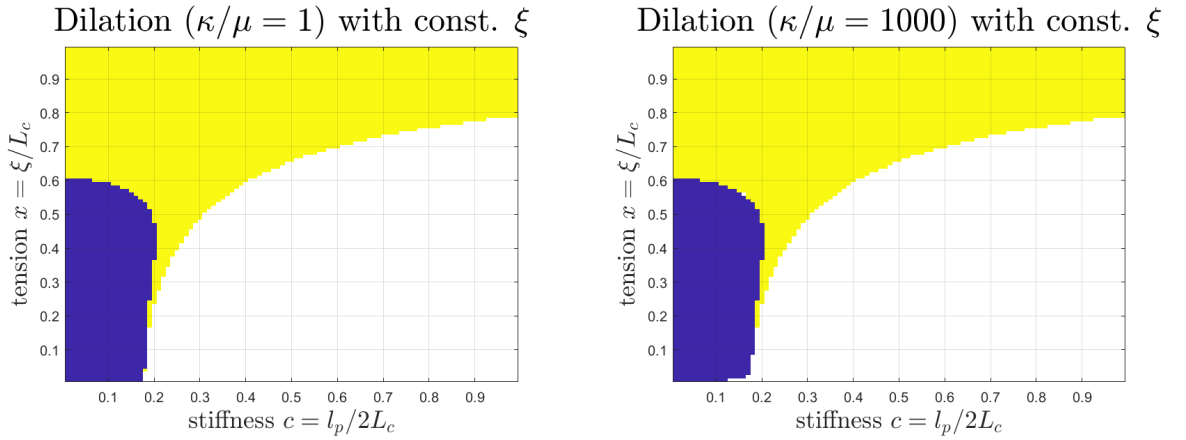

(a) (b)

Figure 4.4: The dilation plots compute the volume ratio change $J - 1$ and they show expansion, $J > 1$, (yellow) under negative Poynting effect and contraction, $J < 1$, (blue) under positive Poynting effect when κ/μ equals (a) 1 and (b) 1000.

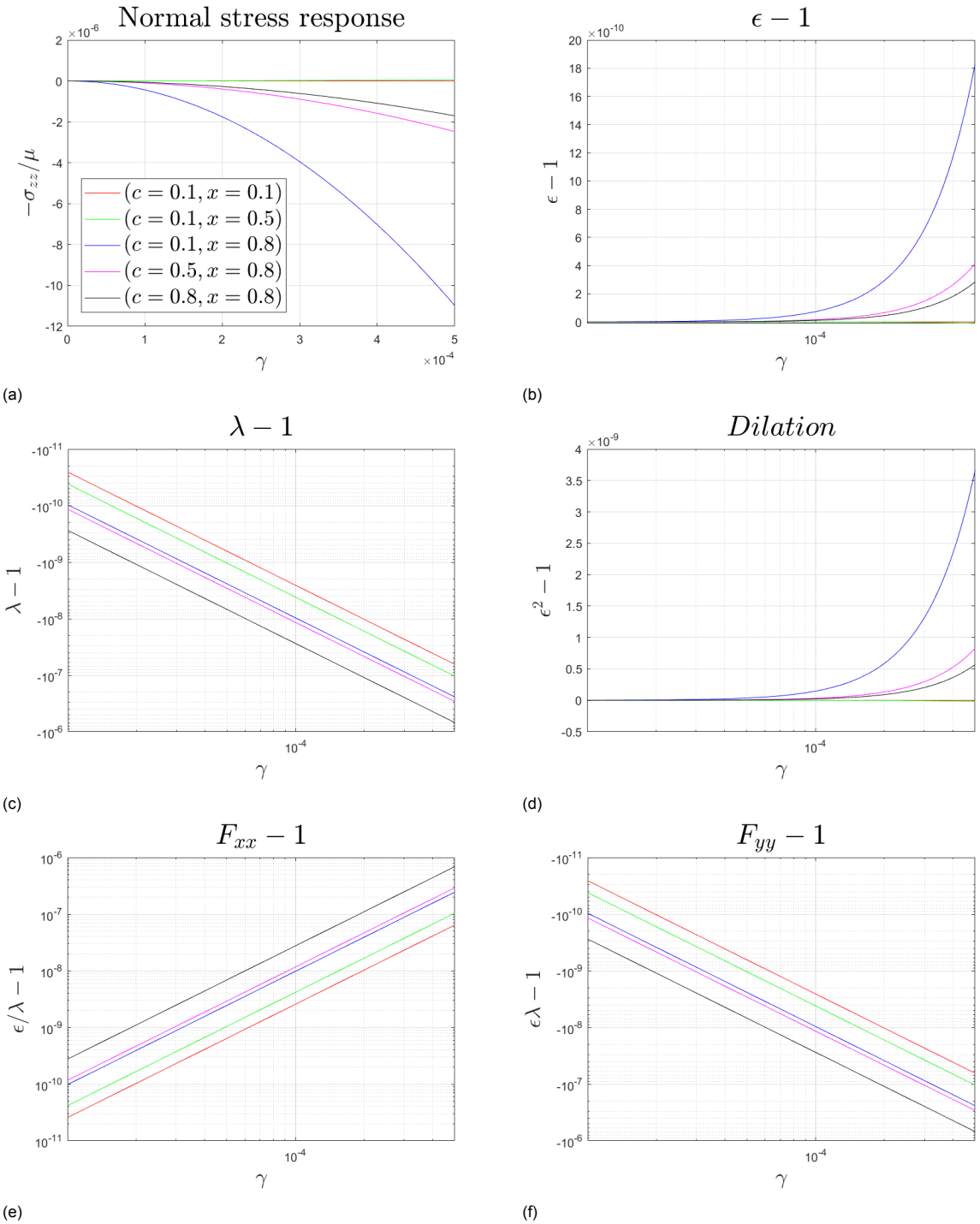

Figure 4.5: Five material sets are chosen to study the response under $\kappa/\mu = 1000$. The adimensional normal stress-strain curve is shown in (a). ϵ, λ, and dilation curves with respect to applied shear strain γ are shown in (b), (c), and (d). The deformation gradient element F_{xx} and F_{yy} are shown in (e) and (f).

In equation (4.21), it is apparent that the Poynting effect depends on the bulk modulus. However, the computational results indicate that the bulk modulus does not play a role in determining the sign of the Poynting effect. This phenomenon arises from the fact that the bulk modulus cannot alter the sign of the denominator in equation (4.21).

The use of the general tensor enables us to account for deformations in the x and y directions. Since the distribution of the sign of $\epsilon - 1$ and $\lambda - 1$ remains consistent for all Poisson's ratios, we will present

just one case, $\kappa/\mu = 1000$, to represent the results. The distribution of the sign of the variable $\epsilon - 1$ is illustrated in Figure(4.3a), and it exhibits an opposite sign compared to the Poynting effect. Since ϵ refers to the dilational factor in the x and y directions, this result aligns with the assumption that when the system exhibits a positive Poynting effect, it has a tendency to contract in the other two directions.

On the other hand, the distribution of $\lambda - 1$ is consistently negative for all parameter sets and for all choices of bulk modulus, as shown in Figure(4.3b). Given that λ signifies shear on the xy plane, this result implies that regardless of the sign of the Poynting effect, the system tends to stretch in the x direction and contract in the y direction. It is important to note that even though we have knowledge of the distribution of $\epsilon - 1$ and $\lambda - 1$, the actual deformation gradient factors F_{xx} and F_{yy} still require further calculation, as will be shown later.

Figure(4.4) presents the dilation of the system under shear. This behavior, whether the system contracts or expands as a whole, is not influenced by the bulk moduli either. Moreover, it exhibits an opposing trend in relation to the sign of the Poynting effect. Specifically, when a positive Poynting effect occurs, indicating that the system tends to expand in the transverse direction, the volume of the system actually decreases.

Finally, we have chosen five sets of material parameters to study the change in magnitude of the system under increasing shear strain. We specifically focus on the deformation gradient elements F_{xx} and F_{yy}. Figure(4.5e) and (4.5f) demonstrate that regardless of how the material parameters change, the system consistently undergoes expansion in the x direction and contraction in the y direction. These results indicate that when shear is applied to the yz plane, the system experiences shear on the xy plane.

4.4.2. Constant Normal Stress

In this subsection, we investigate the system's response under constant normal stress boundary conditions. As we demonstrated in the previous subsection, the bulk-to-shear ratio does not impact the sign of the Poynting effect. Additionally, we observe that the sign of the Poynting effect is not linked to this ratio, in alignment with the expression of χ outlined in equation (4.16). Therefore, we present just one figure as a representation of our findings.

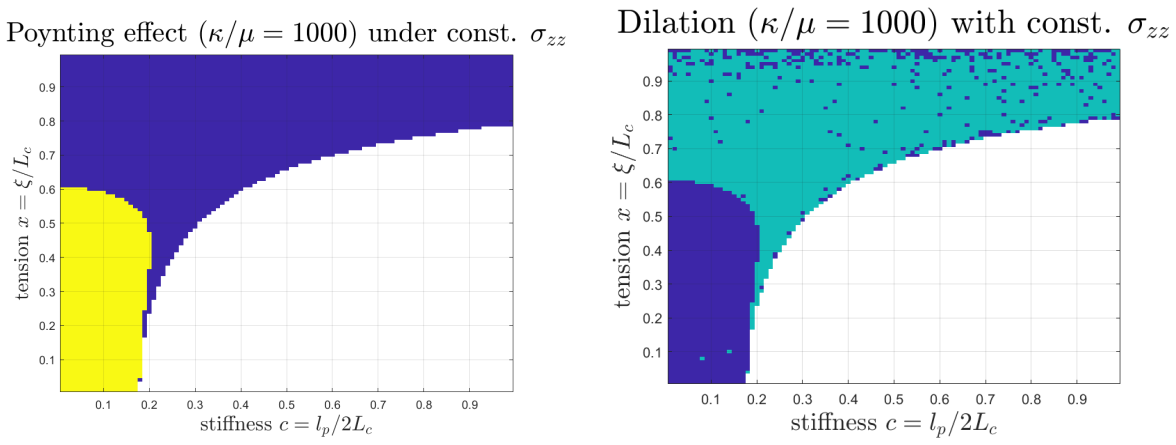

(a) (b)

Figure 4.6: The sign of the Poynting effect under constant normal stress boundary conditions is depicted in (a), while the change in dilation $J - 1$ is shown in (b). In (a), the yellow region and dark blue region represent positive and negative Poynting effects, respectively. In (b), the light blue region and dark blue region correspond to $J - 1$ changing sign under different γ and $J - 1$ monotonically decreasing below zero, respectively. It is noteworthy that this distribution remains consistent regardless of the value of the compressibility parameter κ/μ.

The normal stress response $-\sigma_{zz}$ showcases the same distribution as the Poynting parameter, affirming its effectiveness in predicting the sign of the Poynting effect. Moreover, the distributions under both boundary conditions are identical, indicating that the sign of the Poynting effect solely hinges on the

material parameters and remains independent of the boundary conditions. The distributions of $\epsilon - 1$ and $\lambda - 1$ also mirror those presented in the previous section.

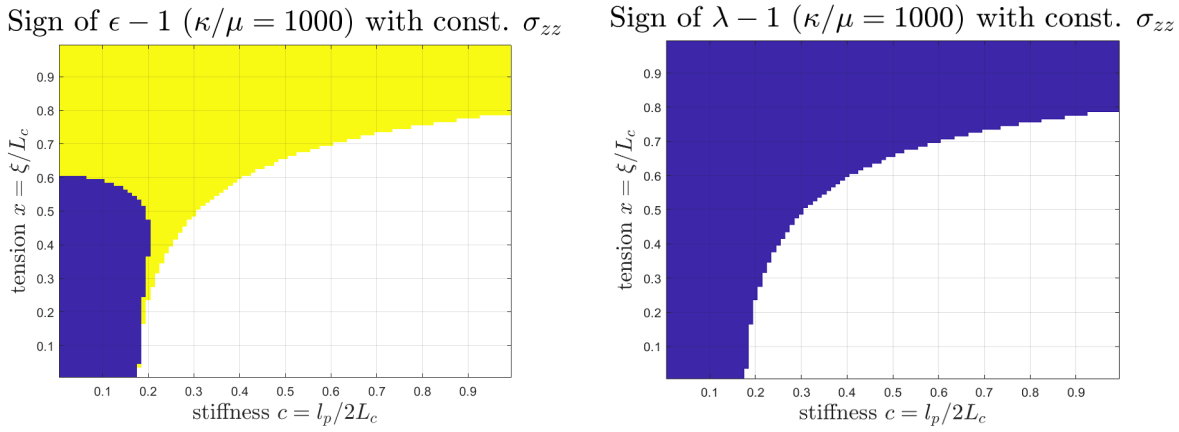

(a) (b)

Figure 4.7: The sign of $\epsilon - 1$ and $\lambda - 1$ under constant normal stress B.C is . is shown in (a) and (b), respectively. The distributions do not change with the compressibility κ/μ and they are identical to the one under constant gap B.C..

However, the dilation of the object exhibits a complex pattern in Figure(4.6b). The light blue region corresponds to situations where, with the increase of shear strain, the change in volume ratio $J - 1$ crosses zero. This means that it is not monotonically increasing or decreasing, as can be observed in the zoom-in section of Figure(4.8d). Conversely, the dark blue region denotes regions where the volume ratio monotonically decreases. The cause of this phenomenon will be explained later when we plot the strain response curve. The distribution of the volume ratio indicates that it can no longer be predicted solely from the sign of the Poynting effect. It is worth noting that the noise-like distribution in the light blue region may also be a result of our calculation. The range of applied shear strain is from 0 to 0.0005, with a constant gap of 0.00002. Thus, it is possible that the change in sign of $J - 1$ is not captured in this region.

We use the same sets of material parameters as in the previous subsection to investigate the actual curves. Figure (4.8c) plots $\lambda - 1$, which is identical to the curve under constant gap boundary conditions. This consistency arises from the fact that the expression of λ solely depends on γ. The derivation for this will be presented in the following subsection. Comparing Figure(4.8f) with the deformation gradient F_{yy} shown in Figure(4.5f), we observe that when the same shear strain is applied, the deformation gradient in the y direction decreases. On the other hand, the values of the deformation gradient in the x axis F_{xx} slightly increase. This implies that when the degree of freedom in the z axis is not constrained, the normal displacement in the y axis does not exhibit the same tendency to contract; instead, F_{zz} varies to compensate for the strain response.

Regarding the complex volume change pattern, it is evident that it is influenced by the boundary condition. Since the z-direction is not restrained, the volume change is influenced jointly by ξ and ϵ. Since $\xi - 1$ and $\epsilon - 1$ always have opposite signs, the volumetric change $\epsilon^2\xi - 1$ becomes more complex under smaller shear strains.

4.4.3. Comparison between two tensors

After studying the results obtained using the general tensor, we perform a comparison between the two tensors to assess how the change of boundary conditions affects the output. Given that the sign of the Poynting effect from both tensors exhibits an identical distribution, it might be expected that the differences between them may not be significant.

However, Figure(4.9) shows that the stress response behaves differently under constant gap boundary conditions. First, we let $\mathbf{F}_1$ denote the tensor used in equation (3.22) in Chapter 3 and $\mathbf{F}_g$ represent the general tensor introduced in this chapter. Because of the constant gap B.C., λ_2 in equation (3.22)

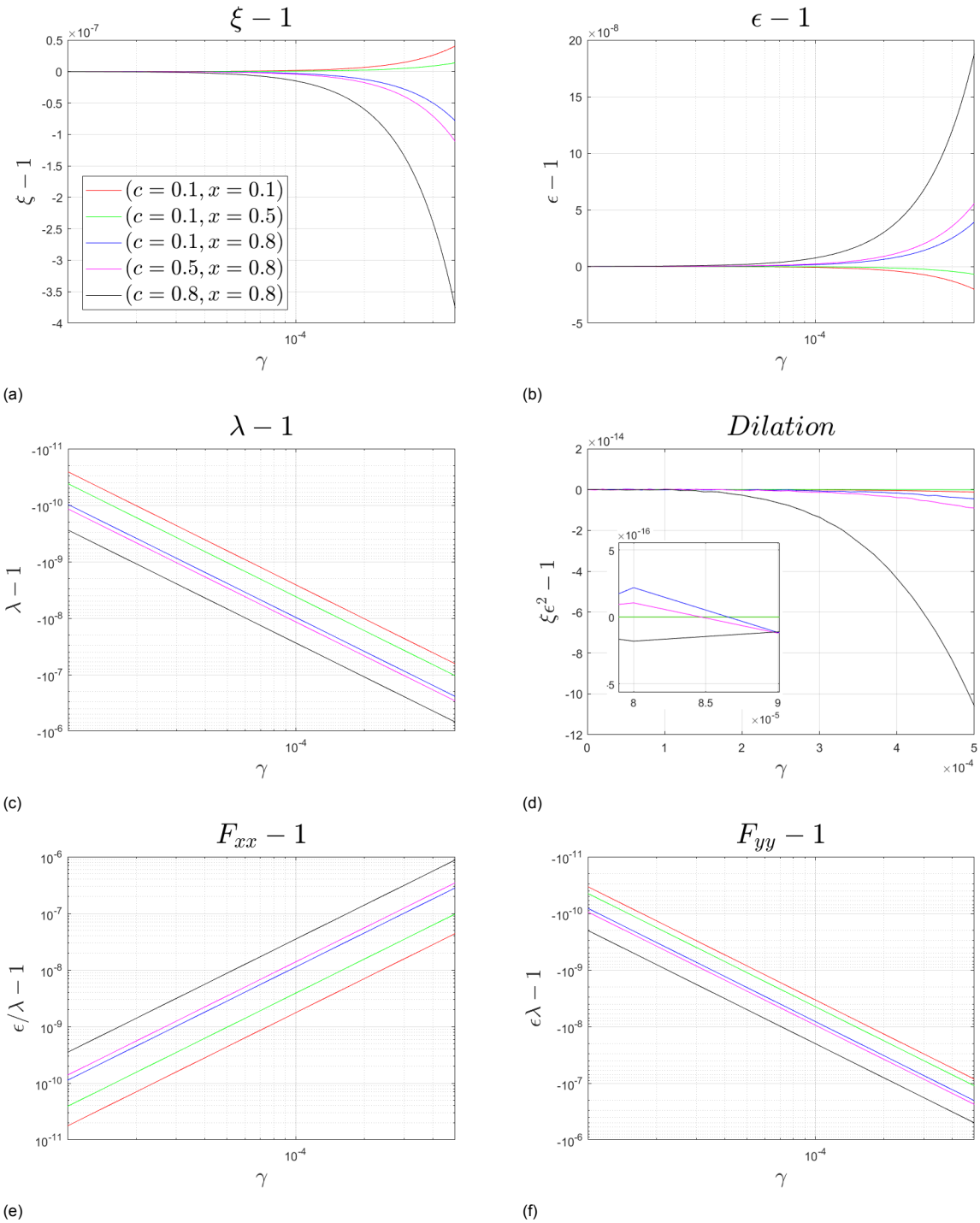

Figure 4.8: Five sets of material parameters have been selected to examine the response under $\kappa/\mu = 1000$. The strain response curves are illustrated in (a). In (b), (c), and (d), you can observe the curves for ϵ, λ, and dilation concerning the applied shear strain γ, respectively. The deformation gradient elements F_{xx} and F_{yy} are displayed in (e) and (f).

and ξ in equation (4.1) are assigned as one. λ and ϵ in equation (4.1) is solved by boundary conditions mentioned in (4.4).

All the results using $\mathbf{F}_1$ collapse on the same curve, which results from the fact that when the transverse normal strain λ_2 is set as a constant, the stress response is independent of the bulk moduli. On the other hand, the $(\epsilon - 1)$ term depends on the bulk moduli in equation (4.6), and therefore the results vary with respect to the choice of κ. For this specific set of material variables, the curve of $\mathbf{F}_1$ corresponds

to the case where the ratio is close to $\kappa/\mu = 100$ using general tensor $\mathbf{F}_g$. It is worth noting that for all cases, it shows a good agreement to the slope of -2, indicating that the γ^2 term is always dominant in the stress response when the shear strain is small enough.

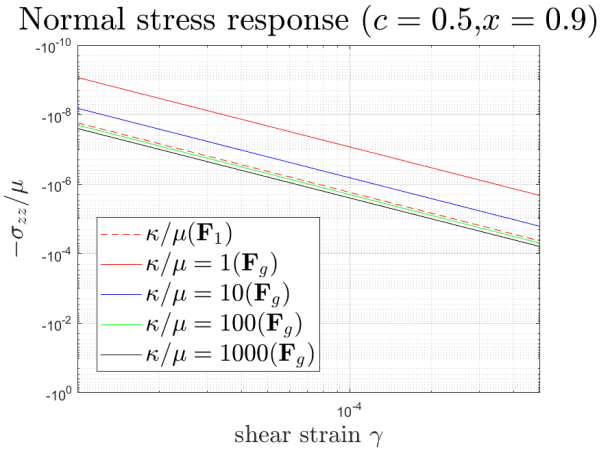

Figure 4.9: The dashed line represents the stress-strain curve of tensor $\mathbf{F}_1$, which is independent of compressibility. Using the general tensor $\mathbf{F}_g$ shows that when the material is more compressible, namely, smaller κ/μ ratio, the resulting normal stress is smaller as well.

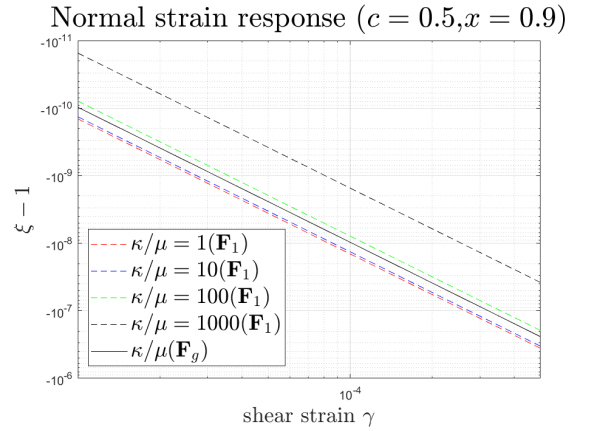

Figure 4.10: The normal strain response curves are shown in (a). The compressibility plays a role only when $\mathbf{F}_1$ is used. Using $\mathbf{F}_g$, the strain responses show no difference.

The comparison between the two tensors under constant normal stress boundary conditions yields a more surprising result. Figure (4.10) demonstrates that the change in Poisson's ratio does not affect the sign and magnitude of the normal strain response, indicating that it has no influence on the Poynting effect. This is in clear contrast to the phenomenon observed under constant gap boundary conditions. The reason why the strain response collapses onto the same curve will be explained in section (4.4.5).

In summary, the difference between the two tensors exhibits a completely different trend, which results from the different assumptions about boundary conditions. For $\mathbf{F}_1$, the stress in the x and y directions is not assumed to be zero because it is not presumed to be free. On the other hand, the general tensor captures a more practical situation because, in real-world scenarios, when simple shear is applied to a material, the x and y directions are often left unconstrained. These differences result in the compressibility having no effect on the Poynting effect for $\mathbf{F}_1$ under constant gap boundary conditions and for $\mathbf{F}_g$ under constant normal stress boundary conditions. These results are not intuitive and prompt us to conduct a simulation study to validate the findings, which will be presented in the next chapter.

4.4.4. The effect of compressibility - Constant gap

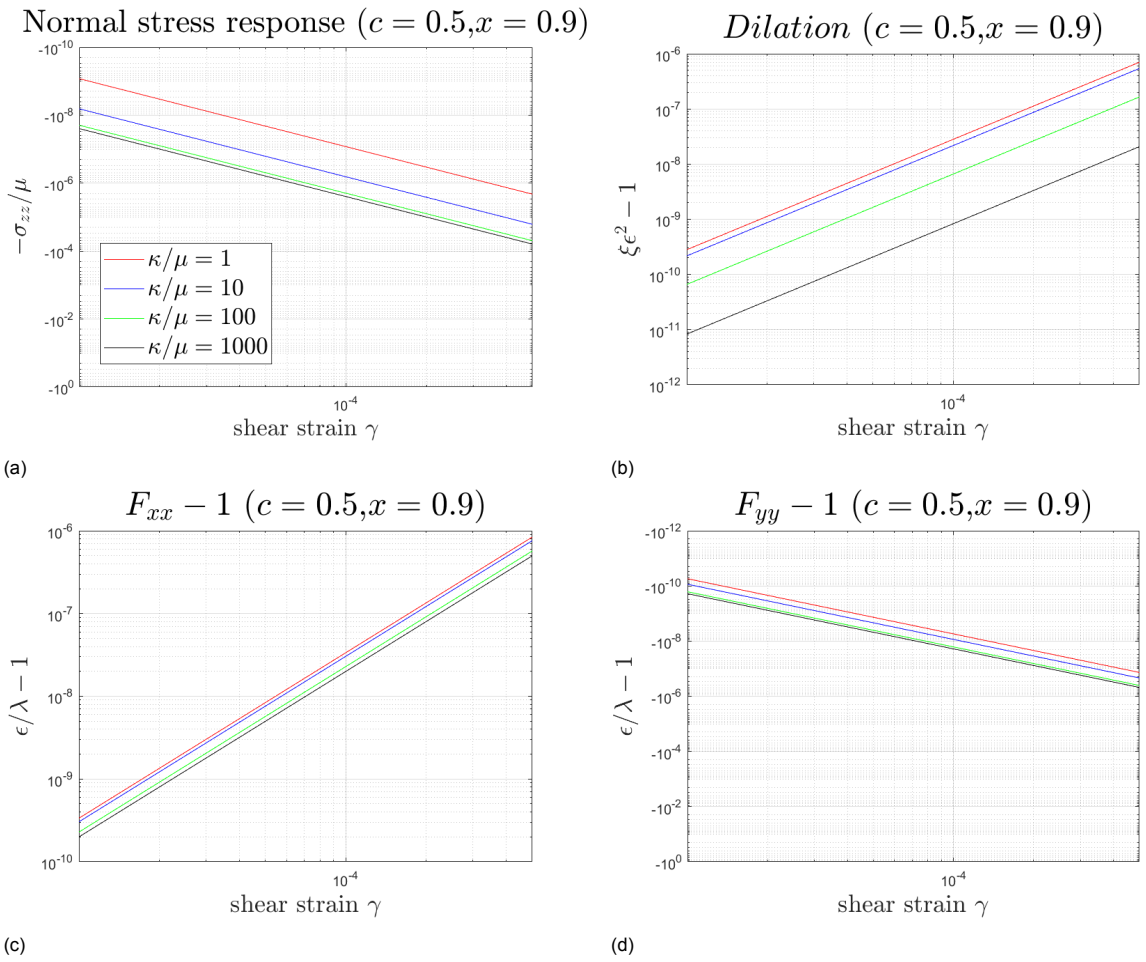

Figure 4.11: (a) The normal stress-strain curves show that the slope is 2, inferring that the γ^2 term dominates the stress responses. In the dilation plot (b), it is noticeable that the compressibility has a great influence. When material is more compressible, F_{xx} and F_{yy} both decrease, referring to a smaller expansion and a larger contraction on x and y direction, respectively.

In this subsection, we investigate the impact of compressibility while assuming constant gap boundary conditions. Initially, we vary the bulk modulus across a range from 1 to one thousand, applying a common ratio of 10. This variation in bulk modulus corresponds to distinct Poisson's ratios of ν = 0.125, 0.4516, 0.4950, and 0.4995. We select material parameters $(c, x) = (0.5, 0.9)$ for this analysis, as they exhibit a more pronounced response to the influence of compressibility.

We start with an examination of the stress response in the z-axis, denoted as $-\sigma_{zz}$, as illustrated in Figure (4.11b). Our results consistently align with the expectation that an increase in bulk modulus leads to a reduction in the magnitude of dilation.

Figure (4.11a) presents the non-dimensionalized normal stress response. It becomes evident that as the bulk modulus increases, the negative Poynting effect becomes more pronounced.

Turning our attention to Figure (4.11c) and (4.11d), we explore the effects of compressibility on the deformation gradient in the x and y directions. The response of F_{xx} reveals that an increase in bulk modulus encourages expansion along the x-direction. Simultaneously, it suppresses contraction along the y-direction.

4.4.5. The effect of compressibility - constant normal stress

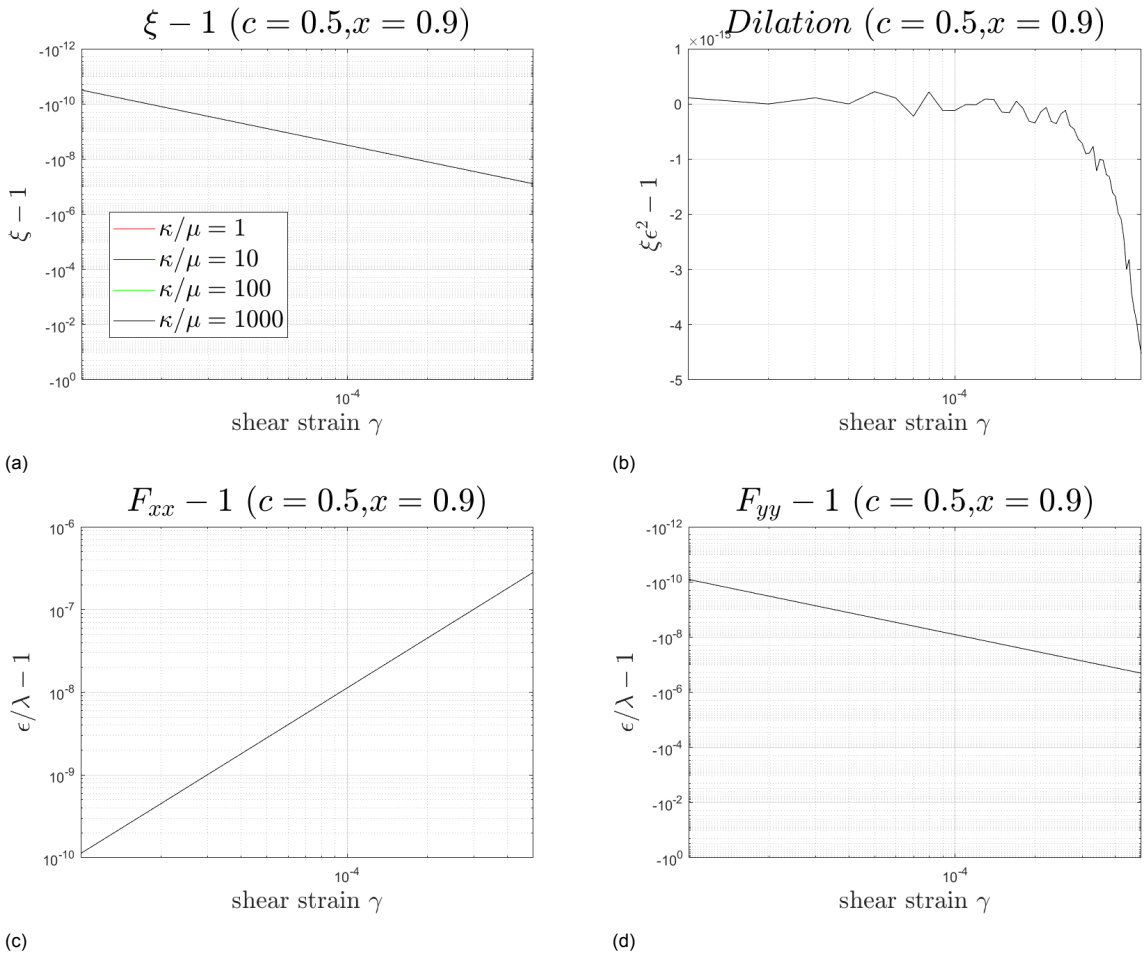

Figure 4.12: (a) The normal strain response curves show that the larger the ratio κ/μ, the larger the deformation gradient in the z direction. Also, when the material is more compressible, F_{xx} decreases, while F_{yy} stays on the same curve, implying that only the expansion in the x direction would be affected by the compressibility.

In this subsection, our focus shifts to investigating the impact of compressibility when the normal stress σ_{zz} is maintained at a constant level. We continue to employ the same bulk modulus as in the previous subsection.

Figure (4.12a) presents a rather unexpected outcome. It appears that the elongation in the z-direction remains consistent across various Poisson's ratios. This suggests that, in this specific scenario, compressibility does not play a significant role in determining the sign and magnitude of the Poynting effect. Instead, these aspects appear to be primarily influenced by the material parameters c and x.

This finding can be explained through analytical means. Firstly, by utilizing σ_{xx} and σ_{yy}, we can express ϵ and λ in terms of the other two variables, ξ and γ.

$$\lambda = \frac{-4 + 4x^4 + \gamma^2 + 2x^2\gamma^2 - c^2\pi^3(-1+x^2)^4(-4+\gamma^2)}{4(-1+x^2)(1+x^2+c^2\pi^3(-1+x^2)^3)},$$
$$\epsilon = \frac{-c^2\pi^3x^2(-1+x^2)^4\mu(\gamma^2-4\xi) + 9c\pi(-1+x^2)^4\kappa(-3+\xi) + x^2\mu((1-2x^2-2x^4)\gamma^2 + 4(-1+x^4)\xi)}{2(-1+x^2)(-9c\pi(-1+x^2)^3\kappa + 2c^2\pi^3x^2(-1+x^2)^3\mu + 2x^2(1+x^2)\mu)}. \tag{4.22}$$

The resulting normal stress σ_{zz} can be represented in an alternative form, as shown in equation (4.23). It becomes evident that when the normal stress is maintained at a constant value, specifically when it

is set to zero, the influence of compressibility becomes negligible.

$$\sigma_{zz} = -\frac{3x^2\kappa\mu(-6-\gamma^2+2x^2\gamma^2+c^2\pi^3(-1+x^2)^4(6+\gamma^2-6\xi)+2x^4(3+\gamma^2-3\xi)+6\xi)}{(-1+x^2)(-9c\pi(-1+x^2)^3\kappa+2c^2\pi^3x^2(-1+x^2)^3\mu+2x^2(1+x^2)\mu)}. \quad (4.23)$$

Figure (4.12b) depicts the volume change relative to the original volume, expressed as $\epsilon^2\xi - 1$. This measurement characterizes the system's dilation, which changes sign as shear strain increases. Dilational changes under constant normal stress boundary conditions are more intricate compared to those under constant gap boundary conditions. This complexity arises because dilation is influenced by two factors: ϵ and ξ. These two factors engage in a dynamic interplay, resulting in fluctuations in the curve when shear strain is smaller than 10^{-4}.

However, beyond $\gamma = 10^{-4}$, the effect of the z-direction deformation gradient ξ gradually becomes more dominant. As a consequence, the volume exhibits a clear decreasing trend under larger shear strains.

On the other hand, the deformation gradients in the x and y directions remain unaffected by compressibility, further supporting the notion that compressibility's impact is negligible in this specific scenario.

4.5. Strain stiffening and boundary condition

Continuing with the derivation presented in section (3.7), our objective is to assess how the boundary conditions impact the behavior of strain-stiffening, but this time using the general tensor. In order to describe the scenario where we maintain the normal stress σ_{zz} constant, we express the normal deformation gradient ξ as shown in equation (4.24).

$$\xi = \xi(\gamma, \epsilon, \lambda, \sigma_{zz}). \quad (4.24)$$

In this chapter, the derivation is similar to the one used in the previous chapter. The first derivative of the shear stress σ_{yz} with respect to shear strain γ under constant normal stress is expressed as shown in equation (4.25).

$$\left(\frac{\partial\sigma_{yz}}{\partial\gamma}\right)_{\sigma_{zz}} = \left(\frac{\partial\sigma_{yz}}{\partial\gamma}\right)_{\xi,\epsilon,\lambda} + \left(\frac{\partial\sigma_{yz}}{\partial\xi}\right)_{\gamma}\left(\frac{\partial\xi}{\partial\gamma}\right)_{\sigma_{zz}} \quad (4.25)$$

By applying the same method, we are able to obtain the second and the third derivative of the shear stress, as shown in equation (4.26) and (4.27).

$$\left(\frac{\partial^2\sigma_{yz}}{\partial\gamma^2}\right)_{\sigma_{zz}} = \left(\frac{\partial}{\partial\gamma}\left(\frac{\partial\sigma_{yz}}{\partial\xi}\right)_{\gamma}\right)_{\xi}\left(\frac{\partial\xi}{\partial\gamma}\right)_{\sigma_{zz}} + \left(\frac{\partial\xi}{\partial\gamma}\right)_{\sigma_{zz}}\left(\left(\frac{\partial^2\sigma_{yz}}{\partial\gamma^2}\right)_{\xi}\left(\frac{\partial\xi}{\partial\gamma}\right)_{\sigma_{zz}} + \frac{\partial}{\partial\xi}\left(\frac{\partial\sigma_{yz}}{\partial\gamma}\right)\right) + \left(\frac{\partial^2\sigma_{yz}}{\partial\gamma^2}\right)_{\xi} + \frac{\partial\sigma_{yz}}{\partial\xi}\frac{\partial^2\xi}{\partial\gamma^2} \quad (4.26)$$

$$\begin{aligned}\left(\frac{\partial^3\sigma_{yz}}{\partial\gamma^3}\right)_{\sigma_{zz}} = \left(\frac{\partial^3\sigma_{yz}}{\partial\gamma^3}\right)_{\xi} + \frac{\partial^3\sigma_{yz}}{\partial\xi^3}\left(\frac{\partial\xi}{\partial\gamma}\right)^3 + 3\left(\frac{\partial\xi}{\partial\gamma}\right)^2\frac{\partial}{\partial\gamma}\frac{\partial^2\sigma_{yz}}{\partial\xi^2} + 3\frac{\partial}{\partial\xi}\frac{\partial\sigma_{yz}}{\partial\gamma}\frac{\partial^2\xi}{\partial\gamma^2} \\ + 3\frac{\partial\xi}{\partial\gamma}\left(\frac{\partial^2\xi}{\partial\gamma^2}\frac{\partial^2\sigma_{yz}}{\partial\xi^2} + \frac{\partial}{\partial\xi}\frac{\partial^2\sigma_{yz}}{\partial\gamma^2}\right) + \frac{\partial\sigma_{yz}}{\partial\xi}\frac{\partial^3\xi}{\partial\gamma^3}\end{aligned} \quad (4.27)$$

Then, the difference in the strain hardening under two boundary conditions could be written as:

$$\begin{aligned}\left(\frac{\partial^3\sigma_{yz}}{\partial\gamma^3}\right)_{\sigma_{zz}} - \left(\frac{\partial^3\sigma_{yz}}{\partial\gamma^3}\right)_{\xi} = \frac{\partial^3\sigma_{yz}}{\partial\xi^3}\left(\frac{\partial\xi}{\partial\gamma}\right)^3 + 3\left(\frac{\partial\xi}{\partial\gamma}\right)^2\frac{\partial}{\partial\gamma}\frac{\partial^2\sigma_{yz}}{\partial\xi^2} + 3\frac{\partial}{\partial\xi}\frac{\partial\sigma_{yz}}{\partial\gamma}\frac{\partial^2\xi}{\partial\gamma^2} \\ + 3\frac{\partial\xi}{\partial\gamma}\left(\frac{\partial^2\xi}{\partial\gamma^2}\frac{\partial^2\sigma_{yz}}{\partial\xi^2} + \frac{\partial}{\partial\xi}\frac{\partial^2\sigma_{yz}}{\partial\gamma^2}\right) + \frac{\partial\sigma_{yz}}{\partial\xi}\frac{\partial^3\xi}{\partial\gamma^3}\end{aligned} \quad (4.28)$$

By applying the initial conditions, we can determine the difference in the strain-stiffening effect under the two boundary conditions, as expressed in equation (4.29). Interestingly, the expression is exactly

the same as the one we found in Chapter 3. Furthermore, Figure(4.13) illustrates that the response with respect to the bulk-to-shear ratio is nearly identical.

$$\left[\left(\frac{\partial^3\sigma_{xy}}{\partial\gamma^3}\right)_{\sigma_{yy}}-\left(\frac{\partial^3\sigma_{xy}}{\partial\gamma^3}\right)_{\xi}\right]_{\gamma=0,\xi=1,\epsilon=1,\lambda=1}=-\frac{3\Lambda_1\chi}{\lambda_L}=\frac{3\chi^2}{\lambda_L}. \tag{4.29}$$

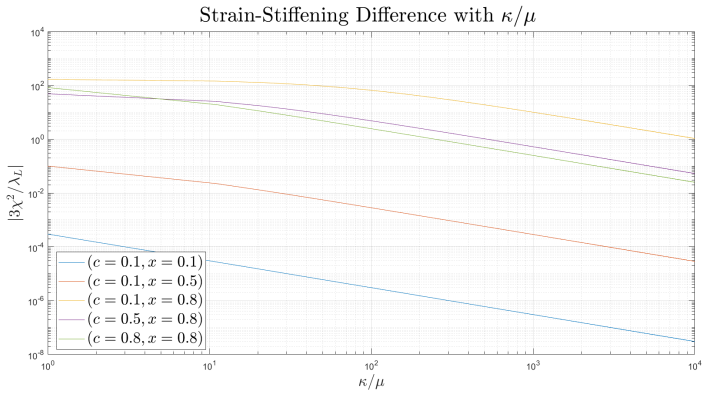

Figure 4.13: The strain stiffening effect performs differently under two boundary conditions. The difference is dependent on the compressibility κ/μ. The plot shows that different material sets may perform differently to the effect of compressibility. However, the slope always reaches $1/(\kappa/\mu)$ at a large ratio.

5

Simulation

In this chapter, our goal is to validate the results obtained in the previous chapters using the commercial software COMSOL. COMSOL is a Finite-element based software known for its capability to solve solid mechanics problems. We selected it due to its flexibility and user-friendly interface. The term ”flexibility” in this context refers to the ease of implementing user-defined functions, which is one of our main objectives because we need to define a hyperelastic materials model in the software.

Our main focus is on the Poynting effect and how it varies with different Poisson's ratios. Specifically, for the constant gap boundary condition, we aim to determine whether an increase in Poisson's ratio corresponds to an increase in the magnitude of the normal stress σ_{zz}. On the other hand, for the constant normal stress boundary condition, we expect that an increase in Poisson's ratio will have no effect on the Poynting effect.

5.1. Simple shear in cylinder

In this chapter, our simulation will involve the application of simple shear to a cylindrical object. Therefore, in this section, we revisit the concept of simple shear applied to a cylinder. The use of a cylindrical geometry is common when analyzing the Poynting effect because soft matter is often placed inside a rheometer during experiments. The strain tensor for simple shear in a cylindrical geometry can be expressed as shown in equation (5.1).

There are two main reasons why we chose the cylindrical geometry for our simulation model. First, it is a relatively simple geometry, making it easier for us to compare with the analytical solution. Second, soft matter often exhibits viscoelastic or thixotropic characteristics, and the parallel plate geometry is typically used to control oscillatory shear and measure time-dependent behaviors. Therefore, even though we are not specifically studying viscoelasticity and thixotropy in this research, we chose the cylindrical geometry to make it adaptable for potential future studies. However, it's important to note that the coordinate system becomes cylindrical, corresponding to the variables r, θ, and $z.\theta$, and z.

$$\mathbf{F} = \begin{bmatrix} \epsilon/\lambda & 0 & 0 \\ 0 & \epsilon\lambda & \gamma/(\epsilon\lambda) \\ 0 & 0 & \xi \end{bmatrix} \tag{5.1}$$

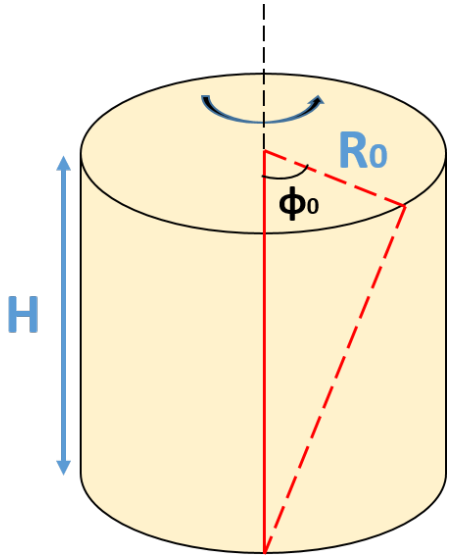

Figure 5.1: The illustration depicts the process of applying simple shear to a cylinder. The bottom of the cylinder is fixed, while the upper plane is rotated by an angle of rotation ϕ_0. It is assumed that this angle decreases linearly as you move towards the bottom of the cylinder along the z-axis. Additionally, the angle remains constant on each cross-section of the cylinder. The resulting shear strain acts on the $\theta - z$ plane of the cylinder.

To provide a clearer visualization of the cylinder's deformation, we have illustrated the simple shear of the cylinder in Figure (5.1). In this illustration, the cylinder has a radius denoted by R and a gap denoted by H. The angle of rotation at the upper plane is represented by ϕ_0. From the figure, several key characteristics can be observed: (1) The angle of rotation ϕ decreases linearly with the distance from the upper plane along the z-axis. (2) On each cross-section at a fixed z-coordinate, the angle of rotation remains constant. (3) The displacement along the θ-direction is related to the radial coordinate, given by $u_\theta = r\phi$. Here ϕ denotes the angle of rotation on each cross-section at fixed z, which should not be confused with θ denoting the coordinate of a point. Due to these characteristics, the shear strain γ can be expressed as shown in equation (5.2). This equation highlights that the shear strain γ is independent of the z-coordinate and solely depends on the radial coordinate.

$$\gamma(r) = \frac{r\phi_0}{H} \tag{5.2}$$

Due to the characteristic of the shear strain distribution in the cylinder, it is necessary to perform additional calculations to compare theoretical results with the cylindrical simulation. In our theoretical analysis, we assume that the entire geometry undergoes identical deformation, making a single cell representative. However, in this chapter, we realize that the assigned γ_0 is only accurate for $r = R_0$.

As we have established in previous chapters, the normal stress response is mainly determined by the γ^2 term. Utilizing the linear relationship between γ and r as described in equation (5.2), we can derive an approximation (5.3) to calculate the stress at $r < R_0$. This approximation takes into account the local variation of γ within the cylinder.

$$\sigma_{zz}(r) = \frac{r^2}{R_0^2}\sigma_{zz,R} \tag{5.3}$$

As a result of this approach, we can approximate the averaged normal stress $\overline{\sigma_{zz}}$ as shown in equation (5.4). In this equation, $\sigma_{zz,R}$ represents the normal stress at $r = R_0$, which is a constant for a given γ_0. This calculation implies that for a given γ_0, we can predict the average normal stress to be half of the results obtained by directly solving the equations with $\gamma = \gamma_0$. This approximation helps us account for the local variation of shear strain within the cylinder.

$$\begin{aligned}\overline{\sigma_{zz}} &= \frac{1}{\pi R_0^2}\int_0^{R_0} \frac{r^2}{R_0^2}\sigma_{zz,R} 2\pi r dr \\ &= \frac{\sigma_{zz,R}}{2}.\end{aligned} \tag{5.4}$$

In this scenario where the normal stress is held constant while the cylinder is free to elongate along the z-axis, reconciling the conditions becomes more complex due to the cylindrical geometry. The shear strain γ varies with the radial coordinates, implying that the z-displacement w should also vary with the radial coordinate. However, the upper plane of the cylinder is assumed to deform as a rigid body, which suggests that the displacement should be constant regardless of radial displacement.

To address these conflicting conditions simultaneously, we introduce two key assumptions: (1) The constant normal stress boundary conditions are satisfied only in an average sense, meaning an alternative condition $\overline{\sigma_{zz}} = 0$ is applied. (2) The transverse displacement gradient ξ is a constant, denoted as ξ_c, at any point within the cylinder.

By using equation (4.23), we can establish the relationship between ξ_c and the original value ξ_0. The equation takes the following form:

$$\sigma_{zz} = C_1\gamma^2 + C2(\xi - 1). \tag{5.5}$$

And the original solution is

$$\xi_0 - 1 = \frac{-C_1}{C_2}\gamma_0^2. \tag{5.6}$$

Then we calculate the solution for the cylinder. Equation (5.5) is integrated with respect to γ over 0 to γ_0 and the integration should result in zero. ξ is replaced by a constant ξ_c.

$$\begin{aligned} &\overline{\sigma_{zz}} = \frac{1}{\pi R_0^2}\int_0^{R_0}(C_1\gamma^2 + C2(\xi_c - 1))2\pi r dr = 0, \\ \Rightarrow &\int_0^{\gamma_0}(C_1\gamma^2 + C2(\xi_c - 1))\gamma d\gamma = 0, \\ \Rightarrow &\xi_c - 1 = \frac{-C_1}{2C_2}\gamma_0^2. \end{aligned} \tag{5.7}$$

Therefore, we could predict that the elongation of the cylinder is half of the value of the one if the object has a universal deformation gradient.

$$\xi_c - 1 = \frac{\xi_0 - 1}{2} \tag{5.8}$$

Given the cylindrical geometry, the original analytical results require further treatment. We begin with the constant gap boundary condition and make several assumptions for the analysis. Firstly, we consider the local volume ratio as a function solely of the radial coordinate, with no dependence on the transverse coordinate. Additionally, we assume that the average volume ratio can be determined by averaging over the entire volume.

To initiate the derivation, we utilize the expression for ϵ as shown in equation (4.22). By applying the boundary condition $\xi = 1$, this expression can be further simplified as shown in equation (5.9).

$$\epsilon - 1 = C_3\gamma^2. \tag{5.9}$$

The volume ratio under constant gap boundary condition is known to be calculated by ϵ^2 and therefore the average of the volume ratio could be formulated as:

$$\bar{J} = \frac{1}{\pi R_0^2 H}\int_0^{R_0}(C_3\gamma^2 + 1)^2 2\pi r H dr \tag{5.10}$$

Using the relation (5.2), the expression of the average volume ratio becomes

$$\bar{J} = 1 + \frac{C_3^2}{3}\gamma_0^4 + C_3\gamma_0. \tag{5.11}$$

Assuming that the original analytical solution has the relation $\epsilon_0 - 1 = C_3\gamma_0^2$, the average volume ratio of the cylinder could relate to the original analytical solution by equation (5.12). Note that since ϵ_0 is

dependent on the compressibility, therefore the average volume ratio is also expected to be affected by the change of Poisson's ratio.

$$\bar{J} - 1 = \frac{1}{3}(\epsilon_0 - 1)^2 + (\epsilon_0 - 1). \tag{5.12}$$

Then, we derive the volume ratio under the constant normal stress relation. The volume ratio becomes more complicated when ξ is involved. First, we start with equation (4.22), only this time the z deformation gradient ξ is not one, instead, it is a constant ξ_c. The expression for ϵ is written as equation (5.13). The expression of the local volume ratio is known as $\epsilon^2\xi$ in this case. The expression for the average volume ratio could thus be written as equation (5.14).

$$\epsilon - 1 = C_3\gamma^2 + C_4\xi_c. \tag{5.13}$$

$$\bar{J} = \frac{1}{\pi R_0^2 H}\int_0^{R_0} \xi_c(C_3\gamma^2 + C_4(\xi_c - 1) + 1)^2 2\pi r H dr \tag{5.14}$$

Using the equation (5.2) again, we obtain the following relation.

$$\bar{J} = \xi_c\left(\frac{C_3^2}{3}\gamma_0^4 + C_4^2\left(\xi_c - 1\right)^2 + 1 + C_3C_4\gamma_0^2\left(\xi_c - 1\right) + C_3\gamma_0^2 + 2C_4\left(\xi_c - 1\right)\right). \tag{5.15}$$

The expression is quite complex, and we have not found a straightforward way to relate it directly to the original solution ϵ_0. However, we can still transform ξ_c back to ξ_0 using the relation shown in equation (5.8).

$$\bar{J} - 1 = \left(\frac{\xi_0 + 1}{2}\right)\left(\frac{C_3^2}{3}\gamma_0^4 + C_4^2\left(\frac{\xi_0 - 1}{2}\right)^2 + C_3C_4\gamma_0^2\left(\frac{\xi_0 - 1}{2}\right) + C_3\gamma_0^2 + 2C_4\left(\frac{\xi_0 - 1}{2}\right)\right) + \left(\frac{\xi_0 - 1}{2}\right). \tag{5.16}$$

These derivations would be used for comparison with the simulation results.

5.2. Settings

In this section, we begin setting up the finite element model (FEM) with a cylindrical geometry that has a high gap-to-radius ratio (H/R), a configuration that has been used in previous studies [68]. The cylinder's centerline aligns with the z-axis, and the chosen ratio for this research is set to 12, with a radius of 0.01 meters. To achieve a highly refined mesh, we utilize a predefined unstructured quadrilateral mesh type available in the general physics menu. The meshing process initiates from one side of the cylinder, and the "swept" function is applied to extend the mesh from the source face to cover the entire domain. The geometry and mesh are depicted in Figure (5.2).

In the numerical model setup, we also focus on the effect of compressibility on the Poynting effect. To achieve this, we utilize a blank material that allows us to specify the bulk and shear modulus of an arbitrary material. We then replace the linear elastic material model with a hyperelastic material model to incorporate the strain-stiffening effect. The near-incompressible mode allows us to divide the material strain energy function into isochoric and volumetric parts. We represent the isochoric strain invariants $\tilde{I_1}$ and $\tilde{I_2}$ as the variables solid.I1CIel and solid.I2CIel. Additionally, the elastic volumetric deformation J in the volumetric energy function is expressed as solid.Jel. We assign an arbitrary value as the material density.

Regarding restraints in the model, a rigid connector is applied to the bottom plane of the cylinder, and prescribed displacements are assumed, effectively fixing this plane with $(u, v, w) = (0, 0, 0)$, where u, v, and w denote the displacements in the x, y, and z-directions, respectively. It is important to note that the connector is set to a rigid type, functioning as a virtual rigid object to prevent internal deformations. The boundary conditions on the bottom plane remain unchanged regardless of the chosen boundary conditions.

For the upper plane, the setup differs based on whether the constant gap or constant normal stress

boundary conditions are applied. In both cases, a rigid connector of a rigid connection type is used. The prescribed angle of rotation ϕ_0 is assigned, with the center of rotation set as the center of the upper plane. ϕ_0 represents the largest shear strain on the cylinder's ring at $r = R_0$. We apply a range of small but finite shear strains, typically ranging from 10^{-5} to 5×10^{-4}.

For the constant gap boundary condition, the prescribed displacements of the center of rotation in the x and y-directions (u, v) are set to zero, and the z-direction displacement w is also set to zero to prevent the upper plane from moving.

In the case of the constant normal stress boundary condition, we cancel the prescribed z-direction displacement to allow the cylinder to elongate along the z-axis. This setup enables the model to satisfy several assumptions: first, it ensures that the cross-sections move rigidly along the z-axis, and second, the radius remains a straight line after deformation.

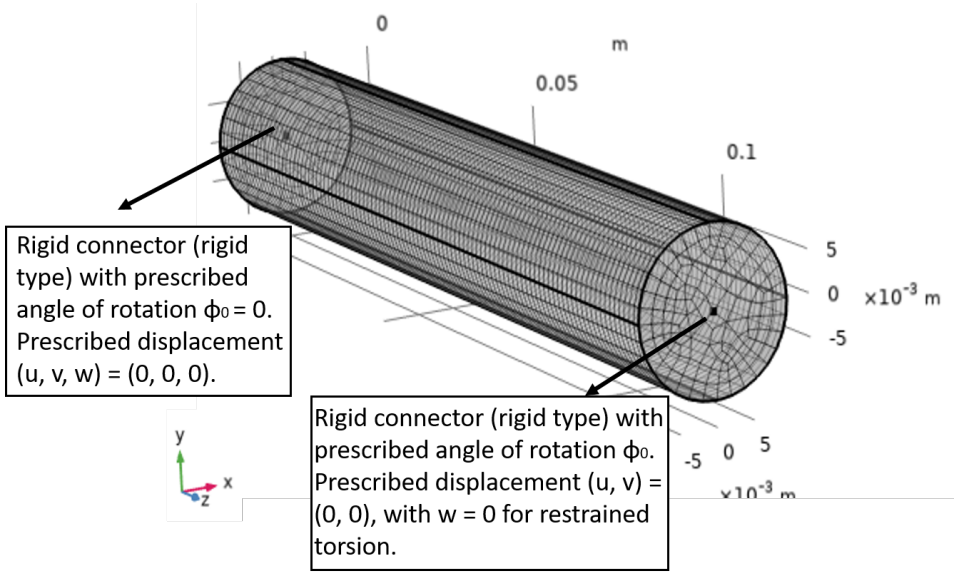

Figure 5.2: An illustration of the cylindrical geometry is shown here. In this research, the gap-to-radius ratio is set to 12. Rigid connectors are applied to both ends of the cylinder, with one end fixed and the other end assigned a prescribed angle of rotation.

5.3. Constant Gap Boundary Conditions

Under the normal gap boundary conditions, the displacement on the upper plane $w(x, y, z = H)$ is set to zero. For this simulation, two sets of material parameters are chosen to investigate the presence of positive and negative Poynting effects, as well as the influence of compressibility. We mostly focus on the normal stress response along the z-axis, σ_{zz}, and the average volume change, $\bar{J} - 1$.

To calculate the average normal stress $\overline{\sigma_{zz}}$, the average of the normal stress on the upper plane is taken and then normalized by the shear modulus μ for non-dimensionalization. The average volume change $\bar{J} - 1$ is determined by taking the volume average over the entire domain. For comparison, the analytical solutions for the average normal stress $-\overline{\sigma_{zz}}$ and the average volume change $\bar{J} - 1$ are computed using equations (5.4) and (5.12).

In Figure (5.3a) and its zoomed-in version (5.3b), it is evident that when the material parameters are set to $(c = 0.1, x = 0.5)$, both the analytical solution (solid lines) and the FEM results (dotted lines) exhibit a positive Poynting effect. The two results closely match, making it challenging to distinguish between them. The stress response follows a linear trend in the log-log diagram, indicating that the γ^2 term plays a significant role in the normal stress response in the FEM.

Upon closer examination, it becomes apparent that the general tensor $\mathbf{F}_g$ aligns better with the simu-

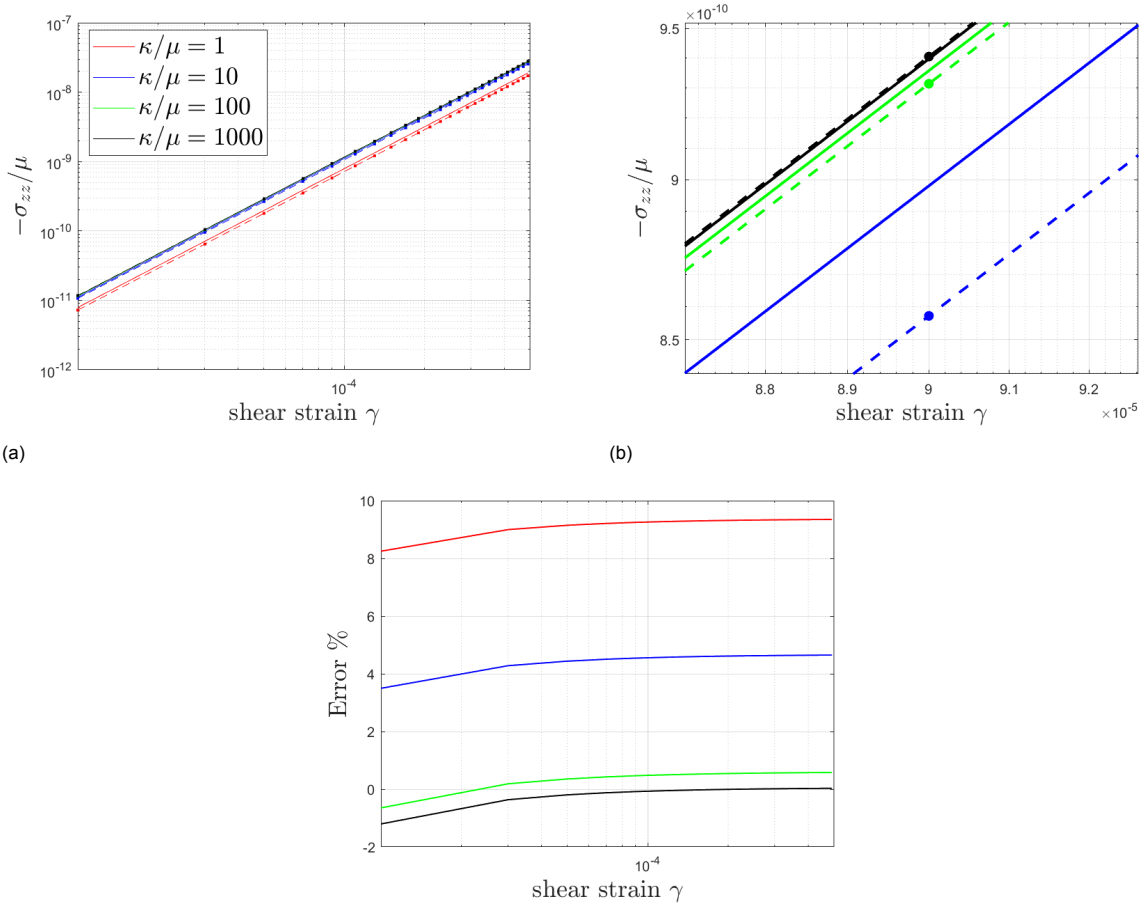

(a) (b)

(c)

Figure 5.3: For material variables ($c = 0.1, x = 0.5$), the normal stress response under constant gap boundary condition curves in (a) shows positive Poynting effect. The FEM solutions and the analytical solution are plotted by dotted lines and solid lines, respectively. A zoom-in figure in (b) shows that the FEM and analytical solution shows the same trend that a larger Poisson's ratio corresponds to a larger stress. The error between the FEM and the analytical solution is shown in (c).

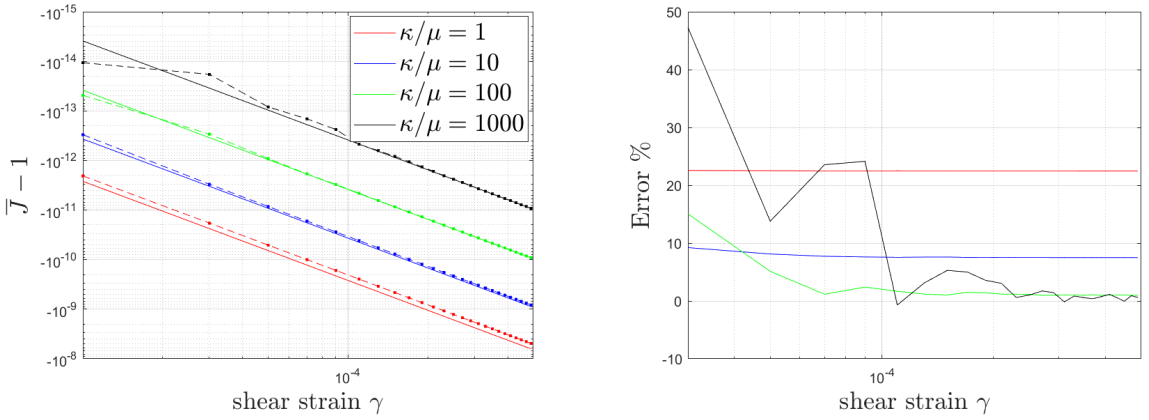

(a) (b)

Figure 5.4: For material variables ($c = 0.1, x = 0.5$), (a) the FEM solution and the analytical solution show a good agreement on the change of average volume ratio $\overline{J} - 1$. The error of each case is shown in (b).

lation results, showing that as the material becomes more compressible, the magnitude of the normal stress decreases accordingly. The trend of normal stress under the influence of compressibility differs

between the general tensor $\mathbf{F}_g$ and the simple tensor $\mathbf{F}_1$. In the previous chapter, it was established that the magnitude of the stress is dependent on the Poisson's ratio when the general tensor $\mathbf{F}_g$ is applied, but not when using the simple tensor $\mathbf{F}_1$, even though the sign of the Poynting effect remains the same for both tensors.

Lastly, we examine the error between the simulation and the analytical solution with the general tensor $\mathbf{F}_g$. This error is computed as $e = 1 - \text{FEM/Analytical}$. In Figure (5.3c), it is evident that the error is generally below 10%, and it decreases significantly with an increase in the bulk-to-shear modulus ratio, which corresponds to a higher Poisson's ratio. This phenomenon may be due to the fact that, in the FEM model, the nearly incompressible mode is chosen. In Comsol, even when selecting the nearly incompressible mode, it is necessary to specify the values for the bulk and shear modulus and incorporate them into the user-defined material model. Therefore, higher Poisson's ratios are more suitable for this model, leading to better consistency with the analytical solution.

Figure (5.5a) to (5.5c) show the results when using material parameters $(c = 0.1, x = 0.8)$, which results in a negative Poynting effect. The FEM and analytical solution using $\mathbf{F}_g$ also exhibit the same trend under the influence of compressibility, with a larger bulk-to-shear modulus ratio corresponding to a larger magnitude of normal stress. The error plots in Figure (5.5c) also demonstrate that higher Poisson's ratios result in smaller errors.

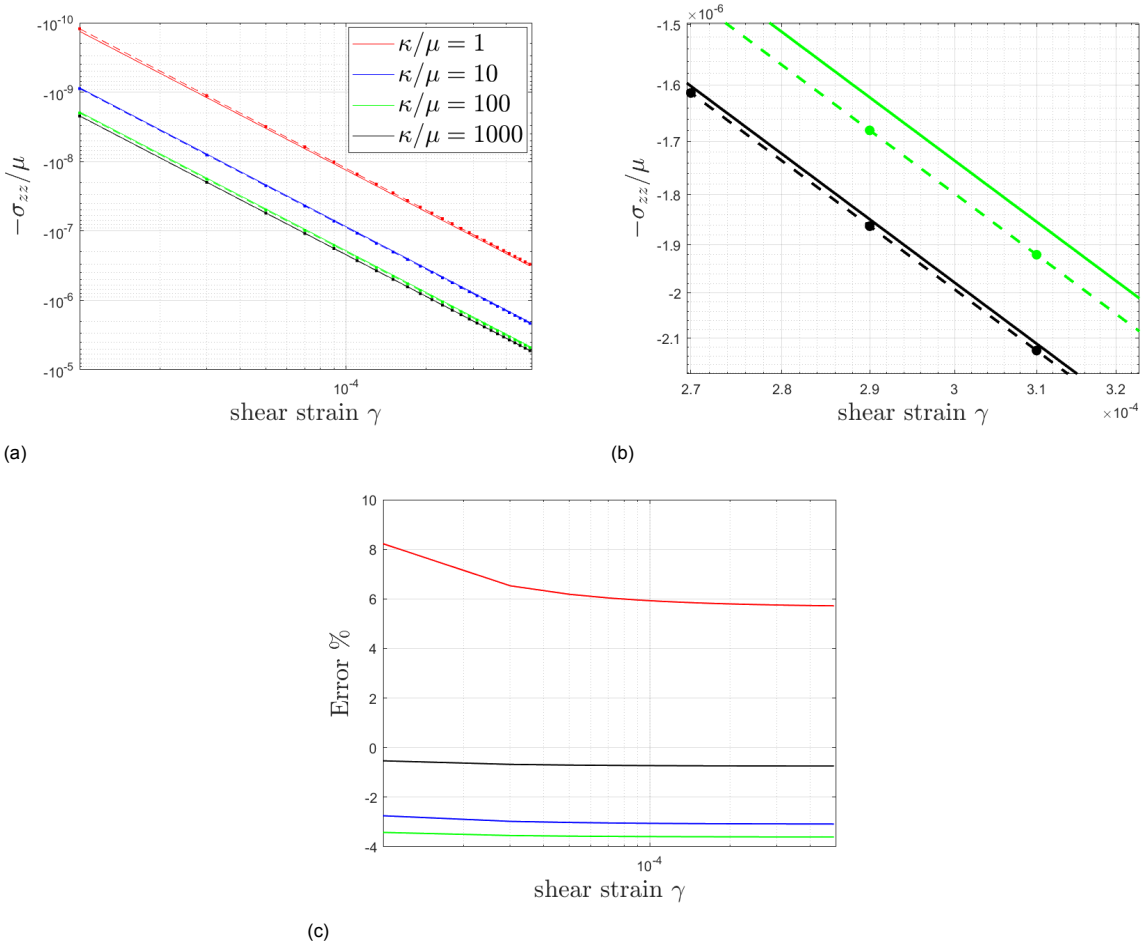

Figure 5.5: For material variables $(c = 0.1, x = 0.8)$, the normal stress response curves in (a) shows negative Poynting effect. The FEM solutions and the analytical solution are plotted by dotted lines and solid lines, respectively. A zoom-in figure in (b) shows that the FEM and analytical solution shows the same trend that a larger Poisson's ratio corresponds to a larger stress response. The error between the FEM and the analytical solution is shown in (c).

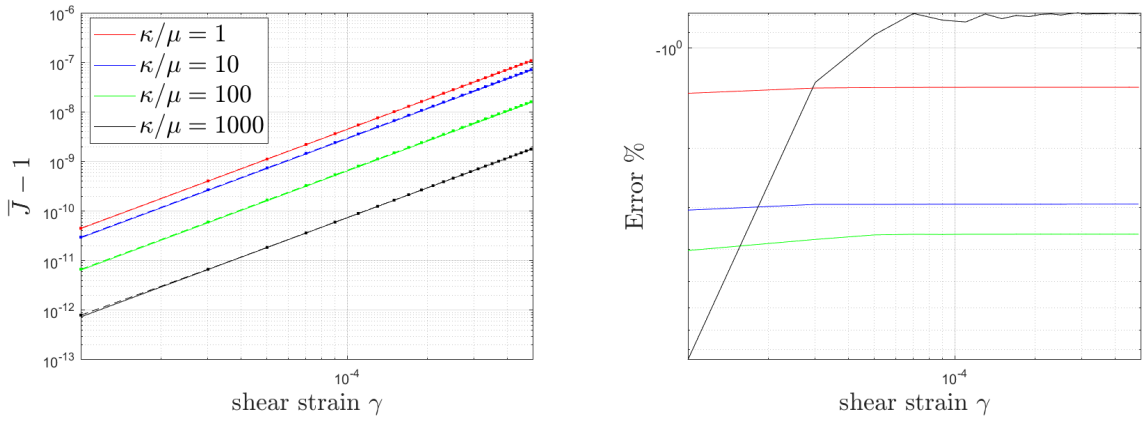

(a) (b)

Figure 5.6: For material variables ($c = 0.1, x = 0.8$),(a) the FEM solution and the analytical solution show a good agreement on the change of average volume ratio $\bar{J} - 1$. The error of each case is shown in (b).

The change in volume ratio $\bar{J} - 1$ is shown in Figures (5.4a) and (5.6a). These results align with the analytical solution, demonstrating that the positive Poynting effect is accompanied by a decrease in volume, while the negative Poynting effect is associated with an increase in volume. The curves exhibit a straight-line behavior that monotonically increases or decreases in the log-log plots, consistent with the derivation in equation (5.12), which relates the volume change to the shear strain through a power-law relationship. Furthermore, the increase in Poisson's ratio reduces the magnitude of the volume change in both cases.

The error plots in Figures (5.4b) and (5.6b) also provide interesting insights. The errors generally remain below 10%, which is regarded acceptable given that $\bar{J} - 1$ is generally small. It is noteworthy that in both scenarios, the case with the highest Poisson's ratio (black lines) exhibits large errors at low shear strains γ, followed by a significant decrease in errors as γ increases. One possible explanation for this behavior is that the analytical solution yields extremely small values of $\bar{J} - 1$, making small differences result in large relative errors at low shear strains.

5.4. Constant Normal stress Boundary Conditions

Under constant normal stress boundary conditions, we investigate the elongation of the cylinder and the volume ratio using the same material parameter sets as chosen in the previous section, allowing us to explore both positive and negative Poynting effects.

While the assumption that ξ is uniform throughout the entire geometry suggests that calculating the average of ξ at the upper plane of the cylinder would be intuitive, Figure (5.7) illustrates that the distribution of $(\xi - 1)$ displays significant local variations near the boundaries. This figure compiles data from the center of each cross-section along the z-axis. Notably, at both ends of the cylinder, the magnitude of $(\xi - 1)$ decreases sharply. Contrarily, in the middle of the cylinder, $(\xi - 1)$ forms a flat, straight line, providing a more accurate representation of the cylinder's elongation.

To account for these local effects, we choose to analyze the displacement of the upper plane instead. The upper plane moves as a rigid body, and its displacement is equivalent to the summation of local deformations along the z-axis. By doing so, we aim to mitigate the local effects near both ends of the cylinder. Consequently, the simulation results are calculated as the average displacement of the upper plane over the gap of the cylinder, represented as avg(w)/H. The averaged volume ratio is once again determined through the volumetric average across the entire domain.

For the sake of comparison, we compute the analytical solution for the average displacement $\bar{\xi} - 1$ and the average volume change $\bar{J} - 1$ using equations (5.8) and (5.16).

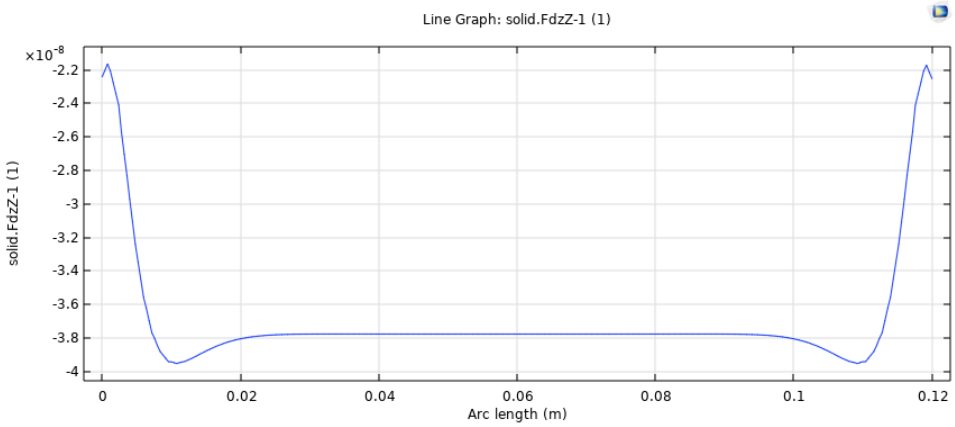

Figure 5.7: The distribution of the z-direction deformation gradient is plotted against the z-coordinate and it presents a strong boundary effect at two ends of the cylinder. The middle part of the cylinder shows a stable flat curve instead, which is more representative when calculating the elongation of the cylinder.

Figure (5.8a) illustrates the positive Poynting effect using material parameters $(c = 0.1, x = 0.5)$. The FEM results (dotted lines) show that the change in deformation gradient $(\xi - 1)$ varies with the choice of Poisson's ratio, which differs from the analytical solution obtained in previous chapter (solid line). A closer examination in Figure (5.8b) suggests that the analytical solution closely matches the case where $\kappa/\mu = 1$. All the $(\xi - 1)$ results display a linear curve in the log-log plot, indicating significant influence from the γ^2 term, in agreement with the derivation in Equation (5.7). The error plot reveals that, even though the FEM outputs exhibit dependence on Poisson's ratio, the error typically remains below 5%. While the fact that the FEM outputs show compressibility dependence may raise questions about the validity of tensor $\mathbf{F}_g$, it would be premature to conclude that tensor $\mathbf{F}_1$ captures this characteristic while $\mathbf{F}_g$ does not.

Figure (5.10a) depicts the negative Poynting effect when material parameters $(c = 0.1, x = 0.8)$ are applied. The FEM results also display a quadratic characteristic, with the only difference being they are negative. A closer examination shows that the analytical solution almost overlaps with the FEM result where $\kappa/\mu = 1000$. The error plot also indicates a good correspondence between the two curves. Except for the case of low Poisson's ratio (red line), the errors are also below 5%.

Whether $\mathbf{F}_1$ captures the dependence on compressibility of the FEM model needs to be determined based on the overall trend. When $\mathbf{F}_1$ is applied, it reveals that increasing incompressibility corresponds to a smaller change in deformation gradient ξ in Figure (4.10). However, the FEM model does not align with this trend in Figure (5.8b). In this case, the most compressible scenario (red dotted line) exhibits the largest deformation, while the second most compressible case (blue dotted line) displays the smallest deformation. On the other hand, in Figure (5.10b), the largest change in ξ corresponds to the third most compressible case (green dotted line), while the smallest change in $(\xi - 1)$ corresponds to the most compressible scenario (red dotted line).

Upon analyzing these two figures, it becomes evident that tensor $\mathbf{F}_1$ does not capture the dependence on compressibility. Furthermore, it is argued that the errors actually stem from geometric factors. One contributing factor is the random distribution of the magnitude of $(\xi - 1)$ concerning compressibility. There is no noticeable trend that would allow us to conclude how compressibility influences the Poynting effect performance in the FEM model.

Finally, we examine the volume ratio of the cylinder. In both cases, the FEM model indicates that the model expands. However, the comparison between the FEM model and the analytical model is not informative due to significant deviations between them.

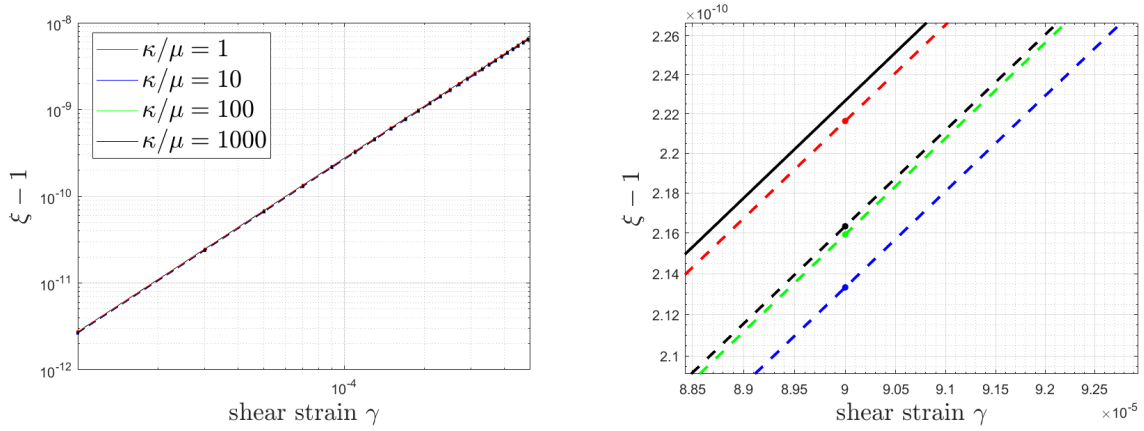

(a) (b)

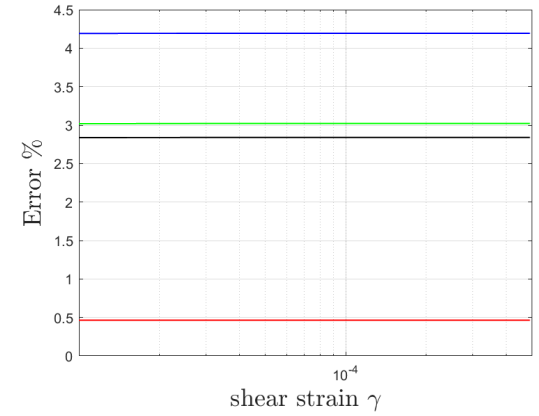

(c)

Figure 5.8: For material variables ($c = 0.1, x = 0.5$), the normal strain response curves show positive Poynting effect in (a). The analytical solutions show no dependence on compressibility. However, the FEM solution shows a variation in strain responses, as shown in the zoom-in figure (b). The errors in (c) are typically below 5%.

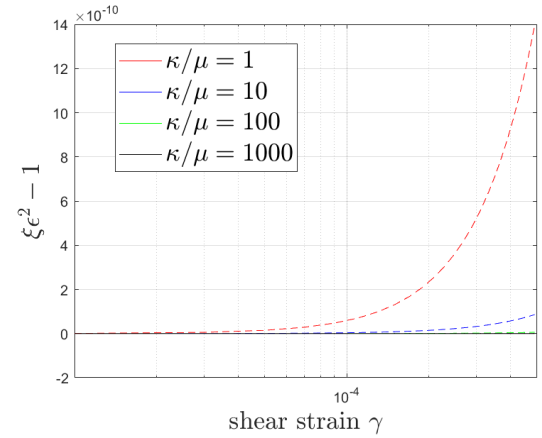

Figure 5.9: For material variables ($c = 0.1, x = 0.5$), the change of volume ratio $\bar{J} - 1$ shows expansion of the system. The compressibility plays a role in the volume change, where an increase in Poinsson's ratio results in a smaller volume change.

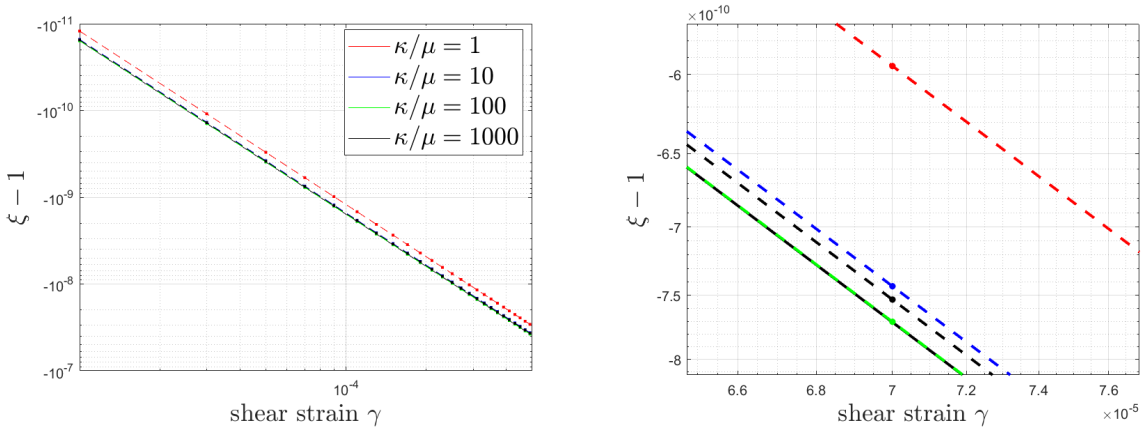

(a) (b)

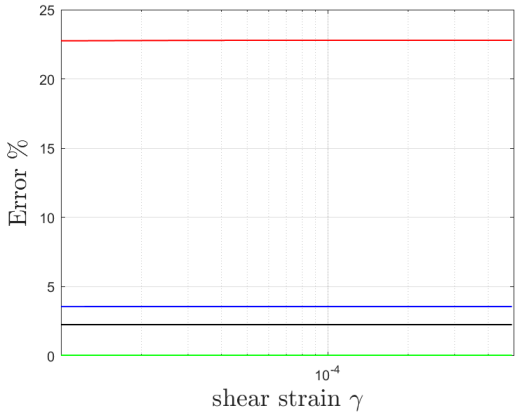

(c)

Figure 5.10: For material variables $(c = 0.1, x = 0.8)$, the normal strain response curves show a negative Poynting effect in (a). Even though for the case of $\kappa/\mu = 1$, the deviation from the analytical solution is large, as shown in (b). However, for the rest of the cases, the errors in (c) are typically below 5%.

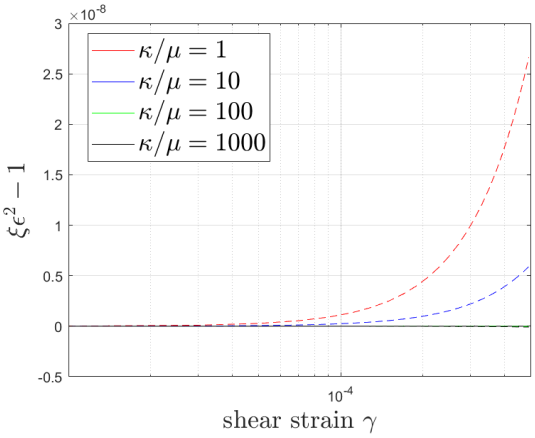

Figure 5.11: For material variables $(c = 0.1, x = 0.8)$,

5.5. Moment response

In the preceding sections, we have examined the difference between the normal stress and strain responses in numerical and analytical solutions. Using the same method, the shear stress response could also be derived. Nevertheless, rather than focusing on comparing shear stress responses, our

primary interest lies in understanding the associated moment applied to the cylinder.

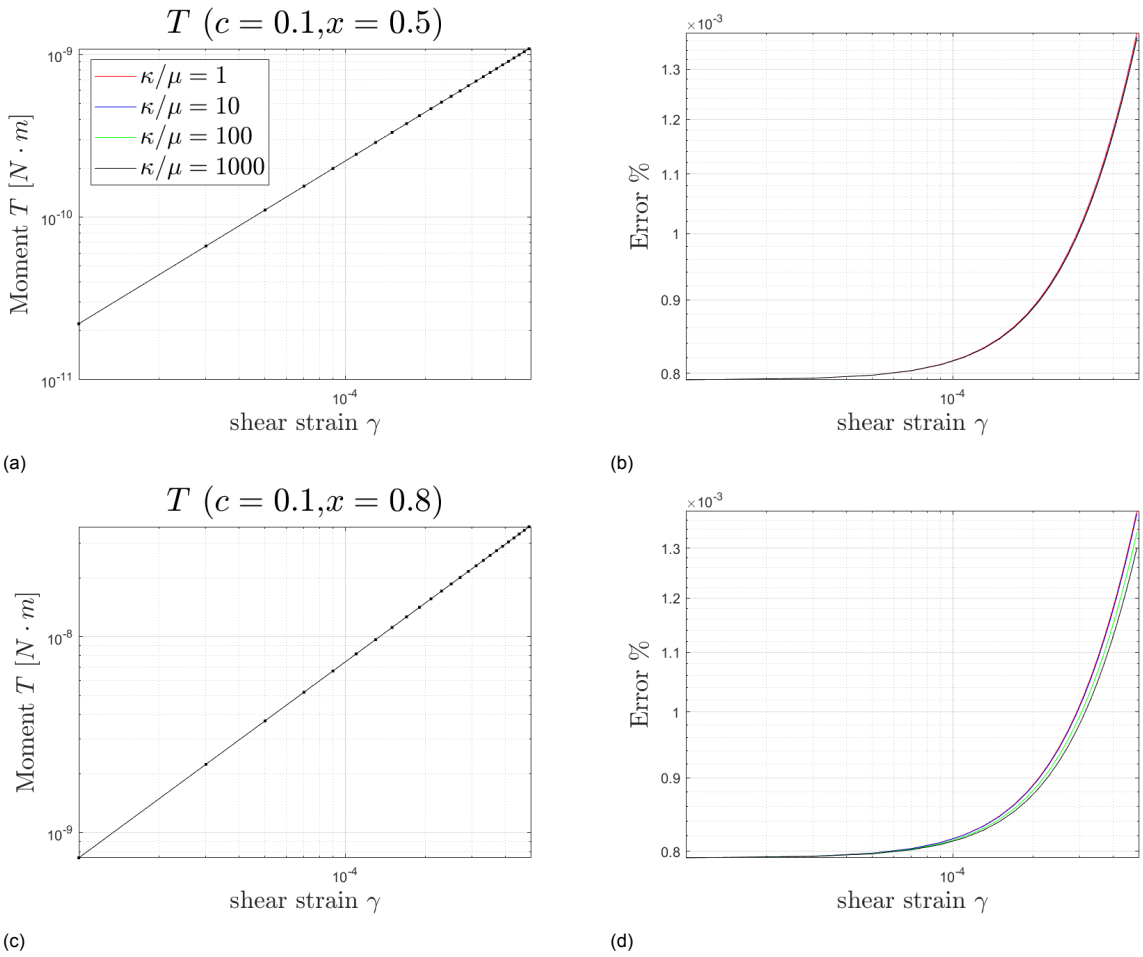

Figure 5.12: The moment required with respect to applied shear strain under constant gap boundary condition is plotted for material sets (a) ($c = 0.1$, $x = 0.5$) and (b) ($c = 0.1$, $x = 0.8$). The solid lines and dotted lines represent the analytical solution and the numerical solution, respectively. The corresponding error plots are shown by (c), and (d).

$$T_{\xi=const.} = \frac{2\pi R^3}{\gamma_o^3} \int_0^{\gamma_o} \gamma^2 \sigma_{yz,\xi=const.} d\gamma \tag{5.17}$$

The approximation of the required moment input follows a similar integration process as in the previous sections. To make the analysis more manageable, we express $\epsilon - 1$ and $\lambda - 1$ as functions of γ and ξ, effectively reducing the shear stress dependency to these two variables. Depending on the specific boundary conditions, we either set ξ to a constant value, resulting in the expression denoted as $\sigma_{yz,\xi=const.}$ under the constant gap boundary condition, or $\sigma_{yz,\sigma_{zz}=const.}$ under the constant normal stress boundary condition. The formulation for $\sigma_{yz,\xi=const.}$ is provided in Equation (5.17).

The numerical result is obtained by performing volumetric integration on $r\sigma_{\theta z}$ and subsequently dividing it by the gap of the cylinder. A comparison between Figure (5.12a) and Figure (5.12c) demonstrates a close alignment between the numerical and analytical solutions. In particular, the moment is a function of Poisson's ratio, resulting in distinct lines corresponding to varying bulk-to-shear ratios. However, the differences are minimal, giving the appearance of the curves collapsing into a single line. The error plot clearly illustrates that as shear strain increases, the solutions diverge from each other to a greater extent. Additionally, an increase in Poisson's ratio leads to a reduction in error. Nevertheless, within the range of shear strain under consideration, the error remains typically small, as evident in Figures

(5.12b) and (5.12d).

$$T_{\sigma_{zz}=const.} = \frac{2\pi R^3}{\gamma_o^3}\int_0^{\gamma_o} \gamma^2 \sigma_{yz,\sigma_{zz}=const.} d\gamma \tag{5.18}$$

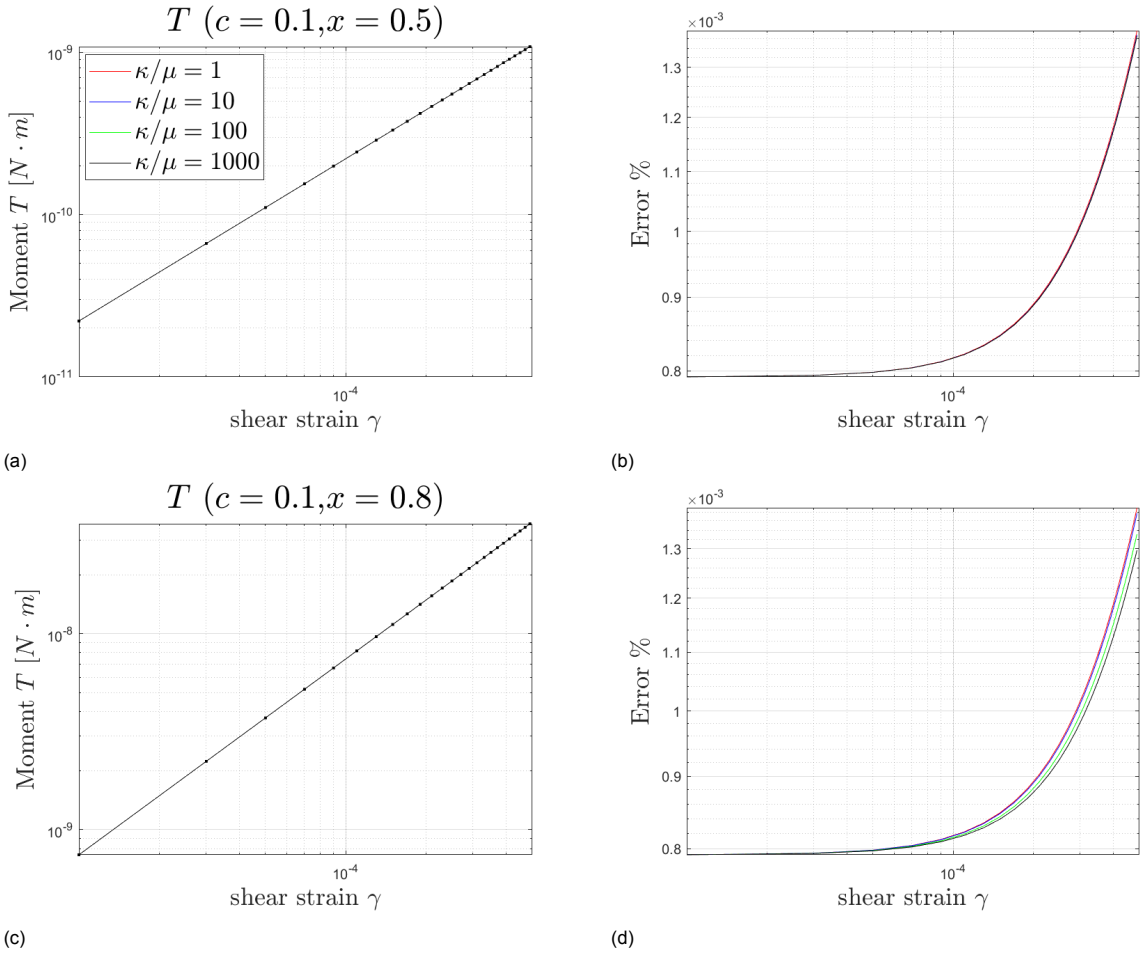

Figure 5.13: The moment required with respect to applied shear strain under constant normal stress boundary condition is plotted for material sets (a) ($c = 0.1$, $x = 0.5$) and (b) ($c = 0.1$, $x = 0.8$). The solid lines and dotted lines represent the analytical solution and the numerical solution, respectively. The corresponding error plots are shown by (c), and (d).

A similar analysis can be conducted for the case under the constant normal stress boundary condition. In Figure (5.13a) and Figure (5.13c), the moment appears to be identical to the one under the constant gap boundary condition. However, these two cases are actually distinct due to differences in their mathematical expressions. Fortunately, the error between the analytical and numerical solutions remains small.

Once the required moment is computed under both boundary conditions, we compare the difference between them to understand how the strain-stiffening effect is affected by the boundary conditions. This difference is calculated as $(T_\xi - T_{\sigma_{zz}})/\gamma_o^3$, where T_ξ and $T_{\sigma_{zz}}$ represent the moment under the constant gap and constant normal stress boundary conditions, respectively. We divide this difference by γ_o^3 because we expect that the strain-stiffening effect is primarily contributed by the cubic term of the shear strain.

Figures (5.14a) and (5.14b) illustrate the difference in the strain-stiffening effect between the two boundary conditions for materials with parameters $(c = 0.1, x = 0.5)$ and $(c = 0.1, x = 0.8)$. The dotted lines represent the difference obtained through numerical methods, while the solid lines represent the difference obtained through analytical approximations. The solid lines are horizontal in both figures, in

line with our prediction. However, some lines are absent because the difference becomes negative. In comparison to the numerical data, the difference is positive, at least when the strain is sufficiently small. It is also worth noting that the curves in the numerical data for the small strain range initially take the form of a linear curve with a negative slope. This slope is found to be -2, suggesting that at small strains, the difference in the moment is primarily influenced by the linear relationship with γ_o.

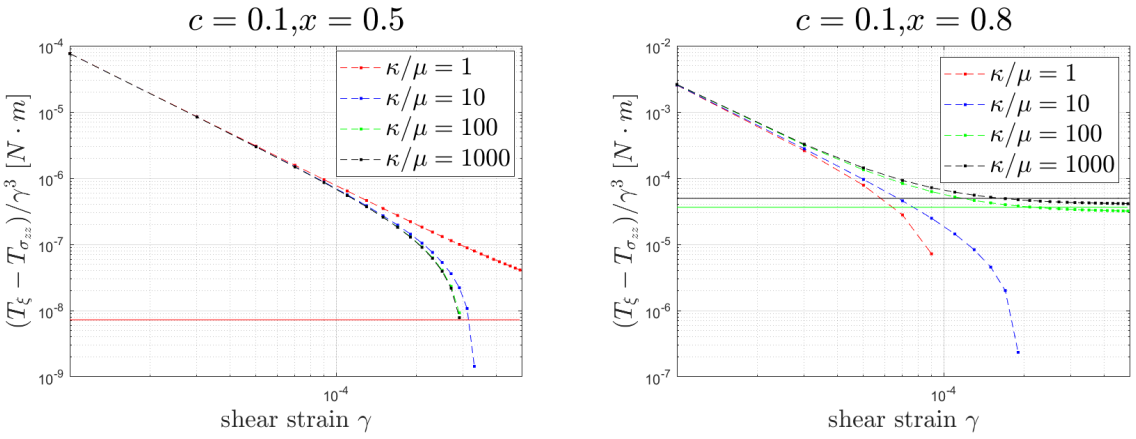

(a) (b)

Figure 5.14: The difference of strain-stiffening effect between two boundary conditions is plotted with the material sets (a) $c = 0.1, x = 0.5$ and (b) $c = 0.1, x = 0.8$. The solid lines represent the solution from analytical approximation and the dotted lines refer to the numerical solution. Some of the solid lines are absent because the corresponding values become negative.

5.6. Discussion

In this section, our objective is to explore the distinctions between the Comsol model and the analytical approximation. Additionally, we seek to assess the plausibility of the boundary conditions applied in deriving the approximation. Prior sections have highlighted the limited capacity of the analytical approximation to closely match the numerical data. This difference can be attributed partially to the boundary conditions specified earlier for analytical calculations and, in part, to certain limitations inherent to the Comsol simulation. In the last subsection (5.6.3), we will talk about the reason behind the choice of the particular approximation used in the preceding sections.

5.6.1. The plausibility of the boundary conditions

In the previous sections, we applied identical assumptions regarding boundary conditions as presented in Chapters 3 and 4. However, some distinctions between this chapter and previous chapters have likely caught your attention. In Chapters 3 and 4, when deriving the analytical solution, we assumed a cubic geometry. In contrast, Chapter 5 implements a simulation involving a cylindrical shape. The difference between these two geometries is primarily related to their homogeneity and the specific boundary conditions imposed.

It is obvious that for the cubic geometry, deformation remains homogeneous throughout the whole domain. This is not the case for the cylinder, where deformation varies based on the radial coordinate. To comprehensively explore and visualize the distribution of stress and strain responses within the cylinder, the following paragraphs utilize numerical solution data to address the distinctions between the model and our initial assumptions.

Firstly, we investigate the applied boundary conditions. Figure (5.15a) illustrates the radial distribution of the strain $\gamma_{\theta z}$ at the middle height of the cylinder. This data is obtained under conditions where normal stress is maintained as constant, with the material parameters set to $c = 0.1$ and $x = 0.5$. The distribution appears linear, with strain dropping to zero at the center of th cross-section and peaking at the outer edge, consistent with our original assumptions.

Figure (5.15b) shows the distribution of the normal stress σ_{rr} in relation to the radial position, while

maintaining the same boundary conditions and material parameters as in Figure (5.15a). The stress distribution clearly indicates non-zero values and exhibits radial dependency. On the edge of the cross-section, the stress reaches zero and gradually decreases as the radial position approaches the center. This contrast with our assumption of zero plane stresses across the entire section is readily obvious.

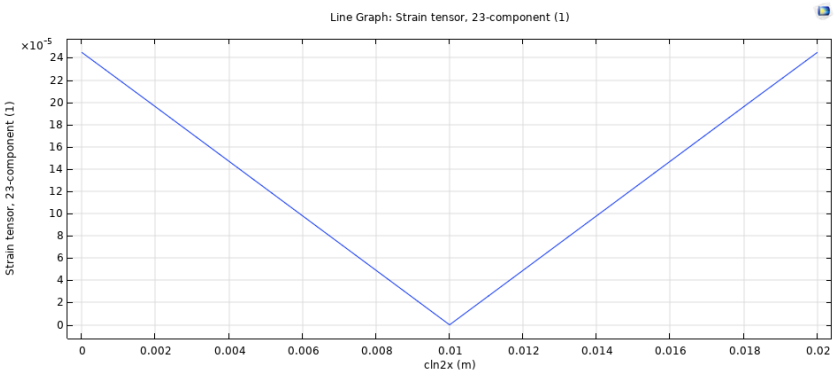

(a)

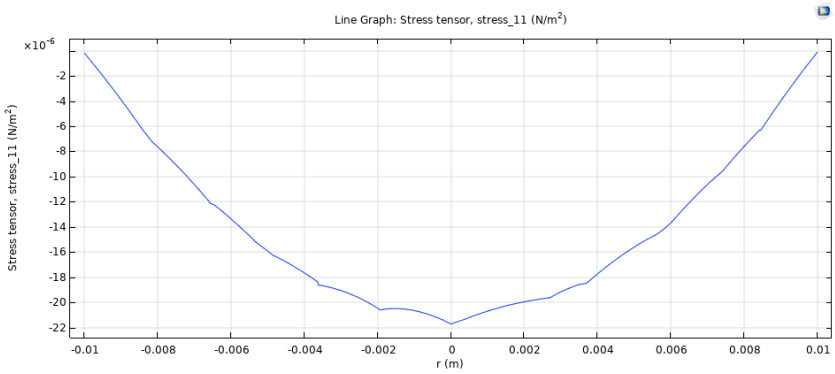

(b)

Figure 5.15: An illustration of the distribution of the (a) shear strain $\epsilon_{\theta z}$, and (b) the radial normal stress σ_{rr} with respect to the radial position. The zero of the x-axis corresponds to the center of the cross-section.

We also speculate the distribution of the stress $\sigma_{\theta\theta}$ to show that the assumptions of plane stress need further consideration. Figure (5.16a) presents an isotherm diagram of $\sigma_{\theta\theta}$ instead of a curve. This choice arises from our realization that assigning a specific value or function to the normal stress in the θ direction for solving the unknown variables in the deformation gradient tensor is not straightforward. Our aim here is to demonstrate that the value of $\sigma_{\theta\theta}$ is indeed non-zero.

In Figure (5.16b), we observe the distribution of σ_{zz}. Both figures indicate singularities at the centers of the cross-sections.

We take this opportunity to discuss how Comsol achieved the constant normal stress boundary condition. As Figure (5.16b) shows, there is a sign change in the normal stress somewhere between the center and the edge, suggesting that the constant normal stress is achieved in an average sense. To investigate the validity of this condition, we compute the average normal stress under the constant normal stress boundary condition and compare it to the value obtained under the constant gap boundary condition. The distribution is depicted in Figure (5.17), with the blue curve representing the constant gap situation and the red curve representing the constant normal stress situation. Although σ_{zz} under the constant normal stress condition is not zero and exhibits a similar trend to the one under the constant gap condition, the magnitude of stress under the constant normal stress condition is nearly a hundred times smaller. Therefore, we can conclude that Comsol successfully established the constant normal stress boundary condition.

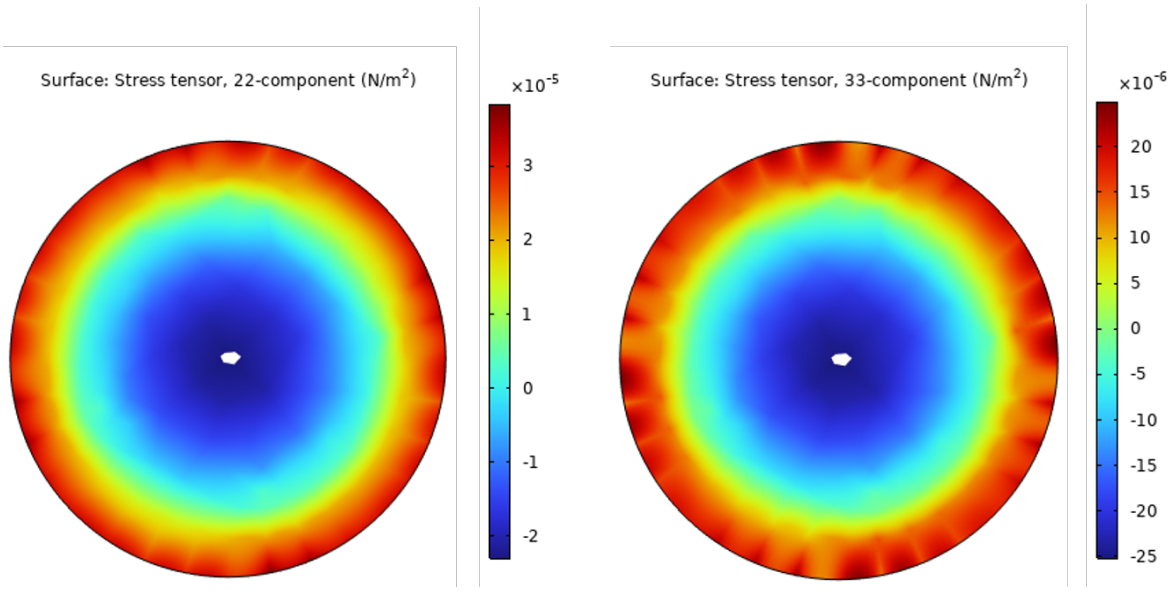

(a) (b)

Figure 5.16: Using the same material set, the normal stress (a) $\sigma_{\theta\theta}$ and (b) σ_{zz} both show a singularity point at the center. The distribution of $\sigma_{\theta\theta}$ implies that it should be assumed as zero.

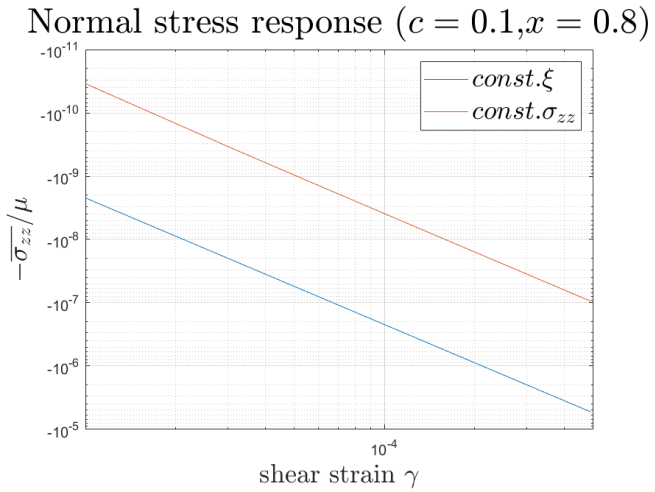

Figure 5.17: For material variables $(c = 0.1, x = 0.8)$, we compare the average transverse normal stress $\overline{\sigma_{zz}}/\mu$ under the constant gap (blue curve) and constant normal stress (red curve) boundary conditions. It is shown that the magnitude of the red line is almost a hundred times smaller than the blue line for a given shear strain, implying that the constant normal stress boundary condition is reached.

There is one more important point that requires clarification. In section (5.1), when we derived the approximation, we established the deformation gradient tensor in such a way that the deformation of the cylinder depends solely on the radial position. This implies that radial deformation should not be a function of the z position, and the geometry should remain cylindrical after deformation. However, due to the modeling choices we have made, the upper and bottom surfaces of the cylinder are held fixed. This constraint suppresses the radial deformation on these two surfaces, causing radial deformation to become dependent on both the r and z coordinates.

The reason for not creating a model that aligns with this assumption is that it is not practically feasible to do so. Although it has been claimed as possible in a previous paper [68], our attempts to replicate their setup did not yield the expected results. Therefore, both surfaces are maintained as fixed boundaries in our model, as this at least provides some similarity with the experimental observations.

5.6.2. Analogy of the cylinder and cube

In this subsection, we will provide a brief overview of the implementation of a deformation gradient tensor based on a cylindrical approach. We will also outline the challenges encountered while attempting to solve the problem using this approach. Subsequently, we will introduce an alternative method for deriving a different approximation of the analytical solution, grounded in cube deformation.

We start with the deformation of the cylinder that has been used in previous papers, such as [69], as shown in equation (5.19). r,θ, and z represents the deformed cylindrical frame; and R, Θ, and Z denote the reference frame. The deformation equations show that the radial deformation is solely dependent on the reference radial position, the deformation in θ direction is governed by the shear, and the deformed z has a linear relation with the reference position Z by a factor ξ.

$$\begin{aligned} r &= r(R), \\ \theta &= \Theta + \phi(z), \\ z &= \xi Z \end{aligned} \tag{5.19}$$

$\phi(Z)$ could be approximated as a linear function with respect to the Z coordinate, which we assumed as $\phi(Z) = \tau Z$, where τ denotes the applied rotation angle ϕ_0 over the height of the cylinder H. Following the concept that the element of the Green-Cauchy tensor $e_{\theta z}$ is only dependent on the shear strain $\gamma = r\tau$, an extra R/r is multiplied to $r\tau$. Therefore, the deformation gradient tensor could be derived.

$$\mathbf{F} = \begin{bmatrix} r'(R) & 0 & 0 \\ 0 & \frac{r}{R} & r\tau\frac{R}{r} \\ 0 & 0 & \xi \end{bmatrix} \tag{5.20}$$

By applying this tensor, we assume four unknowns, which are $r(R)$, $r'(R)$, τ, and ξ. With the deformation gradient tensor, the expressions for stresses could be derived as σ_{rr}, $\sigma_{\theta\theta}$, and σ_{zz}, which results in extra three unknowns.

Then, we write down the boundary conditions

$$\begin{aligned} &(1) \quad \sigma_{rr}(r = R) = 0, \\ &(2) \quad \begin{cases} \overline{\sigma_{zz}} = 0 \\ \xi = 1 \end{cases} \end{aligned} \tag{5.21}$$

Given the aforementioned boundary conditions, it is evident that one additional boundary condition is required. The limitation arises from the inability to predefine $\sigma_{\theta\theta}$; instead, we must first determine the unknowns within the tensor and then utilize the solution to calculate the value of $\sigma_{\theta\theta}$.

In Chapter 4, we encountered a similar problem with seven unknowns: γ, ϵ, λ, ξ, σ_{11}, σ_{22}, and σ_{33}. However, through the control of γ and the imposition of boundary conditions on σ_{11} and σ_{22}, along with an additional constraint related to either constant normal stress or a constant gap, we were able to apply predetermined stress values in the stress-strain equations, effectively reducing the number of unknowns to three and allowing for analytical solutions.

In contrast, in the current situation, we have seven unknowns, yet only two boundary conditions can be applied, indicating the need for an additional assumption or relationship.

Given the complexity of the problem, our initial approach involves approximating it using cube deformation. Through observation, we have noted that the deformation of the cylinder under small torsion can be expressed using Cartesian coordinates, as illustrated in Figure (5.18).

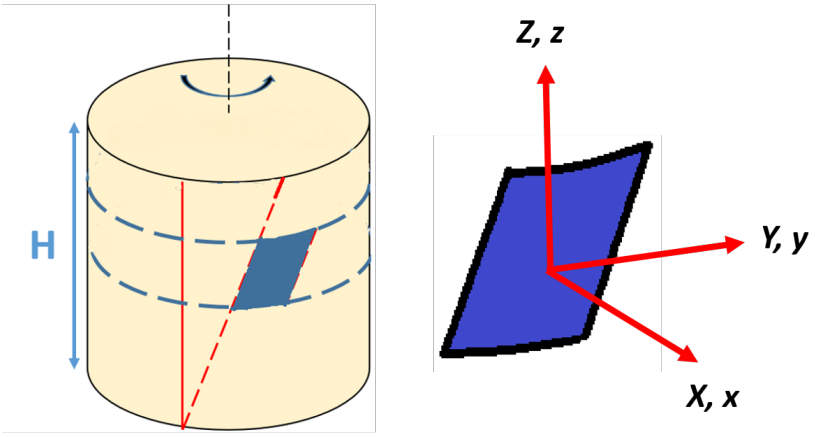

Figure 5.18: For material variables ($c = 0.1, x = 0.8$),

To derive the deformation tensor, we first outline our assumed deformation. Based on the figure, it is evident that the deformation in the y direction is solely influenced by the shear strain. Consequently, we can establish that F_{yy} remains equal to one, while F_{yz} is defined as $\gamma = R\tau$. This assumption can be translated into a relationship, specifically $\lambda = 1/\epsilon$.

Furthermore, the cylinder has the capability to either elongate or contract along the z-axis, and its cross-section can dilate or contract in an axisymmetric manner. Therefore, we assume that the elements F_{xx} and F_{zz} take on the values of ϵ^2 and ξ respectively. This results in the formation of the corresponding tensor, as expressed in equation (5.22).

$$\mathbf{F} = \begin{bmatrix} \epsilon^2 & 0 & 0 \\ 0 & 1 & \gamma \\ 0 & 0 & \xi \end{bmatrix} \tag{5.22}$$

Similar to the steps used in previous chapters to derive the stress responses, we obtain another set of expressions of the stresses. The Taylor expansion of the stresses is shown in equation (5.23).

$$\begin{aligned}
\sigma_{xx} &= \frac{2x^2(-1-4x^2-x^4+c^2\pi^3(-1+x^2)^4)\gamma^2\mu}{9c\pi(-1+x^2)^4} + (-1+\epsilon)(2\kappa - \frac{16x^2(1+x^2+c^2\pi^3(-1+x^2)^3)\mu}{9c\pi(-1+x^2)^3}) \\
&\quad + (\kappa + \frac{4x^2(1+x^2+c^2\pi^3(-1+x^2)^3)\mu}{9c\pi(-1+x^2)^3})(-1+\xi), \\
\sigma_{yy} &= \frac{-2x^2(-2-2x^2+x^4+2c^2\pi^3(-1+x^2)^4)\gamma^2\mu}{9c\pi(-1+x^2)^4} + \frac{(-1+\epsilon)}{9}(18\kappa + \frac{8x^2(1+x^2+c^2\pi^3(-1+x^2)^3)\mu}{c\pi(-1+x^2)^3}) \\
&\quad + \frac{1}{9}(9\kappa + \frac{(4x^2(1+x^2+c^2\pi^3(-1+x^2)^3)\mu)}{(c\pi(-1+x^2)^3)})(-1+\xi), \\
\sigma_{zz} &= \frac{2x^2(-4+12x^4-8x^6+4c^2\pi^3(-1+x^2)^6+8x^2(2-3x^2+x^6))\gamma^2\mu}{9c\pi(2-6x^2+6x^4-2x^6)^2} \\
&\quad + (-1+\epsilon)(2\kappa + \frac{8x^2(1+x^2+c^2\pi^3(-1+x^2)^3)\mu}{9c\pi(-1+x^2)^3}) + (\kappa - \frac{8x^2(1+x^2+c^2pi^3(-1+x^2)^3)\mu}{9c\pi(-1+x^2)^3})(-1+\xi), \\
\sigma_{yz} &= \frac{-2x^2(1+x^2+c^2\pi^3(-1+x^2)^3)\gamma\mu}{3c\pi(-1+x^2)^3} - \frac{4x^4(1+x^2)\gamma^3\mu}{3c\pi(-1+x^2)^5} + \frac{4x^2(-5-8x^2+x^4+5c^2\pi^3(-1+x^2)^4)\gamma(-1+\epsilon)\mu}{9c\pi(-1+x^2)^4} \\
&\quad + \frac{4x^2(-1+2x^2+2x^4+c^2\pi^3(-1+x^2)^4)\gamma\mu(-1+\xi)}{9c\pi(-1+x^2)^4}.
\end{aligned} \tag{5.23}$$

The boundary conditions for solving the problem are given as follows.

$$\begin{aligned}
&(1) \quad \sigma_{xx} = 0, \\
&(2) \quad \begin{cases} \overline{\sigma_{zz}} = 0 \\ \xi = 1 \end{cases}
\end{aligned} \tag{5.24}$$

The solution for the unknowns has been obtained, allowing us to derive the average normal stress $\overline{\sigma_{zz}}/\mu$ and the elongation in the z-axis ξ using integration methods. For brevity, the explicit expressions of $\overline{\sigma_{zz}}/\mu$ and ξ are not presented here as they involve rather complicated mathematical forms.

A comparative analysis between the analytical approximation and the numerical solution is depicted in Figure (5.19). In this figure, the dotted lines represent the results obtained through simulation, while the solid lines correspond to the approximation employed in this subsection. Figure (5.19a) illustrates the elongation under the constant normal stress boundary condition, and Figure (5.19b) illustrates the response of the average normal stress, denoted as $-\overline{\sigma_{zz}}/\mu$.

It is worth noting that solid lines other than the red ones are absent in the figures. This is because the values of these curves become negative, indicating that an increase in the Poisson's ratio contributes to a tendency toward a negative Poynting effect. This outcome notably diverges from the observation made in the simulation results.

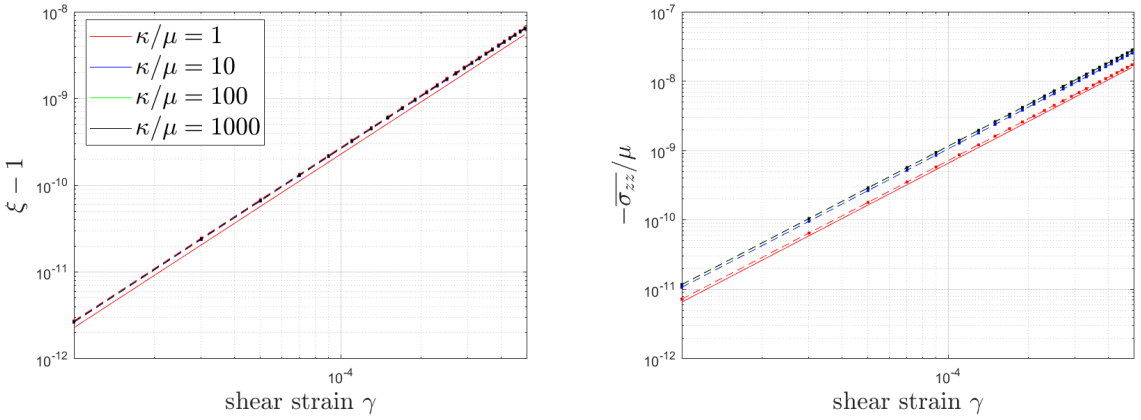

(a) (b)

Figure 5.19: For material variables $(c = 0.1, x = 0.8)$,(a) the FEM solution and the analytical solution show a good agreement on the change of average volume ratio $\overline{J} - 1$. The error of each case is shown in (b).

5.6.3. Solving by cylindrical deformation gradient tensor

In the preceding subsection, we introduced a general assumption for the cylindrical deformation gradient tensor, as denoted in equation (5.20). It was also highlighted that the boundary conditions provided in equation (5.21) are insufficient to fully solve the problem.

A proposed solution, commonly mentioned in previous research papers to address this issue, involves the concept of stress equilibrium. Given that the stresses $\sigma_{r\theta}$ and σ_{rz} are both zero, the equilibrium of stress in the r-direction yields the relationship expressed in equation (5.25). Ideally, this relationship offers a means to effectively solve the problem.

$$\frac{d\sigma_{rr}}{dr} + \frac{\sigma_{rr} - \sigma_{\theta\theta}}{r}. \tag{5.25}$$

Nonetheless, when we derive the stress expressions using the deformation gradient tensor (5.20) and insert them into relation (5.25), it leads to a nonlinear, homogeneous, second-order ordinary differential equation. This equation takes the form displayed in equation (5.26), where the coefficients A_n are placeholders for various parameters.

$$A_1 R^2 r r'' = A_2 R r r' + A_3 R^2 r'^2 + A_4 r^2 + A_5 R^4 r' + A_6 R^3 r. \tag{5.26}$$

Due to the inherent nonlinearity of the equation, finding a straightforward solution has proven to be challenging. Moreover, our search for previous papers did not yield any instances where the equation was solved directly. Instead, most researchers have resorted to alternative methods aimed at simplifying or approximating the solution.

For instance, in reference [70], deformation is approximated by linearly combining extension and torsion, which is a relatively intricate method. For the rest of this subsection, we will adopt another simplification used in [68].

Another assumption has been made in [68]. In this research, the deformation in the radial direction is assumed as $r = \epsilon_c R$, where $\epsilon_c = F_{rr}$ is a constant. It suggests that the radial deformation gradient is universal inside the cylinder. The shear in the $r\theta$ plane is zero because of the axisymmetric nature of the cylinder under torsion, which corresponds to $\lambda = 1$. The deformation gradient could therefore be written as equation 5.27 and the number of unknowns reduces to three.

$$\mathbf{F} = \begin{bmatrix} \epsilon_c & 0 & 0 \\ 0 & \epsilon_c & \gamma/\epsilon_c \\ 0 & 0 & \xi \end{bmatrix} \tag{5.27}$$

In the following paragraphs, we will analyze the response of this tensor and conduct a comparative analysis with simulation results. By applying the deformation gradient tensor, we derive a new set of stress expressions and their corresponding Taylor expansions. Rather than presenting the complete set of expressions here, readers can refer to the Taylor expansions derived in equations (4.6) to (4.9) and set $\lambda = 1$ for the specific stress expressions. As a result, we omit the detailed stress expressions in this section.

With the assumption of $\lambda = 1$, we proceed to derive the analytical solution for the average stress $\overline{\sigma_{zz}}$ and the elongation ξ_c using the following methodology. Initially, we apply the first boundary condition specified in equation (5.21) to establish an expression for $\epsilon_c - 1$ in terms of γ and ξ. As this boundary condition exclusively applies to the side surface, this expression for $\epsilon_c - 1$ also becomes a function of the shear strain at the surface, denoted as γ_o.

$$\epsilon_c - 1 = \frac{9c\pi(-1+x^2)^4\kappa(-3+\xi) + 2c^2\pi^3x^2(-1+x^2)^4\mu(\gamma_o^2+2\xi) - 2x^2\mu((1+4x^2+x^4)\gamma_o^2 - 2(-1+x^4)\xi)}{2(-1+x^2)(-9c\pi(-1+x^2)^3\kappa + 2c^2\pi^3x^2(-1+x^2)^3\mu + 2x^2(1+x^2)\mu)} - 1 \tag{5.28}$$

The expression of $\epsilon_c - 1$ is then applied to σ_{zz} so that it also becomes a function of γ, γ_o and ξ. Then, by employing the relevant second boundary condition and integrating the expression over the range from $\gamma = 0$ to $\gamma = \gamma_o$, we are able to derive expressions for $\overline{\sigma_{zz}}$ and ξ_c. These expressions are notably complex, and for the sake of brevity, we have omitted them in this context.

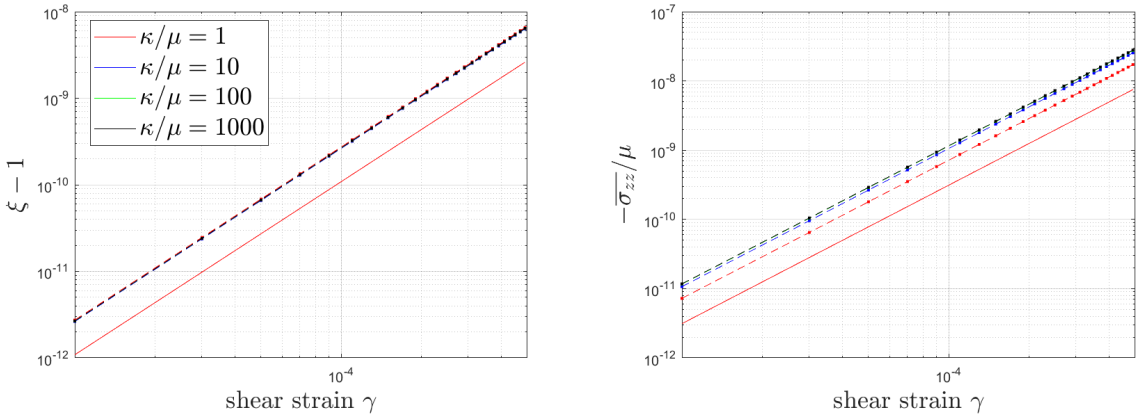

(a) (b)

Figure 5.20: For material variables $(c = 0.1, x = 0.8)$,(a) the FEM solution and the analytical solution show a good agreement on the change of average volume ratio $\overline{J} - 1$. The error of each case is shown in (b).

The comparative analysis between the analytical approximation and the numerical solution is presented in Figure (5.20). It's worth noting that the solid lines corresponding to higher Poisson's ratios are absent from the figures, as their values become negative. This observation indicates that the approximation does not yield a satisfactory result in these cases.

5.6.4. The choice of the analytical approximation

Previous attempts to approximate the numerical results have yielded unsatisfactory outcomes, particularly due to the fact that, in the numerical investigation, the Poisson's ratio (i.e., compressibility) does not impact the sign of the Poynting effect. We chose not to pursue the approximation method implemented in reference [70], which combines extension and torsion to approximate simple shear, recognizing that it still constitutes an approximation and, particularly, a complicated one. Our primary goal is to establish a straightforward means of predicting the sign of the Poynting effect, rather than striving for a more accurate approximation of the numerical results.

The final choice we adopted, as previously introduced in subsection (5.1) and applied for comparative studies, is based on its similarity to the tensor in Equation (5.20), where the elements F_{rr} and $F_{\theta\theta}$ are treated as distinct variables. We believe that the degree of freedom we introduced in this approach significantly influenced the final results. Therefore, even if the boundary condition in the r direction cannot be perfectly replicated, we can still obtain results that exhibit a high degree of similarity.

A final point of discussion focuses on why both cylindrical and cubic geometries exhibit identical signs of the Poynting effect within the context of our chosen model and material sets. Our comparative study has indicated that the analytical approximation aligns well with the numerical solutions, suggesting that the sign of the Poynting effect in the cylinder is indeed primarily contingent on the material parameters (c, x). Therefore, this consistency in sign is maintained under both boundary conditions.

In essence, the similarity in sign between the cylindrical and cubic geometries marks the significance of the underlying material properties in determining the sign of the Poynting effect. These findings emphasize that, for the specific model and material parameters considered, the geometrical differences between cylindrical and cubic setups do not introduce any change in the sign of the Poynting effect. Instead, the material parameters remain the key factor in shaping this phenomenon.

6

Conclusion

In Chapter 3 and Chapter 4, we have proven that the choice of the tensor is a crucial part of studying the stress-strain response under two main boundary conditions set: constant height boundary condition and constant normal stress boundary condition. We investigated two different deformation gradient tensors. The tensor $\mathbf{F}_1$ is a tensor used by the past papers that only included two variables, which are shear strain γ and the transverse deformation gradient λ_2. The other tensor is a more general tensor $\mathbf{F}_g$ that includes two more variables: ϵ and λ, which correspond to the dilation and shear on the xy-plane. The strain energy function proposed by Meng is then applied to the tensors. After transforming Meng's model into an isochoric function and adding an extra volumetric part, the expression of the stress components could be explicitly calculated with different Poisson's ratios. It is worth noting that, since we only focus on the small but finite strains in this research, therefore, the Taylor expansion of the expressions of stress components is derived since it is easier for us to obtain numerical solutions. For tensor $\mathbf{F}_1$, the control variable is γ, and therefore only one boundary condition is required to compute another variable λ_2. Namely, we cannot say anything about the normal stresses in the other two directions. On the other hand, the introduction of two other variables enables us to define the boundary conditions in the other two directions using tensor $\mathbf{F}_g$. The normal stress in the other two directions is assumed to be traction free, therefore $\sigma_{xx} = 0$ and $\sigma_{yy} = 0$ are applied. The difference in the boundary conditions results in a huge deviation of the final results.

Under constant height boundary conditions, where the transverse deformation gradient λ_2 or ξ are held as one, the normal stress response in the z-direction σ_{zz} always shows the same sign of the Poynting effect. However, the magnitude of the normal stress shows distinct characteristics. The magnitude of the normal stress does not vary with Poisson's ratio when $\mathbf{F}_1$ is applied. On the other hand, the general tensor $\mathbf{F}_g$ shows that the magnitude of the normal stress increases with the Poisson's ratio reaching 0.5. The change of volume ratio $J-1$ is also different for each tensor. Since for $\mathbf{F}_1$, the volume ratio J always equals one under this boundary condition, therefore, the system becomes isochoric. The general tensor $\mathbf{F}_g$, on the other hand, shows that the system always performs the opposite sign as the Poynting effect. For example, the positive Poynting effect always corresponds to the shrinking of the system. Also, since we introduce two more variables in $\mathbf{F}_g$, we also found that the dilation factor $\epsilon - 1$ on the xy-plane always shows opposite sign as well, inferring that the positive Poynting effect causes ϵ to show the tendency to shrink on the xy-plane. The other parameter $\lambda - 1$ is always negative disregarding the sign of the Poynting effect, inferring that under the constant height boundary condition, the shear factor $lambda$ on the xy-plane shows the tendency to elongate in the x-direction and shrink in the y-direction. These two factors together result in an elongation in the x-direction and a shrink in the y-direction, indifferent to the sign of the Poynting effect.

Under the constant normal stress boundary condition, the sign of the Poynting effect under both boundary conditions is also identical. The normal stress in the transverse direction is set as zero, which stems from the fact that at the initial state, the transverse normal stress should be stress-free if no prestress is applied. The transverse deformation gradient λ_2 in $\mathbf{F}_1$ and ξ in $\mathbf{F}_g$ will vary with the shear strain. For $\mathbf{F}_1$, the transverse deformation gradient λ_2 could be obtained simply by solving $\sigma_{yy} = 0$. With the increase

of Poisson's ratio, λ_2 decreases for a given γ. On the other hand, ξ in $\mathbf{F}_g$ does not vary with the Poisson's ratio. The volume change $J-1$ of the tensor $\mathbf{F}_1$ equals λ_2-1 since the other two principle strains equal one, therefore the sign of $J-1$ is identical to λ_2-1, thus it is dependent on the Poisson's ratio. For $\mathbf{F}_g$, however, the sign of $J-1$ is hard to predict. The volume ratio $J=\epsilon^2\xi$ is in a tug-of-war between two strain variables, therefore, there is no monotonic feature. Instead, the ratio fluctuates beyond and below $J=1$ under small shear strain. Within the xy-plane, it is found that λ, which represents the shear in xy-plane, is identical under both boundary conditions. Therefore, it also contributes to the tendency to expand in the x-direction and contract in the y-direction. On the other hand, $\epsilon-1$, representing the dilational change in xy-plane, always shows the opposite sign with $\xi-1$. Combining these two factors, the system shows expansion in the x-direction, namely, $F_{xx}>1$, and contraction in the y-direction, $F_{yy}<1$.

In this thesis, we have successfully constructed a method to predict the sign of the Poynting effect under small but finite strain by simply analyzing the chosen material parameters, without actually calculating the stress-strain responses. The method is primarily based on Maxwell's relation, which has been derived for both of the tensors. It is worth noting that, because of the range of shear strain that we are interested in, the Taylor expansions of the stresses are used. It is found that under the constant height boundary condition, the sign of both tensors could be determined solely by the sign of the Poynting coefficient χ, which is the coefficient of the γ^2 term of the transverse normal stress. Moreover, the expression for χ is identical for both tensors. Under the constant normal stress boundary condition, the sign could be predicted cooperatively by the sign of the Poynting effect χ and λ_L, which represents the coefficient of the ξ or λ_2 term in the transverse normal stress. The expression of the prediction could be written as $-\chi/\lambda_L$. In both cases, λ_L is always negative and thus cancels out the effect of the minus sign. Therefore, the distribution of the sign of the predictor is identical to the one of χ.

The difference between the strain-stiffening effect in the shear stress under each boundary condition shows that the extent of the difference could be represented by an expression $3\chi^2/\lambda_L$. It infers that the Poynting coefficient χ does not contribute to the sign of the expression since it is a square term. Also, taking into account that the coefficient λ_L is always negative because of the chosen model, we conclude that the strain-hardening effect is always more pronounced under the constant height boundary condition than under the constant normal stress boundary condition.

Lastly, we have implemented a simulation in Comsol. The simulation shows good alignment with the analytical prediction of the sign of the Poynting effect. One interesting result is that even though the geometry changes, the sign still remains identical. We believe the reason behind this phenomenon is that, under simple shear deformation, the sign is solely dependent on the material set, the end-to-end ratio, and the stiffness parameter. Therefore, the geometry only affects the magnitude of the responses, but not the sign of the Poynting effect.

7

Recommendations

Viscoelasticity

In this investigation, we present evidence indicating that compressibility does not influence the sign of the Poynting effect. This discovery contradicts experimental observations, where compressible materials tend to exhibit a greater potential of displaying a negative Poynting effect, whereas the majority of incompressible materials exhibit a positive Poynting effect. Our analytical solution has effectively predicted the Poynting effect's direction, a validation further supported by a numerical model using Comsol. This leads us to speculate that viscoelasticity may underlie the observed sign change. As discussed in Chapter 2, soft matter materials may exhibit viscoelastic properties, resulting in time-dependent deformation. This concept aligns with the findings presented in the paper referenced as [71], which explores how the Poynting effect's sign evolves over time. Notably, in the paper [1] that inspires this research, the experimental data was collected after subjecting the material to a certain shear strain for 10 seconds. Although we initially assumed quasi-static deformation, it is plausible that it is time-dependent, thereby affecting the Poynting effect's sign.

Effect of porosity

Expanding upon the aforementioned point, there exists another intriguing possibility worth exploring. In our analysis of the Poynting coefficient, denoted as χ and elaborated upon in Chapter 4, a crucial observation emerges: its expression remains unaffected by Poisson's ratio. This implies that χ solely depends on the shear modulus μ, regardless of the bulk modulus κ. Furthermore, it is noteworthy that χ is directly proportional to the magnitude of μ, meaning that altering the shear modulus's magnitude does not alter the sign of χ. This characteristic appears to be a universal phenomenon, regardless of the specific volumetric energy density function employed.

The underlying reason for this phenomenon can be traced to the derivation of the γ^2 term within χ, which exhibits independence from the choice of volumetric energy density function. Instead, it relies solely on the isochoric part of the energy density function. Given our successful validation of χ through numerical solutions, we propose that any mechanism by which compressibility influences the Poynting effect's sign must inherently involve the bulk modulus κ within the Poynting coefficient.

One potential approach involves incorporating the effect of porosity within the isochoric component. Porosity inherently engages both the shear and bulk moduli, as evidenced in paper [72], where the original shear and bulk moduli are transformed into their effective counterparts. Nevertheless, replacing the shear modulus with its effective counterpart does not resolve the issue, as χ remains proportional to the shear modulus, thus the sign remains unchanged. The proposed solution involves introducing an independent term that consists of the isochoric invariants, $\tilde{I_1}$ or $\tilde{I_2}$, while exclusively involving the bulk modulus. By incorporating this new term, we aim to enable a competitive interplay between the

individual μ and κ components within χ, with the hope of inducing a change in sign as the Poisson's ratio varies.

While adding an extra term seems to be straightforward, a more rigorous derivation of how this function should be incorporated needs further investigation. As a result, this research acknowledges the potential for such a modification without presenting a definitive solution at this stage.

The setting of the numerical model

In Chapter 5, we discussed our attempt to replicate the findings from [68] using the Comsol model. Unfortunately, this endeavor did not yield results consistent with the referenced study. Consequently, it became evident that the geometry of the cylinder in our model underwent significant alterations following deformation. Although our Chapter 5 model was designed to closely mimic the experimental setup, it is advisable for future researchers to explore alternative approaches. This could involve utilizing different finite element analysis (FEM) software or adjusting the model settings to achieve a deformation gradient tensor that aligns with the initial assumption. It is important to highlight that the ideal setup may not be possible to implement with the latest version of Comsol, as per our experience when reaching out to customer support for assistance.

By verifying and ensuring the validity of this assumption, we anticipate that the strain response ξ in its cylindrical form will no longer exhibit a dependency on the z-position. This attempt can enhance the accuracy and reliability of the modeling process, ultimately leading to a better representation of the experimental outcomes.

Approximation

The approximation applied in Chapter 5 has demonstrated its utility in determining the sign of the Poynting effect, and to a certain extent, estimating both the magnitude of the Poynting effect and the alteration in volume ratio. However, it is worth noting that this approximation, while effective, may not represent the optimal approach available.

Our study did not comprehensively explore all the existing literature on methods to approximate the deformation of a cylinder under torsion. There are alternative proposals within this field that need further investigation. These alternative methods hold the potential to refine our understanding and provide more precise approximations for modeling the deformation process, ultimately enhancing the accuracy of our predictions and analyses. Future research endeavors should consider exploring these promising alternatives to advance the field's knowledge and capabilities.

Strain-stiffening effect

In Chapter 5, we presented evidence suggesting that the approximation method could successfully predict the phenomenon of strain stiffening. However, an important observation emerged regarding the difference in the strain stiffening effect under two distinct boundary conditions. This difference between the boundary conditions did not align with our initial expectations, as it revealed that the strain stiffening effect is primarily dictated by the shear strain γ in a linear fashion under small γ, rather than the anticipated cubic relationship.

This outcome implies the need for a more in-depth investigation into our initial assumptions and expectations regarding strain stiffening. It indicates that our understanding of the underlying mechanisms may be incomplete or, not entirely accurate. Therefore, further research to examine the nuances of strain-stiffening effect is recommended.

Bibliography

[1] A. Fall, B. P. Tighe, and D. Bonn. “Tuneable normal stresses in hyperelastic emulsions.” In: *Physical Review Research* 4(1) (2022).

[2] M. Vahabi et al. “Normal stresses in semiflexible polymer hydrogels.” In: *Physical Review E* 97(3) (2018), pp. 1555–1564.

[3] C. O. Horgan and J. G. Murphy. “Poynting and reverse Poynting effects in soft materials.” In: *Soft Matter* 13(28).6 (2017), pp. 4916–4923.

[4] C. Truesdell and W. Noll. *The non-linear field theories of Mechanics*. Springer, 2004.

[5] H. B. Khaniki et al. “A review on the nonlinear dynamics of hyperelastic structures.” In: *Nonlinear Dynamics* 110(2) (2022), pp. 963–994.

[6] V. Kumar et al. “Microengineered Materials with Self-Healing Features for Soft Robotics.” In: *Advanced Intelligent Systems* 3(7) (2021).

[7] Z. Peng and J. Huang. “Soft Rehabilitation and Nursing-Care Robots: A Review and Future Outlook”. In: *Applied Sciences* 9(15) (2019).

[8] C. O. Horgan and G. Saccomandi. “Phenomenological hyperelastic strain-stiffening constitutive models for rubber”. In: *Rubber Chemistry and Technology* 79(1) (2006), pp. 152–169.

[9] R. W. Ogden. *Non-linear elastic deformations*. Horwood, 1984.

[10] L. H. Adams and R. E. Gibson. “The compressibility of rubber”. In: *Rubber Chemistry and Technology* 3(4) (1930), pp. 555–562.

[11] M. F. Beatty. “Topics in finite elasticity: Hyperelasticity of rubber, elastomers, and biological tissues—with examples.” In: *Applied Mechanics Reviews* 40(12) (1987), pp. 1699–1734.

[12] C. O. Horgan and J. G. Murphy. “Constitutive models for almost incompressible isotropic elastic rubber-like materials”. In: *Journal of Elasticity* 87(2-3) (2007), pp. 133–146.

[13] I. W. Burgess and M. Levinson. “The instability of slightly compressible rectangular rubberlike solids under biaxial loadings”. In: *International Journal of Solids and Structures* 8(2) (1972), pp. 133–148.

[14] C. O. Horgan and J. G. Murphy. “Simple shearing of incompressible and slightly compressible isotropic nonlinearly elastic materials Journal of Elasticity”. In: *International Journal of Solids and Structures* 98(2) (2009), pp. 205–221.

[15] C. O. Horgan and G. Saccomandi. “Constitutive models for compressible nonlinearly elastic materials with limiting chain extensibility.” In: *Journal of Elasticity* 77(2) (2004), pp. 123–138.

[16] C. O. Horgan and M. G. Smayda. “The importance of the second strain invariant in the constitutive modeling of elastomers and soft biomaterials”. In: *Mechanics of Materials* 51 (2012), pp. 43–52.

[17] C. O. Horgan. “The remarkable gent constitutive model for hyperelastic materials”. In: *International Journal of Non-Linear Mechanics* 68 (2015), pp. 9–16.

[18] C. O. Horgan and G. Saccomandi. “Constitutive models for Atactic elastomers”. In: *Waves and Stability in Continuous Media* (2004).

[19] O. Lopez-Pamies. “A new -based hyperelastic model for rubber elastic materials”. In: *Comptes Rendus Mécanique* 338(1) (2010), pp. 3–11.

[20] R. W. Ogden, G. Saccomandi, and I. Sgura. “Fitting hyperelastic models to experimental data”. In: *Computational Mechanics* 34(6) (2004), pp. 484–502.

[21] J. C. Gardiner and J. A. Weiss. “Simple shear testing of parallel-fibered planar soft tissues”. In: *Journal of Biomechanical Engineering* 123(2) (2000), pp. 170–175.

[22] C. O. Horgan and J. G. Murphy. “Enhancement of protocols for simple shear of isotropic soft hyperelastic samples”. In: *Journal of Elasticity* (2022).

[23] M. Destrade et al. “Slight compressibility and sensitivity to changes in Poisson’s ratio”. In: *International Journal for Numerical Methods in Engineering* 90(4) (2011), pp. 403–411.

[24] M. Destrade, J. G. Murphy, and G. Saccomandi. “Simple shear is not so simple”. In: *International Journal of Non-Linear Mechanics* 47(2) (2012), pp. 210–214.

[25] J. H. Poynting. “On pressure perpendicular to the shear planes in finite pure shears, and on the lengthening of loaded wires when twisted”. In: *Proceedings of the Royal Society of London. Series A, Containing Papers of a Mathematical and Physical Character* 82(557) (1909), pp. 546–559.

[26] F. Meng and E. M. Terentjev. “Nonlinear elasticity of semiflexible Filament Networks”. In: *Soft Matter* 12(32) (2016), pp. 6749–6756.

[27] A. R. Cioroianu and C. Storm. “Normal stresses in elastic networks”. In: *Physical Review E* 88(5) (2013).

[28] C. Storm et al. “Nonlinear elasticity in biological gels”. In: *Nature* 435(7039) (2005), pp. 191–194.

[29] F. Meng and E. Terentjev. “Theory of semiflexible filaments and Networks”. In: *Polymers* 9(12) (2017), p. 52.

[30] L. A. Mihai and A. Goriely. “Numerical simulation of shear and the Poynting effects by the finite element method: An application of the generalised empirical inequalities in non-linear elasticity”. In: *International Journal of Non-Linear Mechanics* 49 (2013), pp. 1–14.

[31] L. A. Mihai and A. Goriely. “Positive or negative Poynting effect? the role of adscititious inequalities in hyperelastic materials”. In: *Proceedings of the Royal Society A: Mathematical, Physical and Engineering Sciences* 467(2136) (2011), pp. 3633–3646.

[32] A. Anssari-Benam, A. Bucchi, and G. Saccomandi. “On the central role of the invariant i2 in nonlinear elasticity”. In: *International Journal of Engineering Science* 163 (2021).

[33] C. O. Horgan and J. G. Murphy. “On the volumetric part of strain-energy functions used in the constitutive modeling of slightly compressible solid rubbers”. In: *International Journal of Solids and Structures* 46(16) (2009), pp. 3078–3085.

[34] E. Vitral. “Stretch formulations and the Poynting effect in nonlinear elasticity”. In: *International Journal of Non-Linear Mechanics* 148 (2023), p. 104293.

[35] M. Destrade et al. “Extreme softness of brain matter in simple shear”. In: *International Journal of Non-Linear Mechanics* 75 (2015), pp. 54–58.

[36] D. Wang and M. S. Wu. “Generalized shear of a soft rectangular block”. In: *Journal of the Mechanics and Physics of Solids* 70 (2014), pp. 297–313.

[37] C. O. Horgan and J. G. Murphy. “Torsion of incompressible fiber-reinforced nonlinearly elastic circular cylinders”. In: *Journal of Elasticity* 103(2) (2010), pp. 235–246.

[38] A. Misra et al. “Pantographic metamaterials show atypical Poynting effect reversal”. In: *Mechanics Research Communications* 89 (2018), pp. 6–10.

[39] P. A. Janmey et al. “Negative normal stress in semiflexible biopolymer gels”. In: *Nature Materials* 6(1) (2006), pp. 48–51.

[40] V. Balbi et al. “Poynting effect of brain matter in torsion”. In: *Soft Matter* 15(25) (2019), pp. 5147–5153.

[41] L. E. Bilston, Z. Liu, and N. Phan-Thien. “Large strain behaviour of brain tissue in shear: Some experimental data and differential constitutive model”. In: *Biorheology* 38(4) (2001), pp. 335–45.

[42] C. O. Horgan and G. Saccomandi. “Simple Torsion of Isotropic, Hyperelastic, Incompressible Materials with Limiting Chain Extensibility”. In: *Journal of Elasticity* 56(2) (1999), pp. 159–170.

[43] L. M. Kanner and C. O. Horgan. “On extension and torsion of strain-stiffening rubber-like elastic circular cylinders”. In: *Journal of Elasticity* 93(1) (2008), pp. 39–61.

[44] R. S. Rivlin and D. W. Saunders. “Large elastic deformations of isotropic materials VII. experiments on the deformation of rubber”. In: *Philosophical Transactions of the Royal Society of London. Series A, Mathematical and Physical Sciences* 243(865) (1951), pp. 251–288.

[45] A. Ghorbani et al. “Inverted and programmable Poynting effects in metamaterials”. In: *Advanced Science* 8(20) (2021), p. 2102279.

[46] H. T. Banks, S. Hu, and Z. R. Kenz. “A brief review of elasticity and viscoelasticity for solids”. In: *Advances in Applied Mathematics and Mechanics* 3(1) (2011), pp. 1–51.

[47] A. E. Green and R. S. Rivlin. “The mechanics of non-linear materials with memory”. In: *Archive for Rational Mechanics and Analysis* 4(1) (1959), pp. 387–404.

[48] R. De Pascalis, I. D. Abrahams, and W. J. Parnell. “On nonlinear viscoelastic deformations: A reappraisal of Fung’s quasi-linear viscoelastic model. Proceedings of the Royal Society A: Mathematical”. In: *Physical and Engineering Sciences* 470(2166) (2014), p. 20140058.

[49] I. W. Hamley. *Introduction to soft-matter: Synthetic and biological self-assembling materials*. John Wiley & Sons, 2008.

[50] M. Doi. *Soft matter physics*. Oxford University Press, 2017.

[51] G. B. McKenna. “Soft matter: Rubber and Networks”. In: *Reports on Progress in Physics* 81(6) (2018), p. 066602.

[52] S. R. Nagel. “Experimental soft-matter science”. In: *Reviews of Modern Physics* 89(2) (2017).

[53] J. G. Murphy. “Strain Energy Functions for a Poisson Power Law Function in Simple Tension of Compressible Hyperelastic Materials”. In: *Journal of Elasticity and the Physical Science of Solids* 60(2) (2000), pp. 151–164.

[54] A. N. Gent, J. B. Suh, and S. G. Kelly III. “Mechanics of Rubber Shear Springs”. In: *International Journal of Non-Linear Mechanics* 42(2) (2007), pp. 241–249.

[55] A. Anssari-Benam and C. O. Horgan. “New constitutive models for the finite deformation of isotropic compressible elastomers”. In: *Mechanics of Materials* 172 (2022), p. 104403.

[56] B. R. Wang et al. “Modeling the initial-volume dependent approximate compressibility of porcine liver tissues using a novel volumetric strain energy model”. In: *Journal of Biomechanics* 109 (2020), p. 109901.

[57] M. T. Punter et al. “Poroelasticity of (bio)polymer networks during compression: Theory and experiment”. In: *Soft Matter* 16(5) (2020), pp. 1298–1305.

[58] H. Wang and X. Xu. “Continuum elastic models for force transmission in biopolymer gels”. In: *Soft Matter* 16(48) (2020), pp. 10781–10808.

[59] J. E. Bischoff, E. M. Arruda, and K. Grosh. “Finite element modeling of human skin using an isotropic, nonlinear elastic constitutive model”. In: *Journal of Biomechanics* 33(6) (2000), pp. 645–652.

[60] M. C. Boyce and E. M. Arruda. “Constitutive models of rubber elasticity: A Review”. In: *Rubber Chemistry and Technology* 73(3) (2000), pp. 504–523.

[61] L. Laiarinandrasana, R. Piques, and A. Robisson. “Visco-hyperelastic model with internal state variable coupled with discontinuous damage concept under total lagrangian formulation”. In: *International Journal of Plasticity* 19(7) (2003), pp. 977–1000.

[62] M. Hrapko et al. “The mechanical behavior of brain tissue: Large strain response and constitutive modeling”. In: *Biorheology* 43(5) (2006), pp. 623–36.

[63] H. Dal, O. Gültekin, and K. Açıkgöz. “An extended eight-chain model for hyperelastic and finite viscoelastic response of rubberlike materials: Theory, experiments and numerical aspects”. In: *Journal of the Mechanics and Physics of Solids* 145 (2020), p. 104159.

[64] T. P. Prevost et al. “Biomechanics of brain tissue”. In: *Acta Biomaterialia* 7(1) (2011), pp. 83–95.

[65] D. Zhong et al. “A visco-hyperelastic model for hydrogels with Tunable Water Content”. In: *Journal of the Mechanics and Physics of Solids* 173 (2023), p. 105206.

[66] T. Shoyama and K. Fujimoto. “Direct measurement of high-frequency viscoelastic properties of pre-deformed rubber”. In: *Polymer Testing* 67 (2018), pp. 399–408.

[67] J.S. Palmer and M.C. Boyce. “Constitutive modeling of the stress-strain behavior of F-actin filament networks”. In: *Acta Biomater* 4 (2008), pp. 597–612.

[68] F. Oyedeji Falope, L. Lanzoni, and A. M. Tarantino. “Finite torsion of compressible circular cylinders: An approximate solution”. In: *Journal of Elasticity* 151(2) (2022), pp. 187–217.

[69] D. A. Polignone and C. O. Horgan. “Pure torsion of compressible non-linearly elastic circular cylinders”. In: *Quarterly of Applied Mathematics* 49(3) (1991), pp. 591–607.

[70] E. Kirkinis and R. W. Ogden. “On extension and torsion of a compressible elastic circular cylinder”. In: *Mathematics and Mechanics of Solids* 7(4) (2002), pp. 373–392.

[71] A. P. Suvorov and A. P. S. Selvadurai. “On Poro-hyperelastic shear”. In: *Journal of the Mechanics and Physics of Solids* 96 (2016), pp. 445–459.

[72] P. A. Kakavas and N. K. Anifantis. “Effective moduli of hyperelastic porous media at large deformation”. In: *Acta Mechanica* 160(3–4) (2003), pp. 127–147.

[73] M. Danielsson, D. M. Parks, and M. C. Boyce. “Constitutive modeling of porous hyperelastic materials”. In: *Mechanics of Materials* 36(4) (2004), pp. 347–358.